Low Temperature Electron-Phonon Interaction in Disordered Metal Thin Films and Applications to Fast, Sensitive Sub-Millimeter Photon Sources and Detectors

A Dissertation

Presented to the Faculty of the Graduate School

of

Yale University

in Candidacy for the Degree of

Doctor of Philosophy

by

Minghao Shen

Dissertation Director: Robert Schoelkopf

December 2005

©2005 by Minghao Shen.

All rights reserved.

Abstract

Low Temperature Electron-Phonon Interaction in Disordered Metal Thin Films and Applications to Fast, Sensitive Sub-Millimeter Photon Sources and Detectors

Minghao Shen

May, 2005

The electron–phonon interaction in metals becomes very weak at very low temperatures (sub–Kelvin temperatures). It is very challenging to measure such weak interaction with traditional techniques. In this thesis work, we develop a new dynamic microwave noise thermometry technique for study the low temperature electron-phonon interaction in disordered metal thin films. The high sensitivity and fast time response of the thermometry allow us to study the electron–phonon interaction in nano–scale disordered metal thin films. Both long diffusive metal wires and short wires in SNS structures are observed. We measure the electron–phonon heat conductance G_{e-ph} in steady states, and the electron–phonon time τ_{e-ph} and electronic heat capacity C_e from the electron thermal dynamic in the time domain. The results of the three quantities are consistent within themselves for each device, and can be explained qualitatively by the theory (Sergeev & Mitin 2000). However, the measured values for G_{e-ph} and C_e are 10–50 times larger than the expected book values.

We also develop a new on-chip calibration scheme for ultra–sensitive submillimeter detectors, with phonon-cooled hot electron sources. The sources are essentially metal

thin films, whose hot electron induced Johnson noise is equivalent to one-dimensional blackbody radiation. The weak electron–phonon interaction in the film makes the source very accurate and fast at low temperatures for low photon power generation.

Acknowledgements

Contents

1 Introduction **15**

1.1 Motivation 15

1.2 Calibration of sub-mm detectors with hot electron blackbody photon source 18

1.2.1 Hot electron blackbody photon source 18

1.2.2 Electron-phonon interaction at low temperatures 20

1.2.3 On-chip Calibration Scheme 23

1.3 Thesis Overview 25

2 Metal Film Resistor Blackbody Photon Source **27**

2.1 Overview of Blackbody Radiation 27

2.1.1 Blackbody Radiation in General 27

2.1.2 One Dimensional Blackbody Radiation 28

2.2 Overview of Johnson Noise 30

2.3 Planar phonon cooled hot electron Blackbody Photon Source 33

2.3.1 Johnson Noise is Blackbody Radiation 33

3 Theoretical background on electron-phonon decoupling in disordered metal films **36**

3.1 Thermal model of metal thin film resistors on insulating substrates . 37

3.2 Interactions of electrons with the surroundings in disordered metal films 40
3.2.1 Electron-electron scattering in disordered metal films 40
3.2.2 Electron-phonon scattering rate 41
3.2.3 Electron-impurity scattering 41
3.2.4 Comparison of rates 42
3.3 Electron Joule heating 44
3.4 Electron cooling 45
3.4.1 Electron cooling by inelastic scattering 45
3.4.2 Electron-Phonon Cooling in Long Diffusive Wires 47
3.4.3 Electron-Phonon Interaction in SNS Structures 49
3.5 Electron-phonon Interaction in low temperature thin metal films . . . 51
3.5.1 Electron-Phonon interaction in *pure* metal 52
3.5.2 Impurity modifications to electron-phonon scattering 55
3.5.3 Electron-phonon interaction in disordered metals 56
3.5.4 The electron energy loss rate 63
3.5.5 Summary 64
3.6 Electron radiation cooling 65
3.7 Metal Film - Insulator Kaptiza Conductance 68
3.7.1 Acoustic mismatch theory 69
3.7.2 Diffuse mismatch theory 70
3.7.3 Kapitza heat conductance in our system 70
3.8 Electronic Heat Capacity 71
3.9 Hot electron blackbody photon sources and hot electron bolometers . 73

4 Dynamic Microwave noise thermometry 75

4.1 Review of techniques for measuring electron-phonon interaction . . . 75

4.2 Microwave noise thermometry setup 79

4.2.1 Microwave setup 79

4.2.2 DC bias line 85

4.3 Electron temperature T_e calibration 86

4.4 Electron-phonon interaction measurement setups 89

4.4.1 Steady state measurement setup 89

4.4.2 Dynamics measurement setup 90

5 Electron-phonon interaction in disordered thin Au films 93

5.1 Au thin film devices 94

5.2 Steady state characteristics 97

5.2.1 DC heating 97

5.2.2 The electron-phonon heat conductance from T_e vs. V_b curves . 103

5.2.3 Direct G_{e-ph} measurement with lockin amplifier 106

5.2.4 The saturation of G_{e-ph} at low temperatures 109

5.3 Electron-phonon dynamics 113

5.3.1 The electron-phonon time τ_{e-ph} 113

5.3.2 The electron-phonon interaction time in the dirty limit 117

5.3.3 The electron-phonon interaction time in the moderate disordered regime 120

5.4 The electronic heat capacity C_e 121

5.4.1 The electronic heat capacity C_e from G_{e-ph} and τ_{e-ph} 121

5.4.2 The electronic heat capacity C_e from calorimetry measurements 123

5.4.3 Possible explanations of the large measured C_e 129

5.5 Applications in ultra-sensitive sub–mm HEB's 133

5.5.1 The concept of the phonon–cooled HEB 133

5.5.2 Potential problems for the HEB performance 136

6 Designs for superconducting high frequency coplanar bandpass filter 143

6.1 On-chip calibration scheme 143

6.2 Lumped element filter prototype 145

6.3 The capacitively coupled CPW resonators bandpass filter 147

6.3.1 Filter layout 147

6.3.2 CPW–slotline balun 150

6.4 The edge coupled microstrip bandpass filter 151

6.4.1 Filter layout and simulated frequency response 152

7 Fabrication of On-chip Calibration Integrated Circuit 156

7.1 Integrated On-Chip Calibration Circuit Design 156

7.2 Fabrication Process Overview 159

7.2.1 Wafer Oxidation 160

7.2.2 Resist Process 161

7.2.3 E-beam Lithography 162

7.2.4 Development 167

7.2.5 Film deposition 167

7.2.6 Lift off 170

7.3 Fabrication of On-chip Calibration Device 170

7.3.1 Device layout 170

7.3.2 Wafer Oxidation 173

7.3.3 Pre-resist wafter cleaning 174

7.3.4 First material layer – Au 175

7.3.5 Second material layer – SiO_x 179

7.3.6 Third material layer – Al/Al_2O_3/Al junction 180

7.3.7 Fourth material layer – Nb 183

7.3.8 Image of the fabricated device 185

8 Conclusions 187

8.1 Summary of results presented in this thesis 187

8.2 Suggestions for future work 189

List of Figures

1.1 Background limited NEP$_{bg}$. 16
1.2 Dynamic Microwave Johnson noise thermometry scheme. 22
1.3 On-chip calibration scheme. 23

2.1 1D blackbody radiation power spectral density P_{bb}. 29
2.2 Nyquist's transmission derivation of Johnson noise. 31
2.3 The net Johnson noise power transmitted by a conductor. 33
2.4 Correlation between Johnson noise and blackbody radiation. 34

3.1 Metal thin film resistors on insulating substrates. 38
3.2 The comparison of electronic scattering rates. 43
3.3 Schematic of Andreev reflection at NS interface. 50
3.4 Electron-Phonon scattering in *pure* metal. 52
3.5 The electron-phonon rate in Cu in the moderate disorder regime. . . 63
3.6 The electron radiation heat conductance 67
3.7 Comparison of heat conductances for different cooling mechanism. . . 71

4.1 Schematics of dynamic microwave Johnson noise thermometry. 79
4.2 Block diagram of microwave noise thermometry setup. 80
4.3 The sample holder and microstrip launcher. 81
4.4 Electrons excessive heating by the thermal radiation of the amplifier. 82

4.5 Electron temperature T_e calibration. 88

4.6 Setup for G_{e-ph} measurement. 90

4.7 Electron-phonon dynamics measurement setup. 91

5.1 Optical microscope pictures for the devices. 98

5.2 T_e vs. P_{Joule} for Au wire in the SNS structure, device SNS-2. 99

5.3 The T_e vs. P_{Joule} for device Diff-1 and SNS-1. 101

5.4 T_e vs. P_{Joule} for device Diff-2, long diffusive Au wire. 102

5.5 T_e vs. V_b curve for device SNS-2. 103

5.6 The temperature dependence of the electron-phonon heat conductances. 105

5.7 Comparison of the G_{e-ph} per unit volume. 106

5.8 The temperature dependence of G_{e-ph} for device SNS-2. 107

5.9 Temperature dependence of G_{e-ph} for device Diff-2. 108

5.10 Comparison of G_{e-ph} per volume for device Diff-2 and SNS-2. 109

5.11 The uncertainty in the electron temperature induced by amplifier drifts. 112

5.12 The time response of electron temperature T_e to a fast heat pulse. . . 114

5.13 The temperature dependence of the electron-phonon time constant . . 116

5.14 The level of disorder of devices the measurement ranges. 118

5.15 Comparison of τ_{e-ph} data and theory for device SNS-1 and SNS-2. . . 119

5.16 The comparison of data and theory for device Diff-2. 121

5.17 Comparison of the derived electronic specific heat for the devices. . . 122

5.18 The calorimetry approach for measuring the electronic heat capacity. 124

5.19 The electron temperature responses to heat pulses for device Diff-2. . 126

5.20 The time response of electron temperature T_e to short heat pulses. . . 127

5.21 The Schottky anomaly. 139

5.22 Possible thermal structure that leads to large G_{e-ph} and C_e. 140

5.23 Comparison between G_{diff} and G_{e-ph} for device Diff-2. 140
5.24 The thermal structure of the phonon cooled HEB. 141
5.25 The minimal volume of the phonon cooled HEB absorber. 141
5.26 The NEP for an HEB with our Au thin film as the absorber 142
5.27 Ultimate sensitivity for our Au thin films as the phonon–cooled HEB. 142

6.1 Block diagram of the on-chip photon calibration scheme. 144
6.2 Lumped element model for bandpass filter. 146
6.3 Transmission lines. 147
6.4 The physical layout of the capacitively coupled CPW resonators bandpass filter. 148
6.5 200 GHz CPW bandpass filter simulation with Sonnet. 149
6.6 Broadband CPW–slotline balun. 151
6.7 The schematic layout of an edge coupled microstrip bandpass filter. . 152
6.8 Frequency response of the 200 GHz microstrip bandpass filter. 153
6.9 A quarter wavelength radial stub as RF ground. 154
6.10 RF chokes for DC bias. 154
6.11 The DC bias scheme for the photon source. 155

7.1 Schematic of the simplified on-chip calibration circuit. 157
7.2 Cross-section of a coplanar stripline. 159
7.3 Steps of e-beam lithography process. 160
7.4 MMA/PMMA double layer e-beam resist with controlled MMA undercut. 162
7.5 Patterns for e-beam lithography alignment. 165
7.6 The proximity effect in e-beam lithography. 166
7.7 Schematic of double angle evaporation. 169

7.8 On-chip calibration device layout at microscope magnification of 150. 171

7.9 Zoom-in on the source-stripline-detector structure. 172

7.10 Segments of the conductor strip for proximity effect correction. 176

7.11 Proximity effect in Al junction writing. 181

7.12 Nb film sputtered on SiO_x deposited on Au. 184

7.13 Optical microscope and SEM images of the on-chip calibration device. 186

List of Tables

3.1 The scaling factors between $\tau_{e-ph}^{-1}(\varepsilon_F, T)$ and τ_{e-ph}^{-1} 64

3.2 The measured temperature dependence of τ_{e-ph}^{-1} on metal thin films. . 66

3.3 Estimated $G_{Kapitza}/T^3$ per unit area 70

5.1 List of devices presented in the thesis. 96

5.2 The parameters for $T_e(P_{Joule})$ characteristics calculated from eqn.(5.2(b)). 100

5.3 Power law temperature dependence of G_{e-ph}. 104

5.4 The fitting parameters of τ_{e-ph} temperature dependence. 117

5.5 Summary of the measured electronic specific heats. 129

6.1 The components of a 200 GHz equal–ripple bandpass filter. 146

6.2 Resonator lengths for 200 GHz bandpass filter 148

6.3 Capacitances of the coupling capacitors in 200 GHz CPW bandpass filter. 149

7.1 Beam currents for different spot sizes of FEI XL30 SEM. 163

7.2 Steam oxidation parameters. 175

7.3 Pre-resist wafer cleaning. 175

7.4 Au layer resist process. 175

7.5 Exposure parameters for Au critical structures 178

7.6 Au e-beam evaporation parameters. 178

7.7 E-beam writing parameters for SiO_x. 179

7.8 SiO_x Sublimation. 180

7.9 $Al/Al_2O_3/Al$ layer resist process. 181

7.10 Area doses in $\mu C/cm^2$ for SQUID writing. 182

7.11 Double angle evaporation for $Al/Al_2O_3/Al$ junctions. 183

7.12 Nb resist process. 183

7.13 Nb sputtering parameters. 185

List of symbols and abbreviations

CPS — Coplanar stripline

CPW — Coplanar waveguide

HEB — Hot electron bolometer

NEP — Noise equivalent power

NIS — Normal metal–insulator–superconductor

rf — Radio frequency

STJ — superconducting tunnel junction

SNS — Superconductor–normal metal–superconductor

B — Frequency bandwidth

C — Heat capacity

C_e — Electronic heat capacity

C_p — Phonon heat capacity

D — Diffusion constant

ε_F — Fermi energy

G — Heat conductance

G_{e-ph} — Electron–phonon heat conductance

G_K — Kapitza heat conductance

G_{diff} — Diffusion heat conductance

G_γ — Electron radiation heat conductance

ℓ — Electron mean free path

$\mathcal{L}$ — Electron elastic mean free path

L_{e-ph} — Electron–phonon length

L_{e-e} — Electron–electron length

P_{Joule} — Joule power

P_{e-ph} — Electron–phonon cooling power

$q_{T,l}$ — Longitudinal phonon wave vector

$q_{T,t}$ — Transverse phonon wave vector

R — Resistance

$R_{\square}$ — Sheet resistance.

T — Temperature

T_{bb} — Blackbody temperature

T_e — Electron temperature

T_p — Phonon temperature

T_{bath} — Bath temperature

T_s — Substrate temperature

T_A — Amplifier noise temperature

τ — Time constant

τ_e Electron scattering time

τ_{e-ph} — Electron–phonon time

τ_{e-e} — Electron–electron time

τ_{e-imp} — Electron–impurity time

u_l — Longitudinal acoustic phonon length

u_t — Transverse acoustic phonon length

V_b — Bias voltage

V_d — Diode voltage

ζ — Zeta function

Chapter 1

Introduction

1.1 Motivation

The Cosmic Microwave Background (CMB) provides modern astrophysicists with essential information on understanding the evolution of the universe, from the initial moment following the big bang to its complex form seen today. The density fluctuations in the CMB record the history of the universe; their development led to the formation of different structures, from simple elements to very complex stars and galaxies. The far infrared and submillimeter emissions are particularly important for studying the early stages of structure formation, since much of the emissions in these phases are in this wavelength range. The ultimate goal for future NASA missions in far infrared and submillimeter studies is to observe the CMB at the background limit in the desired frequency band (Mather et al. 2002).

High sensitivity detectors are the key factors for such missions. The sensitivity of a detector is frequently given by a figure of merit, called the noise equivalent power (NEP), which is the radiation flux impinged on the detector that gives a signal/noise ratio of unity in 1 Hz bandwidth. If the sensitivity of the detector is limited by the photon shot noise, the detector has a background limited NEP, which is determined by the photon power P_ν , and the detecting bandwidth B as $NEP_{bg}=P_\nu/\sqrt{B}$. For

instance, in one dimensional photon detection, for a bandwidth B that is much smaller than the photon frequency ν, the photon power is approximately $h\nu B$, thus the NEP has the form $h\nu/\sqrt{B}$. Fig.1.1 is an example of the background limited NEP_{bg} due to the thermal radiation of a uniform 30 K background in the far infrared and submillimeter range, assuming a 10 KHz bandwidth. In reality, the CMB is not

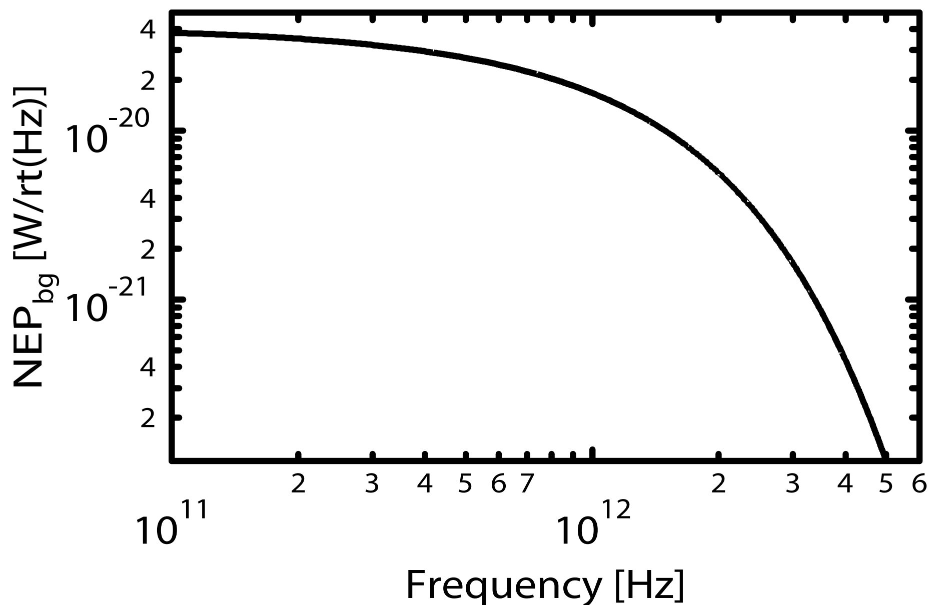

Figure 1.1: Background limited NEP_{bg}.
NEP_{bg} as a function of the photon frequency ν. The background temperature is 30 K and the bandwidth B is 10 KHz for narrow band detection.

uniform; the photon limited sensitivity of the detector does not have the simple curve as above, due to the non-uniform density of CMB (Mather et al. 2002). In future NASA infrared and sub-millimeter missions, it is desirable to have cryogenic detectors with NEP better than the background photon limited NEP_{bg}, i.e. NEP$\sim 10^{-20} - 10^{-21} W/\sqrt{Hz}$ or better for narrow band detection.

With the improvement in the sensitivity of sub-millimeter detectors, the calibration of such detectors becomes increasingly complicated; we need cryogenic sub-millimeter photon sources that can produce very low power (e.g. $\sim$ pW at 200 GHz

in 10% bandwidth) with very high precision, and a calibration scheme that can couple the source and the detector easily and efficiently at cryogenic temperatures. One possible approach is to use a room temperature source, attenuate its output to the desired power level, and couple it to the detector that sits in a cryostat. However, it is difficult to make an attenuator with very large and accurately known attenuation. Hence, it is hard to know precisely how much power is coupled to the detector. Also, extra care is required to block the thermal radiation from room temperature to the detector. Alternatively, one can use a cryogenic blackbody source, which is held at the same temperature as the detector in the cryostat, and the power is delivered through a feed horn or a waveguide. The photon radiation power at a given frequency can be readily adjusted by precisely controlling the blackbody temperature; the thermal radiation from room temperature is thus largely reduced. However, due to the relatively large size ($\sim$ cm^3) of the conventional blackbody cavity, it is hard to cool the source accurately to the required temperature at the low temperature range, the power needed to heat up the source is high enough to heat up the cryostat, and the time response of the source is slow. Moreover, the use of a feed horn leads to a low efficiency and poor precision of power coupling between the source and the detector; hence, there is an uncertainty in the photon power absorbed by the detector. Therefore, one of the major challenges to the development of ultra-sensitive cryogenic submillimeter detectors is how to calibrate them with high accuracy and sensitivity, with the proper photon source and calibration scheme.

In this thesis work, we develop a new on-chip calibration scheme for ultra sensitive cryogenic sub-millimeter detectors, using a thin metal film resistor as a hot electron blackbody photon source. In the rest part of this chapter, I will give an overview of the basic concepts of the source and the scheme, and an outline of the thesis.

1.2 Calibration of sub-mm detectors with hot electron blackbody photon source

1.2.1 Hot electron blackbody photon source

The thermal blackbody radiation can be a source of photons of all frequencies. It is generated by any object that is not at absolute zero temperature. It can be considered as a collection of photons in thermal equilibrium in an enclosure, whose walls are held at the temperature T_{bb}. The photons are bosons that follow the Plank distribution[1]

$$\langle n(\nu, T_{bb})\rangle = \frac{1}{e^{h\nu/k_B T_{bb}} - 1}, \tag{1.1}$$

where $\langle n\rangle$ is the average number of photons with energy $h\nu$, ν being the frequency of the photon, at a given blackbody temperature T_{bb}. The photon power delivered per unit frequency for a one-dimensional blackbody is

$$P_{bb}(\nu) = \frac{h\nu}{e^{h\nu/k_B T_{bb}} - 1}. \tag{1.2}$$

The Johnson noise generated by a conductor originates from the thermal fluctuation of the electrical carriers; in metals, the carriers are conduction electrons. For the low frequency and high temperature limit ($\nu \ll k_B T_{con}/h$), the noise power per unit frequency is given by the Nyquist Theorem, formulated by Nyquist in 1928 by assigning each electrical wave mode an energy $k_B T$ from the classic equipartition law (Nyquist 1928):

$$P_{JN}(\nu) = k_B T, \tag{1.3}$$

where T is the temperature of the conductor. The general form of the theorem for all frequencies should take into account the quantum correction. Thus, the full form of the Johnson noise power per unit frequency is (Callen & Welton 1951)

$$P_{JN}(\nu) = \frac{1}{2}h\nu + \frac{h\nu}{e^{h\nu/k_B T} - 1}, \tag{1.4}$$

[1] more details can be found in most dynamics books (Huang 1987, Pathria 1996, Reif 1965)

where the first term $h\nu/2$ is from the zero–point energy of the fluctuations. However, the net noise power that can be transmitted by the conductor to another matched conductor that is connected to it by a matched transmission line is only the second term. This transmitted noise power has the same form as the one-dimensional blackbody radiation power in eqn.(1.2). In fact, it has been pointed out by Dicke (1946) that the Johnson noise power transmitted from a conductor to a matched resistive load is indeed equivalent to a one dimensional blackbody radiation power, with the blackbody temperature $T_{bb} = T$.

In the above discussion, we use the conductor temperature T in a fairly casual manner. In fact, a metallic conductor consists of both conduction electrons and phonons (the lattice with vibrating ions), and they have temperatures T_e and T_p respectively. When Joule power is applied to the metallic conductor, the conduction electrons are heated up. The electrons cool down by exchanging energy with the phonons of the metal by scattering, and the strength of the process is characterized by the electron-phonon heat conductance G_{e-ph}. At room temperature, the interaction is so strong that for typical applied power levels ($\sim$ 10 W), the electrons and the phonons always have the same temperature. In this case, the conductor temperature $T = T_e = T_p$. However, at very low temperatures ($<$ 1 K), the electron-phonon interaction becomes extremely weak, thus making it possible to drive the electrons significantly above the phonon temperature with only a small amount of power (Wellstood et al. 1994, Roukes 1985). In other words, the electrons and the phonons are decoupled at low temperatures. As the fluctuation of electrons is the origin of Johnson noise in the conductor, the conductor temperature T in eqn.(1.3) and eqn.(1.4) should be replaced by the electron temperature T_e. Thus the Johnson noise power per

bandwidth transmitted by the conductor to a matched load is

$$P(\nu) = \frac{h\nu}{e^{h\nu/k_B \mathbf{T_e}} - 1}, \tag{1.5}$$

which is also a one-dimensional blackbody radiation power at the electron temperature T_e. The blackbody radiation power can be easily controlled by changing the applied Joule power to vary the electron temperature T_e, which is effectively the blackbody temperature T_{bb}. Hence, at low temperatures, a metal thin film resistor is a hot electron blackbody photon source.

1.2.2 Electron-phonon interaction at low temperatures

The performance of the hot electron blackbody photon source depends on the electron-phonon interaction in the metal film at its operating temperature (< 1 K). Thus, a necessary first step is to characterize the electron-phonon interaction in metal films at low temperatures; we need to know the electron-phonon heat conductance G_{e-ph}, time constant τ_{e-ph}, and the electronic heat C_e of the film.

The low temperature electron-phonon interaction is also an elementary process for several other phenomena and applications. The electron-phonon interaction determines the cooling time of the electron gas, if the electrons are not cooled by out diffusion (see Chapter 2). The electron-phonon inelastic scattering also decides the electron dephasing time τ_φ, which is the time scale for a conduction electron to stay in a given exact one-electron energy eigenstate. The weak electron-phonon coupling at low temperatures is the basis for ultra-sensitive phonon cooled hot electron bolometers. The sensitivity of the bolometers improves as the G_{e-ph} drops (Nahum & Richards 1991), NEP$\propto \sqrt{G_{e-ph}}$.

However, our knowledge on electron-phonon interaction is rather limited; only a few experiments have been done on the steady state characteristics and the electron-

phonon scattering rate τ_{e-ph}^{-1} on a few materials by Roukes et al. (1985), Santhanam & Prober (1984), Wellstood et al. (1994), Echternach et al. (1993), Gershenson et al. (2001), and Lin & Bird (2002) and reference within, and there has only been one successful direct dynamic measurement in time domain (Schmidt, Yung & Cleland 2004). The main obstacle is the lack of a fast and accurate probe for the interaction at sub-Kelvin temperatures. Several techniques have been used to measure the interaction: 1).weak localization for measuring the τ_{e-ph} from electron dephasing time τ_{φ}, 2). heating experiments for hot electron generation with Superconducting Quantum Interference Device (SQUID)noise thermometry, or Normal metal-Insulator-Superconductor (NIS) junction thermometry for T_e measurement. Only one of these methods is capable of measuring all aspects of the electron-phonon interaction; Schmidt, Yung & Cleland (2004) were the first to demonstrate a direct time domain measurement of electron-phonon interaction with rf-NIS thermometer. G_{e-ph}, τ_{e-ph}, and C_e are also measured within the same setup. However, only few materials can be measured with this technique due to the required NIS junctions, and there is an upper limit for the measurement temperature, which is the critical temperature T_c of the superconductor Al ($\sim$ 1.2K).

In this thesis work, we develop a new technique for measuring low temperature electron-phonon interaction in nano-structures with fast and sensitive dynamics microwave Johnson noise thermometry (Fig.1.2). The technique allows us to measure both the steady state characteristics and dynamics of the interaction for a large variety of materials, and to extract G_{e-ph}, τ_{e-ph}, and C_e together. The device we study is a thin film resistor made by the material of interest. We generate hot conduction electrons in the film by applying a voltage (V_b) across the resistor through a bias-tee. If the electrons do not cool via diffusing into the leads, we assume that the electrons

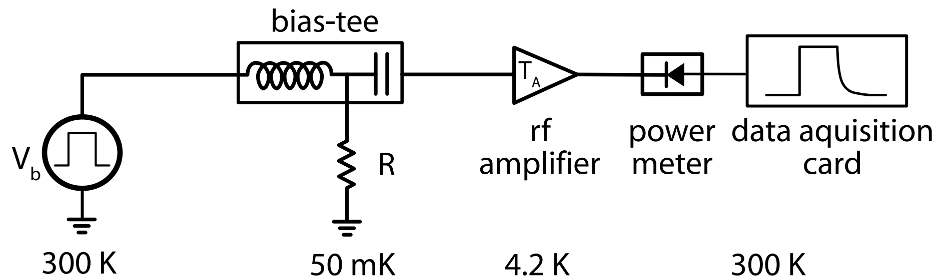

Figure 1.2: Dynamic Microwave Johnson noise thermometry scheme.

are heated to a uniform temperature T_e. Since the electrons and the phonons are decoupled at low temperatures, the low frequency ($\hbar\omega << k_B T_e$) rf Johnson noise of the resistor is given by

$$P_{JN} = k_B T_e B, \tag{1.6}$$

where B is the bandwidth of the measurement. This gives a direct measurement of the electron temperature T_e. The Johnson noise is coupled out of the resistor through the bias-tee, amplified by a cold low noise rf ($T_A \sim 5$ K) amplifier, and eventually detected by a power meter. This setup has very high temperature resolution; if the amplifier noise temperature is ~ 1 K, for a typical 1 s integration time in 100 MHz bandwidth, the setup has a sensitivity ~ 0.1 mK. Moreover, the microwave thermometry has a very fast time response, which is ultimately limited by the system bandwidth ~ 500 MHz. It allows us to directly measure the electron-phonon relaxation time $\tau_{e-ph} \sim \mu s$ in the time domain.

With this technique, we measure the electron-phonon heat conductance G_{e-ph} from the steady state T_e characteristics, where electrons in the film are heated up by a DC current or a current that varies much slower than the electron-phonon time τ_{e-ph}. We can also apply a fast heat pulse to the resistor, so that the electrons in the film are heated and cooled accordingly, and the τ_{e-ph} is extracted from exponential

fittings to the curve. The electronic heat capacity is thus obtained through

$$C_e = G_{e-ph}\tau_{e-ph}. \tag{1.7}$$

The C_e is also directly observed by using a calorimetric type of measurement. A pulse of power P that has a duration Δt much shorter than the electron-phonon time is applied to the film. The energy in the pulse $P\Delta t$ is completely absorbed by the electron gas to heat it up by ΔT_e, and the electron gas cools afterwards on the larger electron–phonon time scale. Thus, the heat transfer follows the relation

$$P\Delta t = C_e \Delta T, \tag{1.8}$$

from which the electronic heat capacity $C_e = P\Delta t/\Delta T_e$ is extracted. This gives a good cross check for the value obtained from eqn.(1.7).

1.2.3 On-chip Calibration Scheme

The hot electron blackbody photon source is essentially a thin piece of metal, hence, it can be used in our new on-chip calibration scheme, as shown in Fig.1.3. The

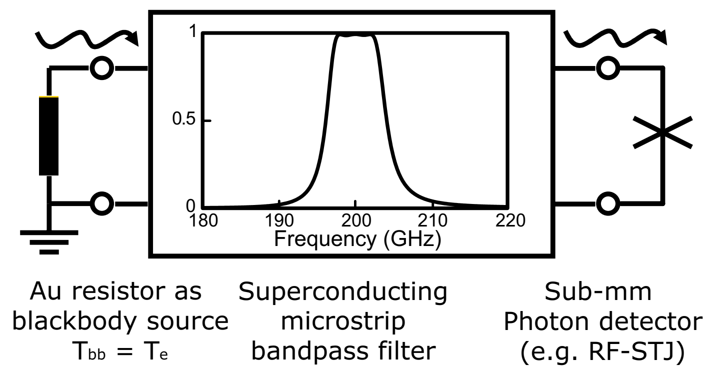

Figure 1.3: On-chip calibration scheme.
The hot electron photon source (left) is connected to the detector under study (right) by a superconducting bandpass filter(center).

detector we are interested in calibrating is an $Al/Al_2O_3/Al$ superconducting tunnel

junction detector. Both the source and the detector are planar structures that can be fabricated on the same Si/SiO_2 substrate. They are connected by a coplanar superconducting bandpass filter, which selects the photons emitted by the source in the desirable frequency band to calibrate the filter. The filter also blocks the DC signals of the source and the detector from each other, so that the two sides can be measured independently but simultaneously. There are several advantages of this on-chip calibration scheme:

- High accuracy: The photon power generated by the source can be precisely determined from the blackbody temperature, which is the same as the hot electron temperature T_e. It can be monitored by using microwave thermometry with very high accuracy during the detector calibration.

- Low input power: Due to the very weak electron-phonon interaction in the film, even a small amount of input power can heat up the electrons significantly, thus changing the source output photon power by a large amount.

- High speed: The source has a very fast time response; it is limited by the electron-phonon interaction time τ_{e-ph}, which is usually in the order of $\sim\mu s$ below 200 mK (see our measurement results in Chapter 5).

- Ease of coupling: All three components of the calibration scheme are planar structures. Therefore, they can be easily integrated on the same substrate by using standard micro-fabrication processes.

- Low loss: The superconducting bandpass filter has low electrical loss in the band when it is matched to both the source and the detector. Thus, the coupling coefficient between the source and the detector is a well defined quantity of the order of unity.

1.3 Thesis Overview

This thesis is roughly divided into two parts. The first part covers the theoretical aspects of the hot electron photon source and the low temperature electron-phonon interaction. It also includes steady state and dynamic measurements of the electron-phonon interaction by using the microwave noise thermometry technique. The second part deals with the development of the on-chip calibration scheme. The possible designs of the the coplanar superconduction bandpass filters are presented. It is followed by the design and fabrication of a simplified version of the on-chip calibration scheme, which gives us some preliminary results.

In the first part, Chapter 2 gives an overview of the relation between blackbody radiation and Johnson noise. In Chapter 3, we discuss the underlying physics of the source — the electron interactions with the surrounding environment; in particular, we discuss the electron-phonon interaction in normal metal disordered thin films at low temperatures. We also present the concept and fabrication of superconductor-normal metal-superconductor (SNS) devices, which are suitable for studying such interactions. A new technique for measuring the electron-phonon interaction is introduced in Chapter 4. The fast and sensitive dynamic microwave noise thermometry is used to measure the steady state and dynamics properties of the electron-phonon interaction, from which we extract the G_{e-ph}, τ_{e-ph} and C_e. Chapter 5 gives the results of such measurements for two classes of devices: 1. long metal film whose length L is much larger than the electron-phonon length l_{e-ph}, 2. short normal metal films in SNS structures. We also discuss the possible use of such nano-scale metal thin film resistors as simple, fast, and sensitive hot electron bolometers (HEB's).

In the second part, in Chapter 6, we outline the concept of a new on-chip calibration scheme for ultra sensitive detectors with hot electron blackbody photon sources.

We then discuss a crucial component of the calibration scheme — the superconducting coplanar bandpass filters. Different stages of the filter development are given, such as modeling, simulation, etc. In the last chapter, we show some preliminary results for on-chip calibration of Superconducting Tunnel Junction (STJ) detector with a simplified version of the calibration, where the filter is replaced by a coplanar strip line.

Chapter 2

Metal Film Resistor Blackbody Photon Source

2.1 Overview of Blackbody Radiation

2.1.1 Blackbody Radiation in General

The blackbody radiation refers to the thermal radiation power generated by a perfect emitter — a blackbody at non-zero temperatures. In the early 20th century, Rayleigh and Jeans predicted an "infinite" thermal radiation power by applying the equipartition theorem of classical statistical mechanics. This obviously unrealistic result caused a huge disturbance in the Physics community at that time, and it was called the "ultraviolet catastrophe". It was later pointed out by Einstein that the radiation should be described by Plank's theory, that is the radiation consists of discrete packets of electromagnetic energy proportional to the frequency, and the distribution of the packets should follow the Plank's distribution. The packages of energy, now known as photons, are identical and indistinguishable bosons of electromagnetic field energy quanta with the following characteristics

$$\begin{aligned} &\text{energy } \varepsilon = h\nu \\ &\text{momentum } \mathbf{p} = \hbar\mathbf{k}, \qquad |\mathbf{k}| = \frac{2\pi\nu}{c} \end{aligned} \tag{2.1}$$

where ν is the frequency, $\mathbf{k}$ is the wavenumber, and c is the speed of light in vacuum.

In order to calculate the actual blackbody radiation power, we can use a good approximation to the blackbody — a cavity of any material with only a pin hole open to the outside world. Electromagnetic radiations impinging on the pin hole enter the cavity and are absorbed by the enclosure walls and re-emitted into the cavity while they are scattering inside the cavity. Since there is only a small opening on the cavity, only a very small part of the electromagnetic radiation can escape from the cavity; the cavity is a nearly perfect absorber, thus a blackbody. Therefore, it can be used to characterize the blackbody radiation. Without loss of generality, in the rest of the thesis, we will only consider a cubical cavity[1] of volume $V = L^3$. The number of photon states per unit volume (density of state) between ν and $\nu + d\nu$ is

$$D(\nu)d\nu = \frac{4\pi}{c^3}\nu^2 d\nu. \tag{2.2}$$

The mean value for the number of photons is given by the Planck's distribution

$$\langle n\rangle = \frac{1}{e^{h\nu/k_B T_{bb}} - 1}, \tag{2.3}$$

The energy density (energy per unit volume) of the blackbody radiation in the frequency range (ν, $\nu + d\nu$) is given as follows,

$$u(\nu)d\nu = D(\nu)h\nu\langle n\rangle d\nu = \frac{4\pi h}{c^3}\frac{\nu^3 d\nu}{e^{h\nu/k_B T_{bb}} - 1}. \tag{2.4}$$

Note that for a fixed frequency range, the radiation energy is determined by T_{bb}.

2.1.2 One Dimensional Blackbody Radiation

Let us now consider the case of one-dimensional blackbody radiation, from a wire of length L. The density of state takes a different expression from eqn.(2.2); the density

[1]General discussions on the blackbody radiation can be found in most Statistical Mechanics books, e.g. (Huang 1987, Pathria 1996, Reif 1965).

of state of photons for one photon polarization in the range $(\nu, \nu + d\nu)$ is given as

$$D_{1D}(\nu) = \frac{1}{c}, \tag{2.5}$$

independent of ν. Hence the blackbody radiation energy per unit length in the frequency range is

$$u_{1D}(\nu)d\nu = \frac{1}{c}\frac{h\nu}{e^{h\nu/k_B T_{bb}} - 1}d\nu. \tag{2.6}$$

Since the photons travel at the speed of light c, the blackbody radiation power spectral density is

$$P_{bb}(\nu) = u_{1D}(\nu)c = \frac{h\nu}{e^{h\nu/k_B T_{bb}} - 1}. \tag{2.7}$$

Fig.2.1 depicts the one-dimensional blackbody radiation power as a function of T_{bb} at

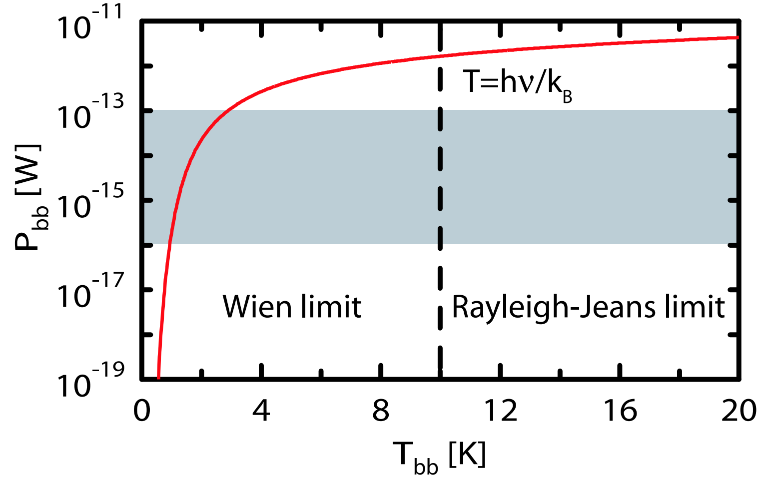

Figure 2.1: 1D blackbody radiation power spectral density P_{bb}. The P_{bb} is calculated for radiation at 200 GHz in 10% bandwidth. The shaded region indicates the desired power level for calibrating a 200 GHz photon detector in 10 GHz bandwidth with NEP $10^{-18} - 10^{-19}$ W/$\sqrt{Hz}$

frequency $\nu = 200$ GHz in 10% bandwidth. The dashed line denotes the temperature of the thermal energy that is equivalent to $h\nu$, i.e. $T = h\nu/k_B \cong 10$ K. At temperatures below it, the radiation is in the *Wien limit*, and above it, in the *Rayleigh-Jeans*

limit. In the Rayleigh-Jeans limit, or equally the low frequency limit ($\nu \ll k_B T_{bb}/h$), the power spectral density has the form

$$P_{bb}(\nu) \approx k_B T_{bb}, \tag{2.8}$$

thus depending on the temperature T_{bb} linearly and being independent of the photon frequency. In the Wien limit, or the high frequency limit ($\nu \gg k_B T_{bb}/h$), the radiation power spectral density is

$$P_{bb}(\nu) \approx h\nu e^{-h\nu/k_B T_{bb}}. \tag{2.9}$$

Thus, for a given photon frequency, the power density drops exponentially as the temperature T_{bb} decreases. In this regime, the radiation power level is very low at low temperatures. In fact, the photon power levels needed for calibrating a photon detector, with $NEP \sim 10^{-18} - 10^{-21}\, W/\sqrt{Hz}$ at $200\, GHz$ in $\sim 10\, GHz$ bandwidth, is in the shaded region ($10^{-13} - 10^{-16}\, W$). Also, the output source power strongly depends on the the blackbody temperature; a minute change of temperature can change the power drastically (e.g. if the temperature changes from 2 K to 1 K, the power drops by an order of magnitude). Thus, a blackbody at temperature below $\sim\ 4\, K$ is a good candidate for sensitive calibration source.

2.2 Overview of Johnson Noise

Johnson Noise (or **Johnson–Nyquist Noise**) generated by a conductor is a thermal noise induced by the thermal fluctuations of the current carriers (e.g. electrons in metals) (Nyquist 1928, Bennett 1960, Reif 1965); the fluctuating charges cause a fluctuating voltage V across the conductor (or a fluctuating current, depending on the choice of bias.)

The functional form of Johnson noise was first derived by Nyquist (1928) from transmission line theory and the second law of thermodynamics. In his derivation, Nyquist considered the detailed balance of power transferred between two identical conductors at the same temperature, connected by an ideal lossless transmission line, demonstrated in Fig.(1.2). The circuit is a matched network, therefore all the noise

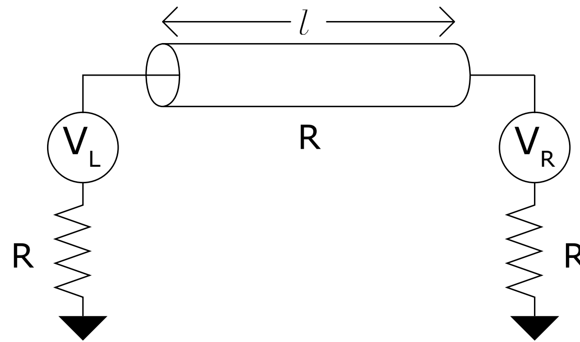

Figure 2.2: Nyquist's transmission derivation of Johnson noise.
The two identical conductors with resistance R are connected by a lossless transmission line with characteristic impedance R and length l. The conductors are held at the same temperature T_R. The conductor is equivalent to an ideal noiseless conductor in series with a noise voltage source. The Johnson noise power generated by one conductor transmits along the transmission line and arrives at the other conductor, where the power is absorbed. The two powers generated by the two conductors are in detailed balance, $P_{JN-right}(\omega, T_R) = P_{JN-left}(\omega, T_R)$, according to the second law of thermodynamics.

power impinging on the conductor is completely absorbed without any reflection and there are no standing waves in the transmission line. The voltage noise spectral density S_V (the average $\langle V^2 \rangle$ per unit bandwidth) of the conductor is given by Nyquist's theorem

$$S_V(\nu, T_R) = 4k_B T_R R. \tag{2.10}$$

The factor of 4 comes from the noise current divided between the two identical resistors (Fig.2.2); the noise voltage of the left (right) conductor induces a current in the right (left) conductor with the value $V_L/2R$. The spectral density of the John-

son noise power transmitted from one conductor to the other conductor through the transmission line is

$$P_{JN}(\nu, T_R) = k_B T_R. \tag{2.11}$$

This simple frequency independent form is only valid for low frequencies, $\omega \ll k_B T_R/\hbar$. The linear temperature dependence of the noise is the basis for Johnson noise thermometry, where the low frequency Johnson noise is a direct measurement of the temperature.

In 1951, Callen and Welton (Callen & Welton 1951) generalized Nyquist's theorem to the fluctuation-dissipation theorem (FDT). The theorem relates the thermal fluctuations of the generalized forces in any passive linear dissipative system to the generalized resistance (the real part of the impedance $Re[Z(\nu)]$). The noise power spectral density of any linear system is related to the impedance as

$$S_V(\nu, T) = \frac{1}{2\pi} 4Re[Z(\nu)] \left[\frac{1}{2} h\nu + \frac{h\nu}{\exp\left(\frac{h\nu}{k_B T}\right) - 1} \right], \tag{2.12}$$

where T is the temperature of the linear system. Note that, the quantity in the square bracket is in fact the mean energy of a harmonic oscillator with frequency ω at temperature T, and the first term gives the zero-point energy. Thus, the spectral density of the Johnson noise power of a conductor is

$$P_{JN}(\nu, T) = \left[\frac{1}{2} h\nu + \frac{h\nu}{\exp\left(\frac{h\nu}{k_B T}\right) - 1} \right]. \tag{2.13}$$

At low frequencies $\nu \ll k_B T/h$, the FDT recovers the original Nyquist relation. The net power delivered by a conductor through a transmission line to a resistive termination, however, does not include the zero-point power (Schmidt, Schoelkopf & Cleland 2004*b*),

$$P = \frac{h\nu}{\exp\left(\frac{h\nu}{k_B T}\right) - 1}. \tag{2.14}$$

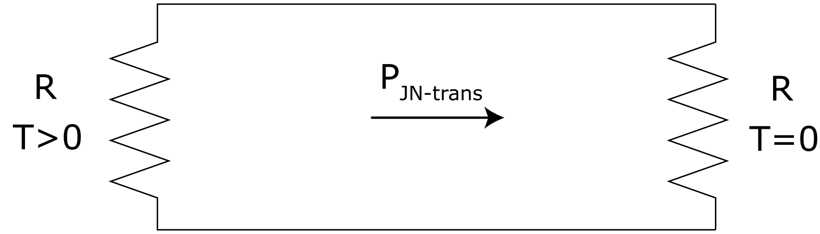

Figure 2.3: The net Johnson noise power transmitted by a conductor. The conductor is at temperature $T > 0$, and the Johnson noise power is transmitted to a matched conductor at $T = 0$.

This can be demonstrated by the schematic in Fig.2.3. The two matched conductors are connected by a transmission line, and the left conductor is at a temperature $T > 0$, while the right conductor is at absolute zero temperature. The Johnson noise power spectral density of the left conductor is given by eqn.(2.13), while that of the right conductor is just zero-point power $h\nu/2$. Thus, the Johnson noise power spectral density can be drawn from the left to the right, and is equal to the difference of the two as given in eqn.(2.14).

2.3 Planar phonon cooled hot electron Blackbody Photon Source

2.3.1 Johnson Noise is Blackbody Radiation

The above discussion shows that the one-dimensional blackbody radiation power spectral density eqn (2.7) has the same form as the Johnson noise power spectral density transmitted by a conductor eqn (2.14). In fact, the two powers are indeed equivalent. Such a correlation was discussed by Dicke (1946) in his microwave radiometer study by using the following simple thermodynamic model depicted in Fig.2.4. A conductor of resistance R is connected through a transmission line to an antenna that is

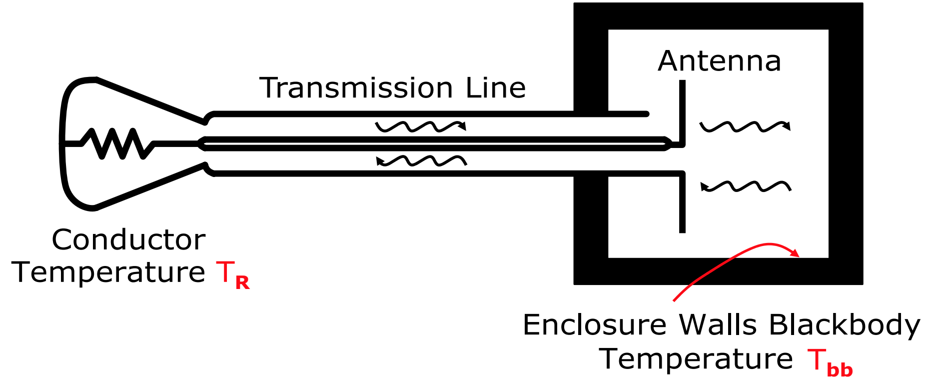

Figure 2.4: Correlation between Johnson noise and blackbody radiation. Dicke's picture, showing the equivalence of Johnson noise and blackbody radiation.

enclosed by a blackbody cavity, and the conductor and the blackbody are at the same temperature, $T_R = T_{bb}$. The conductor impedance R, transmission line characteristic impedance R_0, and the antenna radiation impedance are matched, so that there is no standing wave on the line; traveling waves in the line will be eventually absorbed by the conductor or passed out from the antenna. The Johnson noise power generated by the conductor is delivered to the antenna, emitted, and then absorbed by the blackbody enclosure. Similarly, the blackbody radiation power picked up by the antenna is transferred to the conductor, where it is absorbed. The two powers have to be the same, otherwise the conductor would either gain or lose power, which violates the second law of thermodynamics. The radiation generated by the cavity is three-dimensional with the density of state given by eqn.(2.2), which is proportional to $4\pi^2\nu^2/c^3$ or $4\pi^2 c/\lambda^2$, where λ is the wavelength of the corresponding electrical wave. However, the absorption cross section of the antenna is $\lambda^2/4\pi$. Thus, with this factor canceled out in the density of states of the 3D radiation, the effective power spectral density of the blackbody radiation intercepted by the antenna takes the form of that of the one-dimensional blackbody radiation given in eqn.(2.7). The temperature of resistor is defined as the "antenna temperature". This concept was

utilized by Dicke in detecting the temperature of radiating objects by measuring their thermal radiation with a microwave radiometer (Dicke 1946, Dicke et al. 1946). The antenna of the radiometer picks up thermal radiation of the object under study, and the change of the "antenna temperature" measures the temperature of the object.

If the above concept is used in a reverse manner, a resistor is then a one-dimensional blackbody photon source; the Johnson noise transmitted by the resistor at temperature T_R through a transmission line to a matched load is equivalent to the thermal radiation of a one-dimensional blackbody (eqn.(1.7)) at the same temperature $T_{bb} = T_R$, and the radiation consists of electromagnetic waves or photons of all frequencies. The output photon power of such a source can be readily varied by changing the resistor temperature.

In our on-chip calibration scheme, we use a thin metal film as the resistor blackbody photon source. The calibration of our ultrasensitive cryogenic sub-millimeter detectors require calibration sources that are very accurate, sensitive, fast, and easy to couple to the detectors at cryogenic temperatures. At low temperatures ($< 1\,K$), such sources, due to the weak electron-phonon interaction in metal, satisfy all the above requirements. More details of the source and the underlying physics — the electron-phonon interaction in disordered thin metal films are given in Chapter 3 and in Chapter 5.

Chapter 3

Theoretical background on electron-phonon decoupling in disordered metal films

This chapter covers the theoretical background of this thesis work—the electron-phonon interaction in normal metal thin films. In particular, the interaction is studied at very low temperatures, $\lesssim$1 K, where the resistivity of the films are dominated by impurities; the films are in the *disordered* regime. We begin the chapter with a simplified thermal model of a thin metal film resistor on an insulating substrate. Various possible electron scattering mechanisms and electron cooling processes within the model are discussed in the second section; they include the the electron-electron scattering, the electron-phonon scattering, the electron-impurity scattering, and the electron diffusion. In the third section, we present more details on their contributions to the electron heating and cooling. The main focus of the chapter is the available theories of the electron-phonon interaction; both "clean" and "dirty" limits are discussed in details in the fourth section, together with some examples of the experiments that can be explained by the theories. We also discuss the radiation cooling of electrons in the low temperature thin film. Another important thermal process in the model, the Kapitza boundary heat conductance between the solid metal-insulator interface,

is discussed in the sixth section. As a related topic, the electronic heat capacity of the thin metal film is reviewed in a later section; it can be derived from our electron-phonon interaction measurement. In the last section, we discuss the applications of thin metal films in phonon cooled hot electron blackbody photon sources.

3.1 Thermal model of metal thin film resistors on insulating substrates

In this section we discuss the simply ideal thermal model of thin normal metal film resistor wires on insulating (Si/SiO_2) substrates, as depicted in Fig.3.1(a). The substrate is tightly coupled to the thermal reservoir (a Cu sample holder of volume ~ 1 cm^3). A large conducting lead is connected to either end of the resistor, acting both as an electron reservoir and a wire bonding pad for electrical connections. A voltage source is applied across the resistor at the leads to inject Joule power into the system.

The device can be considered as a thermodynamic system that is composed of several subsystems (Roukes et al. 1985, Wellstood et al. 1994), interacting with one another through heat transfer, as illustrated in the simple ideal thermal model in Fig.3.1(b). These subsystems are the resistor wire, conducting leads, substrate phonons and thermal bath phonons; the resistor wire and the conducting leads are further divided into electron and phonon subsystems. Each of these subsystems is associated with two properties, the temperature and the heat capacity, denoted as T and C respectively. In the wire, the electrons are coupled to the phonons by a thermal link, whose strength is measured by the electron-phonon heat conductance G_{e-ph}. The electrons also transfer heat to the electrons in the leads by out diffusion with the conductance G_{diff}. In addition, there is heat flowing between the phonon subsystems at the metal-substrate interface and the substrate-thermal bath interface.

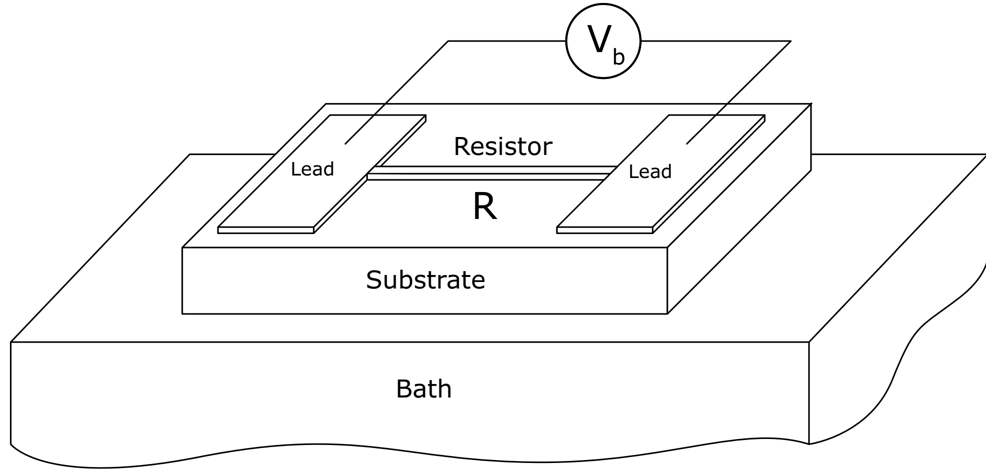

(a) Metal thin film resistor on insulating substrate

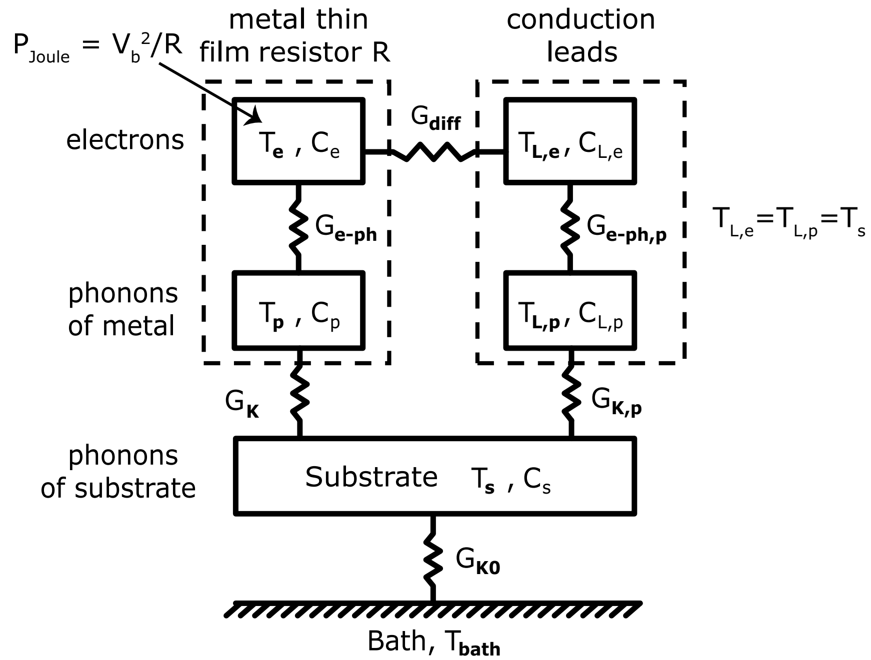

(b) Simple thermal model of the thin film resistor, R. P_{Joule} is the Joule power injected into the resistor by the bias voltage. The temperatures of the electrons, phonons in the metal wire, the electrons and phonons in the leads, phonons in the substrate, and phonons in the thermal bath are T_e, T_p, $T_{L,e}$, $T_{L,p}$, T_s, and T_{bath} respectively. The corresponding heat capacities are C_e, C_p, $C_{L,e}$, $C_{L,p}$ and C_s respectively.

Figure 3.1: Metal thin film resistors on insulating substrates.

Such interactions are characterized by the Kapitza boundary conductances G_K and G_{K0} respectively. Besides the above thermal mechanisms for electron cooling, the electrons can also cool down by electromagnetic radiation (or blackbody radiation). However, the effect of this cooling is only prominent at very low temperatures (<100 mK) and for very small film volumes ($\sim 0.1 \mu m^3$). We will discuss this in later sections. Note that, due to the large volume of the leads, the electrons in them transfer heat to the phonons very efficiently. Also, due to the large contact area between the lead and the substrate, the phonons in the leads are strongly coupled to the substrate phonons. Hence, we have $T_{L,e} = T_{L,p} = T_s$.

Joule power $P_J = V_b^2/R$ can be applied to heat the electrons by the external voltage source V_b, R being the resistance of the resistor. A steady-state is achieved in the electron subsystem at temperature T_e when the electrons transfer the same amount of total power to the phonons of the metal, P_{e-ph}, and to the leads. These phonons are thus heated and finally arrive at a steady state temperature T_p, when a power $P = P_{e-ph}$ flows to the substrate phonons. Similarly, the substrate phonons eventually transfer this amount of power to the thermal bath and attain a well-defined temperature T_s, which is different from the bath temperature T_{bath}. If $G_{diff} \ll G_{e-ph}$, the thermal power flows from the electrons to the phonons in the metal, $P_{e-ph} = P_{Joule}$, and the temperatures of different subsystems in general have the relation $T_{bath} < T_s < T_p < T_e$. The electrons are only cooled through electron-phonon interaction. However, if $G_{K0} \gg G_K \gg G_{e-ph}$, the relation becomes $T_{bath} = T_s = T_p < T_e$. In this case, the phonon subsystems are considered as a single phonon system, with a single temperature T_{bath}. In the next few sections, we give the related theories to show how these conditions can be satisfied.

3.2 Interactions of electrons with the surroundings in disordered metal films

The metal films we are interested in are diffusive systems, whose electrons are constantly doing free motion unless interfered by any scattering with their surroundings, with certain probability. During the scattering, momenta and/or energy are exchanged. The scattering events include the electron-electron scattering, the electron-phonon scattering, and the electron-impurity scattering. These scattering processes determine the thermal characteristics of the electron gas and the resistivity of the metal. In particular, at low temperatures, the electrons are predominantly scattered by the impurities, which results in a temperature independent resistivity. The metal film is thus referred to be in the *disordered* regime. In this section, our discussion focuses on the electronic scatterings in metal thin films in this regime.

3.2.1 Electron-electron scattering in disordered metal films

On average, a conduction electron collides with another conduction electron inelastically with a probability τ_{ee}^{-1} per unit time, and energy is exchanged between the two electrons. As a result, the electron gas eventually achieves a thermal distribution with a well-defined electron temperature T_e. In disordered one-dimensional metal wires (Wind et al. 1986, Altshuler et al. 1982, Altshuler & Aronov 1985, Kozhevnikov 2001) and two-dimensional metal thin films (Santhanam et al. 1987, Burke 1997), the electron-electron scattering rates at low temperatures are given by

$$1D \qquad \tau_{e-e}^{-1} = \left(\frac{R_\Box}{\sqrt{2}(\hbar/e^2)} \frac{k_B}{\hbar} \frac{\sqrt{D}}{W} \right)^{2/3} T^{2/3} \approx 4 \times 10^8 T^{2/3} \tag{3.1a}$$

$$2D \qquad \tau_{e-e}^{-1} = \frac{e^2 R_\Box}{2\pi\hbar^2} k_B T \ln T_1/T \approx 1 \times 10^8 R_\Box T, \tag{3.1b}$$

where $R_\square$ is the residue sheet resistance of the film, D is the diffusion constant, W is the width of the wire, and T_1 is a constant of the order of 10^{12} K (Santhanam et al. 1987)[1], and for the temperatures we are interested in , ~ 1 K, the quantitity $\ln(T_1/T) \sim 30$. The above estimations are made for $R_\square = 2\Omega$, $W = 0.5\,\mu m$, and $D = 50\,cm^2/s$, which are the typical parameters for the devices being discussed in this work.

3.2.2 Electron-phonon scattering rate

The electrons also scatter from the vibrating ions. In this inelastic interaction, the electrons lose energy to the lattice by emitting phonons at a probability of τ_{e-ph}^{-1} per unit time. While the theory for electron-phonon interaction in pure[2] metal is well-understood, the theories for the electron-phonon interaction at low temperature disordered metal thin films are not well-tested; the experimental results do not always agree with the theoretical predictions. However, we can use the widely accepted result from Echternach et al. (2002) to estimate the electron-phonon scattering rate for thin disordered Au ($\sim$ 20 nm) films as follows[3]

$$\tau_{e-ph}^{-1} \approx 2 \times 10^8 T^3. \tag{3.2}$$

3.2.3 Electron-impurity scattering

In an impure metal film sample, the conduction electrons interact with the impurities in the film. These impurities include the impurity atoms, lattice defects, and boundaries (grain boundaries and surface boundaries, since the sample is not infinitely

[1] The value is quoted in the paper for Al(Santhanam et al. 1987). Here, for the purpose of rate estimation, we assume the value for Au is similar, within an order of magnitude.

[2] Bulk metal without any form of impurities or defects.

[3] Santhanam & Prober (1984) measured the electron-phonon interaction for Al thin films and obtained $\tau_{e-ph} \approx 2 \times 10^7 T^3$, which gives a similar power law temperature dependence as Echternach et al. (2002) results on Au thin films.

large). If the impurities are static, the electrons interact with the impurities elastically; the electrons do not exchange energy with the impurities, only their momenta are altered[4]; the scattering rate τ_{e-imp}^{-1} is a temperature independent quantity, and can be estimated as follows. At very low temperatures, the electron-impurity scattering dominates the electronic scatterings, since the temperature dependent electron-electron and the electron-phonon interactions are "frozen". In this case, there exists a temperature independent residue resistivity in the film, $\rho_0 = (\mathrm{m/ne^2})\tau_{e-imp}^{-1}$. Thus, for $\rho_0 = 4\ \mu\Omega \cdot cm$ (for a 20 nm Au films with a residue sheet resistance $R_\Box = 2\ \Omega$), the elastic electron-impurity scattering rate is $\tau_{e-imp}^{-1} \approx 5 \times 10^{13}\, s^{-1}$.

3.2.4 Comparison of rates

Since the electron-impurity scattering rate is temperature independent, while both the electron-electron and electron-phonon scattering rates drop as temperature decreases, there must be a temperature below which the electron-impurity is the dominant scattering process. In Fig.3.2, we compare the three scattering rates. For temperatures above ~50 K, the electron-phonon scattering rate dominates. However, $\tau_{e-imp}^{-1} \gg \tau_{e-e}^{-1}, \tau_{e-ph}^{-1}$ below 50 K, as indicated by the crossover point at the upper right corner of the plot. Therefore, the film enters the disordered regime. Furthermore, as the temperature drops below ~1 K, the electron-phonon scattering rate even drops below the electron-electron rate, thus becoming the weakest thermal process for the electrons.

Characteristic lengths

The scattering processes in the diffusion limit are often studied in terms of the characteristic lengths: the electron-electron length L_{e-e}, the electron-phonon length L_{e-ph},

[4]There are also vibrating impurities that move with the vibrating phonons. In this case, the electron-impurity scattering is inelastic.

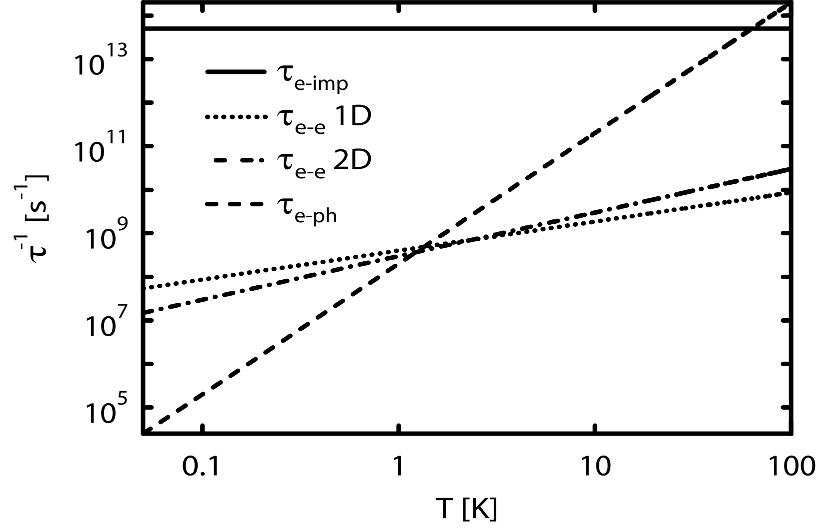

Figure 3.2: The comparison of electronic scattering rates.
The rates are for electron-electron, electron-phonon, and electron-impurity scattering.

and the elastic mean free path ℓ. The electron-electron length, $L_{e-e} = \sqrt{D\tau_{e-e}}$, is the average length a conduction electron can travel before it equilibrates with other electrons, D being the 3D diffusive constant. This sets the minimal length for a metal wire whose electrons can reach a steady state, and a meaningful electron temperature can be defined along the wire. The electron-phonon length, $L_{e-ph} = \sqrt{D\tau_{e-ph}}$, is the average length an electron will diffuse before emitting a phonon. The elastic mean free path, $\ell = v_F\tau$, is the average distance an electron will diffuse, before undergoing an elastic scattering. Here v_F is the Fermi velocity, and τ is the electron elastic time, which is the average time the electron can avoid an elastic collision with any surroundings. In the disordered regime, $\tau = \tau_{e-imp}$, and $\ell \ll L_{e-e}$, $\ell \ll L_{e-ph}$. Note that, in very thin metal films (~ 100 Å), the electrons collide with the surface boundaries very frequently, thus the mean free path is set by the film thickness. Therefore thin metal films are always in the disordered regime at low temperatures.

3.3 Electron Joule heating

The heating of the conduction electrons in disordered metal films are determined by the scattering processes described above. When an electrical field **E** is established across the resistor by the bias source (V_b), the electrons in the resistor are accelerated by the electrical force -e**E**. Except in superconductors, any form of electronic scattering interrupts the motion of the electrons, setting up a finite resistance R, and the Joule power $P_J = V_b^2/R$ is dissipated in the resistor. According to the Mthiessen's rule (Ashcroft & Mermin 1976), the effective electronic scattering rate τ_e^{-1} depends on these rates as

$$\tau_e^{-1} \geqslant \tau_{e-e}^{-1} + \tau_{e-ph}^{-1} + \tau_{e-imp}^{-1} \tag{3.3}$$

and the resistivity of the resistor is

$$\rho = \frac{m}{ne^2}\tau_e^{-1}, \tag{3.4}$$

where m is the electron mass, and n is the conduction electron concentration. The equality only holds if the different processes do not interfere[5]. Thus, in general, the electrons heat up by absorbing energy from the electrical field, while they are losing energy to their surroundings. At the disorder regime, however, the resistivity of the films is established solely as a result of the *elastic* electron-impurity scattering. It involves only momentum exchange but no energy exchange of any form. Therefore, Joule heating is a pure heating process in this regime, with no electron cooling taking place.

[5] It will be shown in the next section that this is barely the case for disordered metal thin films at low temperatures, where a wide variety of interference processes are generated.

3.4 Electron cooling

The electrons would keep heating up unless there are electron cooling channels; the electrons need to lose energy during inelastic scattering or by diffusing into the leads at the ends.

3.4.1 Electron cooling by inelastic scattering

Electron-electron scattering and electron-phonon scattering are the inelastic processes that can possibly cool down the hot electrons. The electron-electron interaction, however, is an "internal" interaction, during which the electrons redistribute energy among themselves, eventually the electron gas arrives at a steady-state Fermi-Dirac energy distribution, and electron temperature T_e can be defined along the wire. Therefore, the electron-electron scattering is only effective for thermalizing the electrons; it does not help to cool down the electron gas as a whole system.

The less frequent electron-phonon interaction ($\lesssim$ 1 K), on other hand, is an inelastic process that causes heat to flow from the hotter electron gas to the cooler phonons of the metal, consequently cools the electron gas. The electron-phonon cooling power depends on the actual electron temperature; the higher the temperature, the higher the power. It increases as the electrons heat up by absorbing energy from the electrical field. As a result, the phonons cooling efficiency keeps growing until $P_{e-ph} = P_{Joule}$, so that the electrons and the phonons reach a steady state. The cooling power P_{e-ph} usually takes the form

$$P_{Joule} = P_{e-ph} = \Sigma V \left(T_e^{p+2} - T_p^{p+2}\right), \tag{3.5a}$$

where Σ is determined by the material, V is the volume of the film, and p is a number from 2 to 4, depending on the level of disorder of the film (Sergeev et al. 2002). The

first equality hold for steady state, and it can be equally expressed in terms of the bias voltage

$$\frac{V_b^2}{R} = \Sigma V \left(T_e^{p+2} - T_p^{p+2}\right). \tag{3.5b}$$

The electron-phonon scattering rate is

$$\tau_{e-ph}^{-1} = \alpha T_e^p, \tag{3.5c}$$

α being a material dependent parameter. Another related quantity that is often used to measure the cooling strength, is the electron-phonon heat conductance which is defined as follows

$$G_{e-ph} \equiv \frac{dP_{e-ph}}{dT_e} = (p+2)\Sigma V T_e^{p+1}. \tag{3.5d}$$

It should be pointed out that the above discussions are based on a couple of assumptions. First, the eqns.(3.5) describe the electron-phonon interaction in terms of the electron temperature T_e, which is meaningful only if the electrons are in equilibrium among themselves, and they can be described by a Fermi–Dirac distribution. It requires the length of the wire to be longer than the electron-electron length, $L > L_{e-e}$. Second, in order for the relation $P_{e-ph} = P_{Joule}$ to hold in steady state, the electron-phonon interaction should be the only cooling mechanism. This is certainly not the case when the metal thin film wire has conducting leads at the ends, as the electrons in the wire can diffuse into the leads, causing the electrons to cool effectively. If $L \gg L_{e-ph}$, the electron gas is still largely cooled through electron-phonon interaction; only a small fraction of electrons within distance $\sim L_{e-ph}$ from the ends are cooled by out diffusion. If $L \ll L_{e-ph}$, the electron gas is mainly cooled through out-diffusion, unless the diffusion is " turned off ", in which case, the electron gas is only cooled through electron-phonon interaction. Devices in both regimes are suitable for studying of the electron-phonon interaction, since it is the dominant electron

cooling process.

3.4.2 Electron-Phonon Cooling in Long Diffusive Wires

The theory for diffusive cooling of a long diffusive metal wire, with or without electron-phonon cooling, is nicely described in details in Burke (1997). Here, we just summarize some of the key results that are importance to this thesis work.

When the electron out-diffusion cooling is under consideration, the long diffusion metal wire should be treated as a distributed thermal system; the electron temperature is a spatial dependent quantity, i.e. $T_e = T_e(x)$, where x is the position along the wire.

DC heating without electron-phonon cooling

For DC heating, in the absence of electron-phonon cooling, the heat flow due to the electron out diffusion is related to the electron temperature $T_e(x)$ by the heat-diffusion equation

$$p_{in} = -\frac{d}{dx}\left(g_{diff}\frac{dT_e(x)}{dx}\right), \tag{3.6}$$

where p_{in} is the input Joule power density (P_{Joule}/Volume) applied to the electrons, and R.H.S. is the diffusion power. g_{diff} is the diffusion heat conductivity, and is related to the wire's electrical conductivity $Volume/R$ by the Wiedemann Franz law

$$g_{diff} = \mathcal{L}\frac{Volume}{R}T, \tag{3.7}$$

where $\mathcal{L} = 2.45 \times 10^{-8}$ WΩ/K^2 is the Lorentz number. The wire lies between x=0 and x=L, and the boundary conditions are $T_e(x = 0, L) = T_{bath}$. The electron temperature profile can be obtained by solving the equation analytically. The details of the profile is not of great important to us; what will be measured is the average electron temperature change induced by the input. Therefore we can define an average

temperature $\langle T_e \rangle_x$ for the electrons in the wire,

$$\langle T_e \rangle_x = T_{bath} \left(1 + \frac{P_{Joule} R}{12 \mathcal{L} T_b^2} \right), \qquad weak\ heating\ P_{Joule} < \mathcal{L} T_b^2 / R \tag{3.8a}$$

$$= T_{bath} \frac{\pi}{8} \sqrt{\frac{P_{Joule} R}{\mathcal{L} T_b^2}}, \qquad strong\ heating\ P_{Joule} > \mathcal{L} T_b^2 / R \tag{3.8b}$$

and an effective diffusive heat conductance G_{eff}

$$G_{eff} = \frac{\partial P_{Joule}}{\partial \langle T_e \rangle_x} = \frac{12 \mathcal{L} T_{bath}}{R}, \qquad P_{Joule} < \mathcal{L} T_b^2 / R \tag{3.9a}$$

$$\approx \frac{13 \mathcal{L} T_{bath}}{R}, \qquad P_{Joule} > \mathcal{L} T_b^2 / R \tag{3.9b}$$

Weak AC heating without electron-phonon cooling

Similarly, when the wire is under AC heating, without electron-phonon cooling, the system can be described by the time dependent heat balance equation

$$p_{in}(t) = -\frac{\partial}{\partial x} \left(g_{diff} \frac{\partial T_e(x,t)}{\partial x} \right) + \frac{\partial (c_e T_e(x,t))}{\partial t}, \tag{3.10}$$

where c_e is the electronic heat capacity per volume. The input power here consists of a DC heating power and a small AC excitation, $p_{in} = (P_{DC} + P_{AC} e^{i\omega t})/Volume$. At the low frequencies that we are interested in, i.e. $\omega < \pi^2 D/L^2$ (D is the diffusion constant), the effective electron temperature and the effective diffusive heat conductance derived from the above approximately take the forms of those for the weak DC heating.

Another important result pointed out by Burke (1997) is that, under weak AC heating, the crossover from electron-phonon cooling and diffusive cooling occurs at $L = \pi L_{e-ph}$.

DC heating with electron-phonon cooling

In real devices, both diffusive cooling and electron-phonon cooling exist. The heat balance equation is thus written as

$$p_{in} - p_{out} = -\frac{d}{dx}\left(g_{diff}\frac{dT_e(x)}{dx}\right), \tag{3.11}$$

where p_{out} is the electron-phonon cooling power density $P_{e-ph}/Volume$. The equation can be solved numerically by using "Relaxation Method" for two-point boundary problems (Press et al. 2002).

We will not show the results for the electron temperature simulation here, but we have two important conclusions from the simulations: 1). For metal wires with length $L > \pi L_{e-ph}$, there is a uniformly distributed electron temperature along the wire, except for about πL_{e-ph} from the ends, and the electrons are predominantly cooled by phonons; the wire is in the electron-phonon interaction regime. 2). For metal wires with length $L < \pi L_{e-ph}$, the electron temperature varies significantly along the wire. The electrons are predominately cooled by diffusing into the conducting leads. The effective diffusion heat conductance is much larger than the electron-phonon heat conductance. Thus, the wire is in the diffusion cooled limit.

In order to study the electron-phonon interaction in diffusive metal wires with normal conducting leads, it is desirable to have wires whose length $L > \pi L_{e-ph}$. This strongly limits the minimal size the of the film we can study. Especially at very low temperatures, the electron-phonon length are very long; at 100 mK, L_{e-ph} can be as long as 300 μm, the wire length then has to be $\sim$ 1 mm.

3.4.3 Electron-Phonon Interaction in SNS Structures

In order to study the electron-phonon relaxation in metal thin films shorter than πL_{e-ph}, it is desirable to make the effect of electron out-diffusion cooling negligible.

This can be realized by using superconductors as the conducting leads. The thermal flow is then blocked due to the Andreev reflection (Andreev 1964) of the hot electrons at the normal-superconductor (NS) interface, and $G_{diff} \approx 0$.

To give a simple picture, we consider the interface of a normal metal - superconductor as shown in Fig.3.3. An electron below the superconductor energy gap

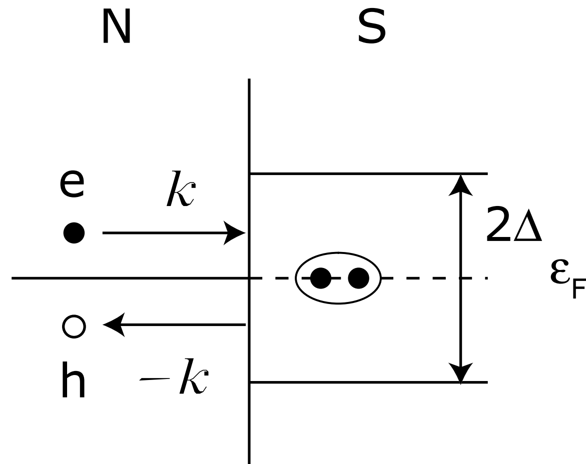

Figure 3.3: Schematic of Andreev reflection at NS interface.

cannot cross the interface. However, an electron with energy in the superconductor gap in the normal metal can enter the superconductor and condense into the ground state of the superconductor as one electron of a Cooper pair. The superconductor requires another electron from the normal metal to complete the pair. As a result, there is a missing electron in the normal metal. One can understand this as the retro-reflection of the electrons by the NS interface, causing a "hole" to emerge in the normal metal. It has opposite charge, and velocity (all three components) with respect to the electron. Thus, there is electrical current flowing across the interface, but the thermal flow is blocked, since the Cooper pairs only carry charge but not entropy, the superconductor leads are thermal opens for the hot electrons.

Given the above properties of the NS interface, we can study the electron-phonon

interaction in nano-scale metal thin films with length $L < L_{e-ph}$. For a thin metal wire that is connected to superconductor leads, as long as the length of the wire $L \gg L_{e-e}$, electron thermal distribution can be established in the wire[6], and a uniform electron temperature can be defined along the wire. Since at the lower temperatures we are interested in, the electron-phonon length $L_{e-ph} \gg L_{e-e}$, it is possible to make a wire whose length $L_{e-ph} > L \gg L_{e-e}$.

3.5 Electron-phonon Interaction in low temperature thin metal films

If the electron out-diffusion is negligible as discussed above, the electrons can only cool through transferring heat to phonons in the metal through electron-phonon interaction. At equilibrium, the heat flow from the electron subsystem to the phonon subsystem P_{e-ph} equals the Joule power injected into the electron gas. For a small electron temperature excursion ΔT_e above the phonon temperature T_p, $P_{e-ph} = G_{e-ph}\Delta T_e$. At room temperature, the electron-phonon heat conductance G_{e-ph} is very high, the power needed to create a noticeable steady state temperature difference between the electrons and the phonons, P_{Joule}, is so high that the metal would be vaporized (Wellstood et al. 1994). However, at low temperatures (sub-Kelvin), the electron-phonon interaction becomes exceedingly weak, i.e. G_{e-ph} is very small $\sim 10^{-11} W/K$, so that the electrons in the metal can stay at a temperature that is significantly higher than the metal phonon temperature — the electrons and phonons are thus decoupled (Roukes et al. 1985).

[6]If the length $L < L_\phi$, where L_ϕ is the electron dephasing length, and at low temperatures it is decided by the L_{e-e}, multiple Andreev reflection (MAR) occurs in the wire, and staircase shape non-thermal electron distributions can be setup in the wire (Pierre et al. 2001).

Electron-phonon interaction is essential for many physical processes in metal, especially in disordered metal thin films at low temperatures, such as electron dephasing (Lin & Bird 2002, Echternach et al. 2002, Pititsina et al. 1997, Santhanam & Prober 1984), hot electron cooling (Roukes et al. 1985, Wellstood et al. 1994), and superconducting branch imbalance (Sergeev & Mitin 2000). However, our knowledge on the electron-phonon interaction in low temperature disordered metal films and micro- and nano- scale system is limited. In this section, we discuss the theories for electron-phonon interaction in low temperature disordered thin metal films, whose electron-phonon scattering rate is largely modified from the well-understood *pure* bulk metal value by the presence of disorders.

3.5.1 Electron-Phonon interaction in *pure* metal

The electron-phonon interaction in *pure* metal is well-understood. It should be stressed that "*pure*" metal is defined as bulk metal without any forms of impurities, such as impurity atoms, lattice defects, boundaries (including grain boundaries and interfaces). Under these conditions, the electrons can interact with real thermal phonons, i.e. phonons due to the the thermal vibrations of the immobile ions on a perfect lattice, if the effects of the impurities can be neglected. The process can be treated as a single particle scattering problem as shown in Fig.3.4. The electron either

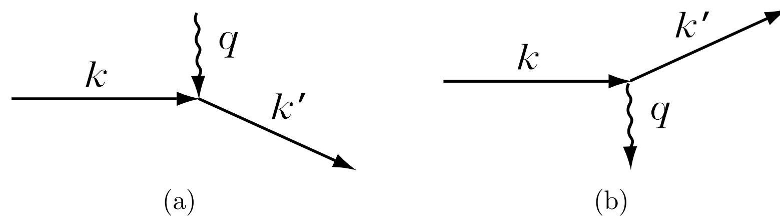

Figure 3.4: Electron-Phonon scattering in *pure* metal.
$\mathbf{k}$ and $\mathbf{k}'$ are the electron wave vectors before and after the scattering, and $\mathbf{q}$ is the phonon wave vector. (a) Absorption of phonon. (b) Emission of phonon.

absorbs a phonon or emits a phonon, under the following conditions: conservation of energy

$$E_{k'} = E_k \pm \varepsilon_q, \tag{3.12}$$

and the conservation of the crystal momentum [7]

$$\mathbf{k}' = \mathbf{k} \pm \mathbf{q} + \mathbf{K}, \tag{3.13}$$

where E_k, $E_{k'}$, and ε_q are the electron energy before and after the scattering, and the energy of the phonon respectively, $\mathbf{k}$, $\mathbf{k}'$, and $\mathbf{q}$ are the corresponding wave vectors, and $\mathbf{K}$ is a reciprocal lattice vector. The "+" sign is for phonon absorption, and the "–" is for phonon emission. The electron energy loss rate by electron-phonon scattering (the rate at which an electron scatters from the electronic state $\mathbf{k}$ to another state by emitting or absorbing a phonon) can be calculated from the Fermi golden rule

$$\begin{aligned} \tau_k^{-1} = \frac{1}{(2\pi)^3} \int \frac{2\pi}{\hbar} \mathbf{M}(\mathbf{k},\mathbf{q})^2 \{ [1 - f(E_{k'})] n(q) \delta(E_{k'} - E_k - \varepsilon_q) \\ + [1 - f(E_{k'})][n(q) + 1] \delta(E_{k'} - E_k + \varepsilon_q) \} dq^3, \end{aligned} \tag{3.14}$$

where $f(E_k)$ is the electron Fermi-Dirac distribution function, $n(q)$ is the phonon Bose-Einstein distribution function and $\mathbf{M}(\mathbf{k},\mathbf{q})^2$ is the interaction matrix element. The first term gives the rate for phonon absorption and the second the phonon emission.

Gantmakher (1974) calculated the rate for *pure* metal at low temperatures that are much smaller than the Debye temperature, where only the lower energy acoustic phonons need to be considered. Furthermore, in the calculation, the interaction matrix is assumed to take the scalar form (Gantmakher 1974, Wellstood et al. 1994)

[7] Assuming the umklapp process is possible (Gantmakher 1974, Wellstood et al. 1994, Ashcroft & Mermin 1976). Actually, this is always true for pure Au, since its Fermi surfaces have necks joining together spheres, and the umklapp process can always occur in the neck regions even at very low temperatures.

$\mathbf{M}(\mathbf{k},\mathbf{q})^2 = (\hbar q/2\rho_m u_l \Omega)(2\varepsilon_F/3)^2$, where ρ_m and Ω are the mass density and volume of the metal, u_l is the longitudinal sound velocity, and ε_F is the Fermi energy. This implies that only the longitudinal branch of the three acoustic phonon modes is significant. Under these assumptions, a cubic temperature dependence of the rate for electrons at the Fermi energy at temperature T was derived

$$\tau_{e-ph}^{-1}(\varepsilon_F, T) = \frac{7\zeta(3)k_B^3}{8\pi\hbar^4 u_l^4 v_F \rho_m \Omega}\left[\frac{2\varepsilon_F}{3}\right]^2 T^3 \propto T^3, \tag{3.15}$$

where v_F is the Fermi velocity, $\zeta(n)$ is the Riemann zeta function, and $\zeta(3) \approx 1.2$. The pre-factor is not of great importance due to the fairly crude approximations.

In fact, it was pointed out later by Reizer (1989) that, the contribution of the two transverse phonon modes could be significant at very low temperatures ($\lesssim 100$ mK). For instance, for a cubic lattice, $u_l = \sqrt{3}u_t$ (u_t is the transverse sound velocity), and $\tau_{e-ph}^{-1}(\varepsilon_F, T)$ increases by a factor about 15 by taking into account the transverse modes. Reizer calculated the electron-phonon interaction rate at Fermi energy and with electron distribution at the temperature of the phonons, by using Keldysh-diagram technique, and obtained the same T^3 law but different pre-factor.

$$\tau_{e-ph}^{-1}(\varepsilon_F, T) = \frac{7\pi\zeta(3)\beta_l k_B^3}{\hbar^3(k_F u_l)^2}\left[1 + \frac{16}{\pi^2}\left(\frac{u_l}{u_t}\right)^4\right] T^3, \tag{3.16}$$

where k_F is the Fermi wave vector, and β_l is a constant that characterize the electron-longitudinal phonon interaction, with the form

$$\beta_l = \left(\frac{p_F v_F}{3}\right)^2 \frac{D(\varepsilon_F)}{2\rho_m u_l^2}, \tag{3.17}$$

where p_F is the Fermi momentum, and $D(\varepsilon_F)$ is the electron density of states at the Fermi energy. The cubic temperature dependence results have been used to explain experimental data of Roukes et al. (1985) and Wellstood et al. (1994). However in both cases, the samples can hardly be treated as *pure* metal due to the very

small thickness of the samples. A possible explanation is that the samples are in the intermediate-disorder regime for transverse phonons (Sergeev & Mitin 2000, Lin & Bird 2002), see § 3.5.3.

3.5.2 Impurity modifications to electron-phonon scattering

The electron-phonon interaction is strongly influenced by the presence of impurities, which include impurity atoms, lattice defects, and boundaries (grain boundaries and interface/surface boundaries). In the thin metal films we are interested in, due to the extremely small film thickness (∼10–20 nm), the effect of the surface boundaries as impurities is significant. Therefore, regardless how few impurity atom and defects, the thin metal films are always in the disordered regime. In this section, we focus our discussion on the electron-phonon interaction in disordered metal thin films at low temperature. The disordered films are further divided into three categories: 1. The "clean" limit (or "clean" metal), where $q_{T,l(t)}\ell > 1$, $q_{T,l(t)}$ being the wave vector of the longitudinal (transverse) thermal phonon, and ℓ being the electron mean free path. 2. The "dirty" limit (or "dirty" metal), where $q_{T,l(t)}\ell < 1$. 3. The moderate disordered regime, where $q_{T,l(t)}\ell \sim 1$. Note that, for *pure* metal, the quantity $q_{T,l(t)}\ell$ goes to infinity.

In disordered metal thin films, along with the "pure" inelastic electron- thermal phonon interaction, there are a couple of other basic processes — the electrons' scattering from impurities and the elastic electron scattering. These scattering mechanisms, interfere among themselves and modify the electron-phonon interaction drastically from that of the *pure* metals.

It was first observed by Pippard (Pippard 1955, Lin & Bird 2002) in his ultrasonic attenuation experiment, that the phonon-electron interaction (the actual measured

quantity is the ultrasonic attenuation coefficient) depends on impurities and weakens as $q_{T,l}\ell$ decreases, where $q_{T,l}$ is the wave vector of the thermal longitudinal phonon, and ℓ is the electron mean free path. For a "dirty" metal ($q_{T,l}\ell < 1$), the phonon-electron interaction rate τ^{-1}_{ph-e} is weakened by a factor of $q_{T,l}\ell$ from its pure metal value. From the energy balance equation (Reizer 1989) $C_e\tau^{-1}_{e-ph} = C_p\tau^{-1}_{ph-e}$, the electron-phonon interaction rate also has such a dependence on $q_{T,l}\ell$. An intuitive explanation for such weakening is given by Lin & Bird (2002) as follows. In "dirty" metals, the electron mean free path ℓ is very short, which imposes an uncertainty for the magnitude of the electron wave vector k on the order of $\Delta k \sim \ell^{-1}$. Thus, if the change of the electron wave vector is smaller than Δk, during its scattering with phonons, the initial and final wave vectors are indistinguishable, and the electron is effectively not scattered. Thus the phonons with wave vector $q_{T,l} < \ell^{-1}$ are inefficient in scattering electrons. Schmid (1973) theoretically calculated the electron-phonon scattering rate for such "dirty" metals, and predicted a $T^4\ell$ dependence, by considering the inelastic scattering of electrons with complete phonon dragged vibrating impurities. This agrees with Pippard's results. The $T^4\ell$ dependence is observed in "dirty" films from a few materials experimentally: Bi by Komnik et al. (1994), Hf and Ti thin films by Gershenson et al. (2001), and Au and Cu films by Karvonen et al. (2004). However, the T^2 and T^3 dependence are commonly found in the experiments for other disordered films (Gershenzon et al. 1990, Dumpich & Carl 1991, Santhanam & Prober 1984, Roukes et al. 1985).

3.5.3 Electron-phonon interaction in disordered metals

In this section, we summarize the key results from a more systematic theory for the electron-phonon interaction in disordered metals by Sergeev & Mitin (2000). The

theory suggest that the electron-phonon interaction rate has a possible power law dependence on the temperature $\tau_{e-ph}^{-1} = T^n$, with n=2–4. In their work, they further divided the impurity scatterers into static (non–vibrating) impurities (e.g. heavy impurity atoms, rigid interface) and vibrating impurities (e.g. light impurity atoms, vibrating boundaries). The interaction of the electron–static impurities is elastic. Together with other static scattering potential, it decides the elastic relaxation rate; the total static potential is the sum of the two. The elastic electron scattering enhances the interaction of electrons with transverse phonons. Under the assumption that the electron interaction with such static potentials are random and short range, an electron elastic mean free path $\mathcal{L}$ is defined for the static potentials, i.e. the average distance an electron can travel without scattering from static potentials, while ℓ is the total electron mean free path. The quantity $\ell/\mathcal{L}$ gives the fraction of the static potential. For instance, if all of the scattering potential is static, than $\mathcal{L} \rightarrow \ell$, thus $\ell/\mathcal{L} \rightarrow 1$. On the other hand, if there is no static potential, $\mathcal{L} \rightarrow \infty$, and $\ell/\mathcal{L} \rightarrow 0$. The electrons also interact vibrating impurities. These impurities give vibrating scattering potentials for electrons. The potentials are inelastic for the electrons and they are assumed to move in phase with the host lattice; it is said the impurities are *dragged by phonons.*

The electrons interact with both longitudinal and transverse phonons. The electron-phonon interaction rate for a single electron at the Fermi energy at temperature T is given as follows. For electron-longitudinal phonon scattering

$$\tau_{e-ph,l}^{-1}(\varepsilon_F, T) = \frac{7\pi\zeta(3)}{2}\frac{\beta_l(k_BT)^3}{\hbar^3(k_Fu_l)^2}F_l(q_{T,l}\ell), \tag{3.18a}$$

where

$$F_l(z) = \frac{2}{7\zeta(3)}\int_0^{k_B\theta_D\ell/\hbar u_l z} dx\Phi_l(xz)(n(x)+f(x))x^2, \tag{3.18b}$$

and

$$\Phi_l(x) = \frac{2}{\pi}\left[\frac{x\arctan(x)}{x-\arctan(x)} - \left(1-\frac{\ell}{\mathcal{L}}\right)\frac{3}{x}\right]. \tag{3.18c}$$

$n(x)$ and $f(x)$ are the Bose-Einstein and Fermi-Dirac distribution function for phonons and electrons respectively, $\Phi_l(x)$ is the Pippard function, θ_D is the Debye temperature, and the dimensionless constant for electron-longitudinal phonon interaction β_l is defined in eqn.(3.17). The rate due to electron interacting with transverse phonons is

$$\tau^{-1}_{e-ph,t}(\varepsilon_F, T) = \frac{3\pi^2\beta_t(k_BT)^2}{\hbar^2(k_Fu_t)(k_Fl)}\left(1-\frac{\ell}{\mathcal{L}}\right)F_t(q_{T,t}\ell), \tag{3.19a}$$

where

$$F_t(z) = \frac{4}{\pi^2}\int_0^{k_B\theta_D\ell/\hbar u_t z} dx\Phi_t(xz)(n(x)+f(x))x, \tag{3.19b}$$

and

$$\Phi_t(x) = 1 + \left(1-\frac{\ell}{\mathcal{L}}\right)\left(\frac{3x-3(x^2+1)\arctan(x)}{2x^3}\right). \tag{3.19c}$$

The dimensionless constant $\beta_t = (p_Fv_F/3)^2/(D(\varepsilon_F)/2\rho_m u_t^2) = \beta_l(u_l/u_t)^2$. The electron-phonon rate $\tau^{-1}_{e-ph}(\varepsilon_F, T)$ is the sum of the above two rates. We now only discuss the electron-phonon interaction in low temperatures, such that $T \ll \theta_D$.

The "clean" limit $q_T\ell > 1$

In the clean limit, where $q_{T,l}\ell > 1$, and $q_{T,t}\ell > 1$ ($q_{T,t}$ is the transverse phonon wave vector), and at temperature $T \ll \theta_D$, the electron-phonon scattering rate is given by

$$\tau^{-1}_{e-ph}(\varepsilon_F, T) = \frac{7\pi\zeta(3)}{2}\frac{\beta_l(k_BT)^3}{\hbar^3(k_Fu_l)^2}\left[1+\frac{6\pi\hbar u_l}{7\zeta(3)k_BT\ell}\left(1-\frac{\ell}{\mathcal{L}}\right)\left(\frac{u_l}{u_t}\right)^3\right]. \tag{3.20}$$

The first term comes from the contribution of the electron-longitudinal phonon interaction, and the second term comes from the electron-transverse phonon interaction. For pure metal, i.e. $q_{T,l}\ell$, $q_{T,t}\ell \gg 1$, the second term is negligible, thus, the rate recovers Gantmakher's T^3 law shown eqn.(3.15).

The "dirty" limit $q_T\ell < 1$

For "dirty" metal, the conditions $q_{T,l}\ell < 1$ and $q_{T,t}\ell < 1$ are satisfied. The electron-phonon interaction rate reduces to

$$\tau_{e-ph}^{-1}(\varepsilon_F, t) = \frac{\pi^4 (k_B T)^4 \ell \beta_l}{5\hbar^4 k_F^2 u_l^3}\left[1 + \frac{3}{2}\left(1 - \frac{\ell}{\mathcal{L}}\right)\left(\frac{u_l}{u_t}\right)^5\right] + \frac{3\pi^2 (k_B T)^2 \beta_l}{2\hbar^2 k_F^2 \mathcal{L} u_l}\left[1 + 2\left(1 - \frac{\ell}{\mathcal{L}}\right)\left(\frac{u_l}{u_t}\right)^3\right]. \tag{3.21}$$

The first term in both square brackets is from the electron-longitudinal phonon interaction, and the second term is from the electron-transverse phonon interaction. In general $u_l/u_t \sim 2$ (e.g. in cubic lattice, $u_l/u_t = \sqrt{3}$), so the factor $(u_l/u_t)^3$ and $(u_l/u_t)^5$ can easily be in the range of 10–100. Thus, the electron-transverse phonon interaction dominates the scattering rate under most conditions. In other words, the impurities in the disordered metals enhance the electron-transverse phonon interaction.

Complete phonon-drag

If the impurities in the metal are completely dragged by the phonons, i.e. all the impurities are vibrating in the same way with the lattice, then we have $\mathcal{L} \to \infty$, and the factor (1 - $\ell/\mathcal{L}$) $\to$ 1.

For *clean* metals, with low concentration of impurities, we have $q_T\ell > 1$, but not much larger than 1 ($\sim$ 5). The transverse phonons contribution in eqn.(3.20)

is the dominant term, and a $T^2 l^{-1}$ dependence is expected for the electron-phonon interaction rate

$$\tau_{e-ph}^{-1}(\varepsilon_F, T) = \frac{3\pi^2 \beta_l k_B^2}{\hbar^2 k_F^2 u_l} \left(\frac{u_l}{u_t}\right)^3 T^2 l^{-1}. \tag{3.22}$$

This relation is use by Pititsina et al. (1997) for calculating the electron-phonon rate in clean ($l \sim 10\,nm$) Au, Be, Nb, and NbC thin films at relatively high temperature $T \gtrsim 10\,K$, where the clean limit condition is satisfied. For example, for Au film with electron mean free path of the order of 10 nm, $T = 10\,K$, and sound velocity $u \approx 3000\,ms^{-1}$, we have $q_T l \approx 5$. The estimated rates are in good agreement with the experimental results (Au (Dumpich & Carl 1991), Nb (Dalrymple et al. 1986), Be (Pititsina et al. 1997) , NbC (Il'in et al. 1998)).

If the metal is in the *dirty* limit, where $q_T \ell < 1$, the second term of eqn.(3.21) drops out due to the large $\mathcal{L}$. The transverse phonons strongly dominate the relaxation rate, which is given by

$$\tau_{e-ph}^{-1}(\varepsilon_F, T) = \frac{\pi^4 k_B^4 \beta_l}{5\hbar^4 k_F^2 u_l^3} \left[\frac{3}{2}\left(\frac{u_l}{u_t}\right)^5\right] T^4 \ell. \tag{3.23}$$

This gives the same $T^4 \ell$ dependence of the electron-phonon rate on temperature and electron mean free path calculated by Schmid (1973) and Sergeev et al. (1999). The result is in good agreement (within factor of 5) with the data on Ti and Hf thin films on sapphire substrate (Gershenson et al. 2001). The samples are in the deep dirty limit, $q_T l \ll 1$, below $T = 50\,K$. The acoustic impedance of the films and the sapphire substrate are very close, such that the interface vibrates in phase with the film phonons, i.e. the interface is considered as an impurity completely dragged by the film phonons.

Incomplete phonon-drag

In the presence of static scattering potentials, the impurities are not completely dragged by the metal phonons. This corresponds to a finite value of $\ell/\mathcal{L}$. The vibration of the impurities in metal thin films depends on their properties, such as mass, connections with the substrate. In most cases, their vibrations are not much different from that of the lattice, therefore, the ratio $\ell/\mathcal{L}$ is on the order of $10^{-4} - 10^{-3}$ (Sergeev et al. 2002). However, if the thin films are deposited on rigid substrates (e.g. diamond), the interface does not vibrate with the film phonon, and $\ell/\mathcal{L} \sim 0.1$ is possible. So in general, the quantity $(1 - \ell/\mathcal{L}) \lesssim 1$.

In *clean* metals, under the above conditions, the electron-transverse phonon interaction still dominates the electron-phonon scattering. The scattering rate is only slightly modified from eqn.(3.22) by a factor of $(1 - \ell/\mathcal{L})$,

$$\tau_{e-ph}^{-1}(\varepsilon_F, T) = \frac{3\pi^2 \beta_l k_B^2}{\hbar^2 k_F^2 u_l} \left(\frac{u_l}{u_t}\right)^3 \left(1 - \frac{\ell}{\mathcal{L}}\right) T^2 \ell^{-1}. \tag{3.24}$$

Therefore, for disordered metal thin films in the *clean* limit ($q_T \ell > 1$), the electron-phonon rate has a $T^2 l^{-1}$ dependence on the temperature and the electron mean free path, regardless whether the impurities are dragged by the phonons or not.

However, the electron-phonon rate in the *dirty* limit ($q_T \ell < 1$) can be drastically changed by the static scatterers. Due to the large values of $(u_l/u_t)^3$ and $(u_l/u_t)^5$, the contribution of the transverse phonons are still the dominant sources of the relaxation. We rewrite the rate from eqn.(3.21), and ignore the longitudinal part

$$\tau_{e-ph}^{-1}(\varepsilon_F, t) = \frac{3\pi^2 (k_B T)^2 \beta_l}{2\hbar^2 k_F^2 u_l} \left(\frac{u_l}{u_t}\right)^3 \left[\frac{2}{\mathcal{L}} + \frac{\pi^2}{5}\left(\frac{k_B T l}{\hbar u_l}\right)^2 \frac{1}{\ell}\left(\frac{u_l}{u_t}\right)^2\right], \tag{3.25}$$

where $k_B T\ell/\hbar u_l = q_{T,l}\ell$. The ratio of the first and the second term is

$$\frac{\dfrac{\ell}{\mathcal{L}}}{\dfrac{\pi^2}{5}(q_{T,l}\ell)^2\left(\dfrac{u_l}{u_t}\right)^2} \sim \frac{\dfrac{\ell}{\mathcal{L}}}{4(q_{T,l}\ell)^2}. \tag{3.26}$$

If $\ell/\mathcal{L} > 4(q_{T,l}\ell)^2$, then the electron-phonon rate is strong enhanced; it changes from the $T^4\ell$ dependence to the $T^2\mathcal{L}^{-1}$ dependence

$$\tau^{-1}_{e-ph}(\varepsilon_F, t) = \frac{3\pi^2 k_B^2 \beta_l}{\hbar^2 k_F^2 u_l}\left(\frac{u_l}{u_t}\right)^3 \frac{T^2}{\mathcal{L}}. \tag{3.27}$$

Even for very small $\ell/\mathcal{L} \sim 10^{-4}$, this can be achieved for a film deep in the dirty limit ($q_T\ell \sim 0.01$). Hsu et al. (1999) have measured the electron-phonon interaction rate in $Ti_{73}Al_{27}$ alloy, with $q_T\ell \sim 0.006$, and found a T^2 dependence. If $\ell/\mathcal{L} < 4(q_{T,l}\ell)^2$, the rate recovers the form of $T^4\ell$ dependence from eqn.(3.23) for dirty films with complete phonon-drag, with an extra factor of $(1 - \ell/\mathcal{L})$, which is of the order of unity.

The moderate disorder regime $q_T\ell \sim 1$

Besides the above mentioned "clean" and "dirty" limits for the disordered metal thin films, there exits an intermediate regime—the *moderate* disordered regime, where $q_T\ell \sim 1$. The temperature dependence of the electron-phonon rate this regime is more complicated. For a given temperature, if the $q_T\ell \sim 1$ condition is satisfied, the film can enter the *clean* regime for higher temperatures, and *dirty* regime for low temperatures. As a result, the power law temperature dependence of the electron-phonon rate can change from one exponent (4) to another exponent (2) as temperature increases. This is used to explain the famous Roukes' T^3 electron-phonon rate (Roukes et al. 1985) for thin Cu film (Sergeev et al. 2002) with complete phonon-drag, and obtain reasonably good result, as shown in the Fig.3.5. The Cu film in Roukes'

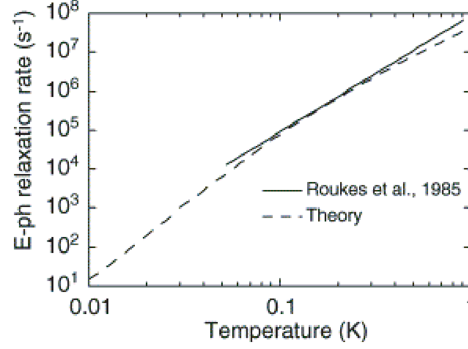

Figure 3.5: The electron-phonon rate in Cu in the moderate disorder regime. The figure is taken from Sergeev et al. (2002). The solid line is a T^3 curve from the results on Cu from Roukes et al. (1985), and the dashed line is calculated by using the theory described (Sergeev & Mitin 2000).

work has electron mean free path $l \sim 200\,nm$. In the measured temperature range $0.025 - 0.32\,K$, the value of $q_T l$ changes from 0.2 (dirty) to 2.6 (clean).

3.5.4 The electron energy loss rate

The expressions for the electron-interaction rate in the above theories are all calculated for single electron processes, where an electron is at the Fermi surface of an electron distribution at temperature T, i.e. the $\tau_{e-ph}^{-1}(\varepsilon_F, T)$. However, in experiments, the measured rate is the actual energy loss rate for the electron gas, which is the average of the single electron value over the electron states $\sim k_B T$. This rate is denoted as τ_{e-ph}^{-1} in this thesis work. The two rates differ by a constant given by Il'in et al. (1998)

$$\tau_{e-ph}^{-1} = a\tau_{e-ph}^{-1}(\varepsilon_F, T) = \frac{3(n+2)\Gamma(n+2)\zeta(n+2)}{2\pi^2(2-2^{-(n-1)})\Gamma(n)\zeta(n)}\tau_{e-ph}^{-1}(\varepsilon_F, T) \tag{3.28}$$

where n is the exponent in the power law dependence of $\tau_{e-ph}^{-1}(\varepsilon_F, T) \propto T^n$. The values of a for different power n's are given in the following Table 3.1.

n	2	3	4
a	1.6	4.5	9.1

Table 3.1: The scaling factors between $\tau^{-1}_{e-ph}(\varepsilon_F, T)$ and τ^{-1}_{e-ph}
$\tau^{-1}_{e-ph}(\varepsilon_F, T)$ is the single electron electron-phonon interaction rate at the Fermi energy and τ^{-1}_{e-ph} is the electron gas energy loss rate.

3.5.5 Summary

To summarize, the theory by Sergeev & Mitin (2000) predicts that the electron-phonon scattering rate in disordered metal films has different power law temperature dependence, and is determined by the level of disorder and the property of the impurities. In the clean limit, independent of the properties of the impurities, the rate has a T^2 dependence. In the dirty limit, with impurities completely dragged by the phonons, the rate depends on the temperature as T^4. If the phonons are incompletely dragged by the phonons, the temperature dependence changes to T^2. Interestingly, in the moderate disordered regime, an approximate T^3 dependence is expected.

Table 3.2 summarizes some of the experimental results on the electron-phonon scattering, whose power law dependence on the temperature has been successfully interpreted by the above theory. However from the above discussion, one can realize that the theory is rather complicated; several factors are coupled together to determine the electron-phonon interaction rate in disordered metal thin films. The measurement temperature ranges for all the experiments listed in Table 3.2 merely expand one order of magnitude. It could be rather deceiving to fit the data with a single power law in such small temperature range. Furthermore, there are still measurements that cannot be reasonable explained by the theory, for instance, the electron-phonon rate of Al measured by Santhanam & Prober (1984), although the film is in the clean limit in the measurement range, the author found a T^3 law could

approximate the data very well. Therefore, the theory should be used with caution, especially for applications that require precise values of the electron-phonon rate (e.g. the phonon cooled HEB and the phonon cooled hot electron photon source), the rate should be verified with careful experiments.

3.6 Electron radiation cooling

In addition to electron thermal cooling mechanisms discussed above, another possible cooling mechanism is through the electromagnetic radiation (Schmidt, Schoelkopf & Cleland 2004*a*), in other words, one-dimensional blackbody radiation. This is the basis for the phonon cooled hot electron blackbody photon source we described in Chapter 3, where the electron thermal fluctuation induced Johnson noise is radiated from the electron gas to the matched detector through electrical connections. What we haven't mentioned in the discussion is that during such photon emission, the source (i.e. the electron gas in the metal thin film) itself is losing energy due to the electrical radiation. If the metal thin film is electrically connected to a matched load, the net radiation power from the electron gas to the load is (Schmidt, Schoelkopf & Cleland 2004*a*)

$$P_\gamma = \int_0^\infty \frac{h\nu}{e^{h\nu/k_B T_e} - 1} d\nu, \tag{3.29}$$

and the corresponding radiation heat conductance is

$$G_\gamma = \int_0^\infty \frac{d}{dT_e} \frac{h\nu}{e^{h\nu/k_B T_e} - 1} d\nu. \tag{3.30}$$

As a good estimate, we can assume the power spectral density of the radiation is that of the classic one-dimensional blackbody (eqn(2.8)), $k_B T_e$, and the bandwidth of the radiation is $k_B T_e/h$. Therefore, the total radiation power from the electron gas

(a) Pure metal ($q_T \ell \to \infty$), $\tau_{e-ph}^{-1} \sim T^3$

τ_{e-ph}^{-1}	Ref.
T^3	Ashcroft & Mermin (1976)
T^3	Gantmakher (1974)
T^3	Reizer (1989)

(b) "Clean" limit ($q_T \ell > 1$), $\tau_{e-ph}^{-1} \sim T^2$

Material	ℓ (Å)	T_{meas} (K)	$q_T \ell$	τ_{e-ph}^{-1}	Ref.
Au	39	5–20	1.5–5.9	T^2	Dumpich & Carl (1991)
Be †	100	10–25	14–36	T^2	Pititsina et al. (1997)
Nb	12	10–25	1–2.5	T^2	Dalrymple et al. (1986)
NbC	40	10–25	1.2–3.0	T^2	Il'in et al. (1998)

(c) "Dirty" limit ($q_T \ell < 1$), complete phonon drag, $\tau_{e-ph}^{-1} \sim T^4$

Material	ℓ (Å)	T_{meas} (K)	$q_T \ell$	τ_{e-ph}^{-1}	Ref.
Au	43	0.1–0.4	0.0047–0.19	T^4	Karvonen et al. (2004)
Bi	25	0.6–1.2	0.11–0.22	T^4	Komnik et al. (1994)
Cu	21	0.1–0.5	0.012–0.048	T^4	Karvonen et al. (2004)
Hf	9	0.04–0.7	0.0025–0.044	T^4	Gershenson et al. (2001)
Ti	23	0.1–0.5	0.01–0.05	T^4	Gershenson et al. (2001)

(d) "Dirty" limit ($q_T \ell < 1$), incomplete phonon drag, $\tau_{e-ph}^{-1} \sim T^2$

Material	ℓ (Å)	T_{meas} (K)	$q_T \ell$	τ_{e-ph}^{-1}	Ref.
Au	4	0.3–20	0.01–0.6	T^2	Dorozhkin & Schoepe (1986)
Nb	12	1.5–15	0.05–0.85	T^2	Gershenzon et al. (1990)
$Ti_{73}Al_{27}$	2	3–22	0.02–0.15	T^2	Hsu et al. (1999)
$Ti_{100-x}Sn_x$	3	3–15	0.021–0.16	T^2	Wu & Jian (1998)

(e) Moderate disordered regime ($q_T \ell \sim 1$), $\tau_{e-ph}^{-1} \sim T^p$ (p∼2–4)

Material	ℓ (Å)	T_{meas} (K)	$q_T \ell$	τ_{e-ph}^{-1}	Ref.
AuCu	200	0.025–1	0.04–1.6	T^3	Wellstood et al. (1994)
Cu	2200	0.025–0.32	0.2–2.6	T^3	Roukes et al. (1985)

Table 3.2: The measured temperature dependence of τ_{e-ph}^{-1} on metal thin films. The data are grouped in different disordered regimes.
† The values are extrapolated from measurement above 30 K.

to the matched load is

$$p_\gamma \approx \frac{(k_B T_e)^2}{h}, \tag{3.31}$$

and the radiation heat conductance is

$$G_\gamma \approx \frac{2k_B^2 T_e}{h}, \tag{3.32}$$

The radiation heat conductance has a linear temperature dependence, while the electron-phonon heat conductance has a stronger temperature dependence, for instance, $G_{e-ph} \propto T_e^4$ from eqn.(3.2). Thus, there could be a crossover temperature, below which the radiation heat conductance dominates. However, the heat conductance is very small; it is insignificant compared to the electron-phonon heat conductance even at 50 mK expect for very small volume of metal films. In Fig.3.6 we compare the radiation and electron-phonon heat conductance for a $0.06\mu m^3$ Au film we measured for this thesis work (device SNS-2). The volume of this device is the smallest of all

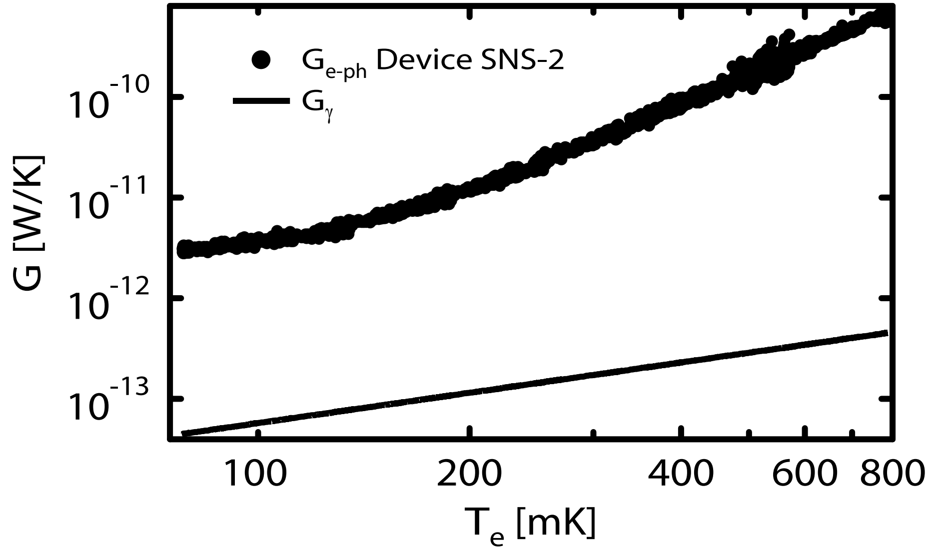

Figure 3.6: The electron radiation heat conductance
The dots are the data for the electron-phonon heat conductance of a $0.06\mu m^3$ Au film, and the solid line is the electron radiation heat conductance.

the devices measured. The plot indicates the electron radiation heat conductance can be ignored in our measurements.

3.7 Metal Film - Insulator Kaptiza Conductance

The thermal boundary conductance between two different materials first drew people's attention in cryogenic experiments, where a temperature discontinuity ΔT at the interface of liquid helium and solid was measured by Kapitza (1941) when passing heat across the boundary, hence the name *Kapitza* thermal boundary conductance. The conductance is defined as follows

$$G_{Kapitza} \equiv I_h/\Delta T, \tag{3.33}$$

where I_h is the heat flowing across the boundary. Subsequently, many experiments have shown that such boundary conductance also exists between solid-solid contacts, such as a metal-insulator contact. For more details, please refer to the review article by Swartz & Pohl (1989) and the references within. In general, the Kapitza heat conductance has the form

$$G_{Kapitza} = ABT^3, \tag{3.34}$$

where A is the area of the contact, and B is a constant depending on the material pair.

The origin of the Kapitza heat conductance is attributed to the dissimilarity of atomic masses and lattices of the two materials being considered. As a result, the phonons have different sound velocities across the boundary. When a phonon arrives at the interface, it can either reflect or transmit into the other media. The goal of the theory is to calculate the probabilities of the phonons to transmit across the interface. There are two major limiting models: the acoustic mismatch theory, where

no phonon is scattered at the interface, and the diffuse mismatch theory, where *all* the phonons which arrive at the interface are scattered. In reality, the effect should be the combination of the two; the two limiting theories set the limits for the Kapitza heat conductance (Swartz & Pohl 1989).

3.7.1 Acoustic mismatch theory

The acoustic mismatch theory by Little (1959) assumes that the media are isotropic 3D continua[8] and the phonons are treated as plane waves[9]. Under these assumptions, a simply analogy can be made to light impinging on the interface of two media; the phonons incident on the interface can specularly reflect, reflect and mode convert, refract or refract and mode convert. The angles of the incidence and the refraction are related to the sound velocities in the two media by the Snell's law. The longitudinal and the two transverse phonon modes can be considered as the light waves of different wavelengths. The total transmission probability is the sum of the refraction.

The acoustic mismatch theory gives a T^3 law for $G_{Kapitza}$, which is consistent with most of the experimental results. However, when the acoustic impedances of the two media are very different Stoner & Maris (1993), the predicted result can be up to 2 orders of magnitude smaller than the experimental value. This is because under this condition, the phonons arrive at the interface do not just specularly reflect; they undergo scattering.

[8]This assumption decides the dimensionality of the phonon density of state, which is similar to that of the photon in blackbody radiation in eqn.(2.2). Thus, a T^3 dependence of $G_{Kapitza}$ is calculated. However, in thin metal films whose thickness is smaller than the phonon wavelength, this assumption fails; the phonons might have reduced dimension spectrum, and thus the T^3 dependence is modified.

[9]This assumption is valid as long as the phonon wavelength is much larger than the interatomic distance of the lattice.

3.7.2 Diffuse mismatch theory

The large discrepancy between the measured G_K and that predicted by the acoustic mismatch theory is explained by Swartz's diffuse mismatch theory (Swartz & Pohl 1989). He pointed out that the quality of the interface affects the Kapitza heat conductance; the phonons can be scattered at the interface and new channels for heat transport are opened. The theory assumes that all the phonons are scattered at the interface, and after the scattering, the phonons lose their "memories" of their previous status. The probability of a phonon scattering into a given side of the interface is completely decided by the phonon density of states. Detailed balance of phonon transport from one side to another is assumed. The diffuse mismatch theory gives an upper limit on the diffusive scattering to $G_{Kapitza}$, while the acoustic mismatch theory gives the lower limit.

3.7.3 Kapitza heat conductance in our system

In our simple device, there is a Kapitza heat conductance G_K between the Au–Si interface. For Au thin film on single crystal Si substrate, the difference of the acoustic impedances of the two are not very large, i.e. within a factor of 5. The calculated G_K from acoustic mismatch and diffuse mismatch theories (Table 3.3) (Swartz & Pohl 1989)) are expected to be similar and the experimental value is expected to be slightly

	Acoustic mismatch	diffuse mismatch
B (W/m^2K^4)	633	794

Table 3.3: Estimated $G_{Kapitza}/T^3$ per unit area
The values are from the acoustic mismatch and the diffuse mismatch theories (Swartz & Pohl 1989).

higher than these values (Stoner & Maris 1993).

At low temperatures ($< 1\,K$), the G_K is expected to be much larger than the electron-phonon heat conductance of a very thin ($\sim$ 100 Å) Au film (Swartz & Pohl 1989). Fig.3.7 gives the comparison of the estimated electron-phonon heat conductance G_{e-ph} from eqn.(3.2), the effective radiation heat conductance G_r and the G_K calculated from the acoustic mismatch theory for a $1000\,\mu m \times 30\,\mu m \times 0.02\,\mu m$ Au film; the G_K is larger than G_{e-ph} by 1-2 orders of magnitudes below 1 K. Under these

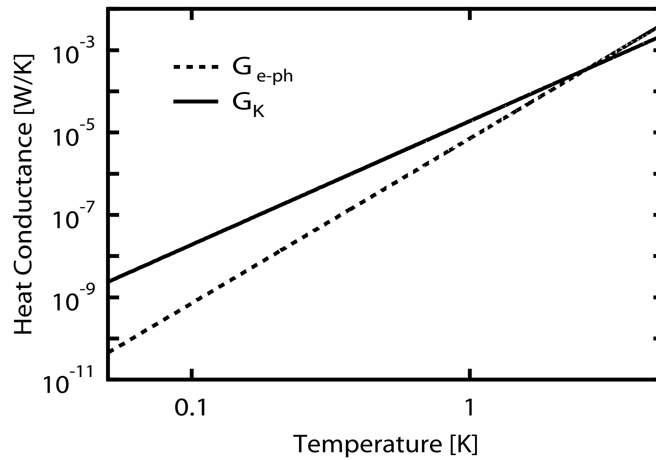

Figure 3.7: Comparison of heat conductances for different cooling mechanism.

conditions, the metal phonon temperature equals the substrate phonon temperature, while the electron temperature can be higher than that of the phonons, $T_e > T_p = T_s$.

3.8 Electronic Heat Capacity

The heat capacity of metals is usually taken to be the sum of the electronic and the lattice (or the phonon) contributions $C = C_e + C_p$. In normal state, the electronic heat capacity is proportional to temperature as

$$C_e = \gamma N_m T, \tag{3.35}$$

where γ is the Sommerfeld constant, and N_m is the number of moles of the electrons. The constant is estimated from the free electron model (Ashcroft & Mermin 1976) with the expression,

$$\gamma = \frac{\pi^2}{3} k_B^2 D(\varepsilon_F), \tag{3.36}$$

and is in relatively good agreement with the experimental data on bulk alkali metals and noble metals (Cu, Ag, Au) (Ashcroft & Mermin 1976). The phonon heat capacity for temperatures much lower then the Debye temperature[10], $T \ll \theta_D$, has a cubic temperature dependence according to Debye model

$$C_p \approx 234 N k_B \left(\frac{T}{\theta_D} \right)^3 \tag{3.37}$$

where N is the number of atoms. At temperature well above 1 K, due to the cubic dependence on temperature, the phonon heat capacity is much higher than that of the electrons. However, below 1 K, in the disorder regime, the electronic heat capacity dominates the total heat capacity.

In our metal thin film, the electrons of the metal are only thermally connected to their surroundings through election-phonon interaction. Thus, the electronic heat capacity can be obtained by

$$C_e = G_{e-ph} \tau_{e-ph}. \tag{3.38}$$

This provide an approach for measuring the electronic heat capacity at low temperatures in nano-scale structures.

Alternatively, the electronic heat capacity of metals can be approached directly from its definition

$$C_e = \left(\frac{\partial U}{\partial T} \right)_n, \tag{3.39}$$

[10] The Debye temperature of Au is 165 K. Thus, in the disorder regime, this condition holds for all temperatures.

where U is the total energy of the electron system, and n is the electron concentration of the metal. For a small temperature excursion ΔT, the definition can be approximately written as $C_e = \Delta U/\Delta T$, this is the basis of calorimetry.

3.9 Hot electron blackbody photon sources and hot electron bolometers

As discussed in Chapter 2, the Johnson noise of our thin film resistor can transmit one-dimensional blackbody radiation through the connected transmission line to a matched conductor, and the blackbody radiation temperature T_{bb} equals the resistor temperature T_R. At low temperatures $< 1\,K$, the electrons and phonons in the metal are decoupled, thus the Johnson noise or equally the blackbody radiation solely depends on the electron temperature T_e, i.e. $T_e = T_{bb}$. Since the blackbody radiation power, at given frequency band, only depends on its temperature, the performance of the source completely lies in how well one can control the electron temperature T_e.

At very low temperatures, the electron temperature T_e in the disordered metal thin film can be readily controlled by the amount of applied Joule power; in steady state, the electron temperature is derived from eqns.(3.5). Since the electron-phonon cooling power in this regime is extremely weak, the amount of power needed to significantly change the electron temperature is very low. To give an idea, at bath temperature $T_{bath} \sim 50$ mK, a Joule power of only ~ 1 nW can heat up electrons in a $\sim 2000\ \mu m^3$ Au film to 100 mK (see Fig.5.4 for our measured results). Therefore, the thin films are very sensitive photon sources.

Moreover, the steady state electron temperature stabilizes on a timescale $\sim \tau_{e-ph}$. The electron-phonon time τ_{e-ph} is fairly short, on the order of ns–μs. Hence, the thin

films photon sources also have fast time response.

Chapter 4

Dynamic Microwave noise thermometry

In order to study the low temperature electron-phonon interaction in disordered metal thin films, it is important to accurately measure the electron temperature T_e. It is also essential to precisely determine the electron temperature when the thin films are used as sub-millimeter photon sources in our on-chip sub-millimeter detector calibration scheme; it enables us to accurately measure the output photon power. In this chapter, we discuss a new technique for studying the electron-phonon interaction with the accurate and fast dynamic microwave noise thermometry, which enables us to measure both the steady state and the dynamic characteristics of the interaction in the same setup.

4.1 Review of techniques for measuring electron-phonon interaction

Despite the great importance of the electron-phonon interaction in disordered thin metal films, there are few experimental techniques available to probe the interaction at very low temperatures ($\sim$ 1K).

The electron-phonon interaction rate τ_{e-ph}^{-1} has been measured from the study of weak localization (Santhanam & Prober 1984, Gershenzon et al. 1990, Echternach et al. 2002, Friedrichowski & Dumpich 1998, Il'in et al. 1998, Hsu et al. 1999, Gershenson et al. 2001, Lin & Bird 2002), where the temperature and magnetic field dependence of weak localization (i.e. the magneto-resistance of the sample as a function of temperature) is used as the electron thermometer. This technique directly accesses the inelastic electron scattering processes that destroy the phase coherence of electron's wave functions. These processes include electron-electron scattering, spin-orbit scattering, electron-magnetic impurity scattering, electron-phonon scattering. Thus, the measured electron dephasing rate τ_{φ}^{-1} bears signatures of all possible inelastic scattering mechanisms. However, the electron-phonon rate τ_{e-ph}^{-1} is only directly measured at relatively high temperatures (a few Kelvin), where the electron-phonon interaction is the dominant inelastic scattering mechanism. At lower temperatures, the rate is extracted by subtracting other scattering effects (e.g. the electron-electron interaction) (Echternach et al. 1993). Also, the actual measured quantity is the electron dephasing time τ_{φ}, which does not always coincide with the electron inelastic scattering (or energy loss) time τ_i (Altshuler et al. 1982), the desired quantity to be measured. Finally, the technique is only suitable for measuring the electron-phonon interaction at steady states.

In 1985, Roukes et al. developed a new technique for directly measuring the electron-phonon interaction at low temperatures. In this work, a Joule power is applied to the device to heat up the electrons in the thin film (as we discussed in Chapter 3). The Johnson noise of the hot electrons are used as the electron thermometer, since the Rayleigh-Jeans limit of the Johnson noise generated by the hot electrons, $P_{RJ} = k_B T_e B$, has a simple linear dependence on the electron temperature

T_e. Thus is a direct measurement of the electron temperature T_e. This is usually called the *Johnson noise thermometry* (White et al. 1996). Although this concept has been established in the 1920's (Nyquist 1928), the thermometry technique is not widely used. The main obstacle is the difficulty of measuring the extremely low noise powers, especially at low temperatures. For example, a resistor at 1 K in a 100 KHz bandwidth generates a noise power $\sim 10^{-18}$ W. High gain amplifiers are needed to amplify the noise signal to measurable levels. But inevitably, they add more noise to the system and corrupt the already very small noise signal. The uncertainty of the temperature δT is given by Dicke (1946) as $\delta T/T_N = 1/\sqrt{B\tau}$ at a system noise temperature T_N, where τ is the measurement time, and B the bandwidth. Thus to measure the temperature with high accuracy, low system noise temperatures and/or large bandwidths and long integration times are desirable. To give an idea, for a 5 K system noise temperature, and 100 kHz bandwidth, a 250 s integration time is needed to measure the temperature with 1 mK accuracy. Therefore, in order to detect such small signals, ultra–low–noise dc superconducting quantum interference device (dc SQUID) amplifiers are used to measure the Johnson noise of the device (Roukes et al. 1985, Wellstood et al. 1994), and measure the electron temperature with a resolution better than 1 mK below 1 K. However, the setup is not fast enough to perform direct time domain measurements of the electron-phonon time ($\lesssim \mu s$), due to the inductive input coupling to the SQUID amplifier.

Alternatively, the electron temperature can be measured by using *superconductor-insulator-normal metal* SIN junctions attached to the normal metal film being measured (Nahum & Richards 1993, Schmidt, Yung & Cleland 2004, Taskinen et al. 2004). The small signal resistance $R_0 = dV/dI$ of the junction is a function of the electron temperature (Nahum & Richards 1993), i.e. $R_0(T_e) \propto e^{-\Delta/k_B T_e}$, where Δ is the en-

ergy gap of the superconductor. The resistance can be measured very accurately by using very small bias currents without significant self-heating. The measuring bandwidth of the SIN thermometer is often limited by the stray capacitances. Schmidt, Yung & Cleland (2004) have improved the bandwidth ($\sim$ 100 MHz) by using a rf LC tank circuit, and the resistance is measured from the reflected power of the tank circuit at its resonance frequency $f = 1/2\pi\sqrt{LC}$. The setup has been used to measure the electron-phonon interaction time $\tau_{e-ph} \sim 1.6\mu s$ of Au films from electron cooling/heating dynamics in the time domain. However, the sample being measured is a complicated combination of a few materials — Au, NiCr, and Cu, which are introduced from the electron heater and the SIN thermometer. It is hard to define the material actually being measured. Moreover, the materials that can be characterized by this technique are limited by the require SIN junction. Also, the superconductor in the thermometer sets a upper temperature limit of the measurement, i.e. the critical temperature of the Al, $T_c \sim 1.2$ K.

In this thesis work, we develop a new technique — the *dynamic microwave Johnson noise thermometry* for measuring the hot electron temperature T_e, by incorporating the Johnson noise thermometry with our microwave setup. It is a simple apparatus, without the complication of using SQUID amplifiers and SIN junction thermometers, yet still accurate and fast enough to study both the steady state and dynamics of the electron-phonon interaction. The technique uses the Johnson noise of the hot electrons as the electron thermometer, with a conventional low noise broad band cold HEMT amplifier. Fig.4.1 gives a simplified block diagram for the setup. The voltage bias source applies Joule power through the dc path of the bias-tee to the thin metal film, and causes generation of hot electrons. The Johnson noise of the film is in turn coupled to the cold rf amplifier via the ac path of the bias-tee. The working

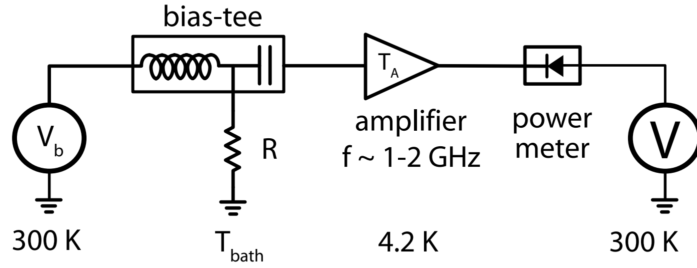

Figure 4.1: Schematics of dynamic microwave Johnson noise thermometry.

frequency band of the amplifier is about 1-2 GHz, which is in the Rayleigh-Jean limit of the hot electrons Johnson noise even at the lowest measurement temperature ~ 50 mK. The amplified noise power is then detected by the power detector, whose output is measured by a voltmeter. The setup has a wide bandwidth ~ 500 MHz, which gives a highly accurate temperature measurement ~ 1 mK in a short 1 s integration time, with the low noise cold amplifier $T_A \sim 5$ K. The microwave setup also gives the system a very fast time response, ~ 80 ns. Thus, it enables us to measure both the steady state and fast dynamics ($\tau_{e-ph} \sim 80$ ns – 20 μs) of the low temperature electron-phonon interaction within the same setup.

In the remainder of the chapter, we give a detailed description of the experimental setup of the dynamic microwave noise thermometry for measuring the electron-phonon interaction in thin metal films, both the steady state characteristics and cooling/heating dynamics. The calibration of the electron temperature is given in the end.

4.2 Microwave noise thermometry setup

4.2.1 Microwave setup

The detailed schematic of the microwave noise setup is shown in Fig.4.2.

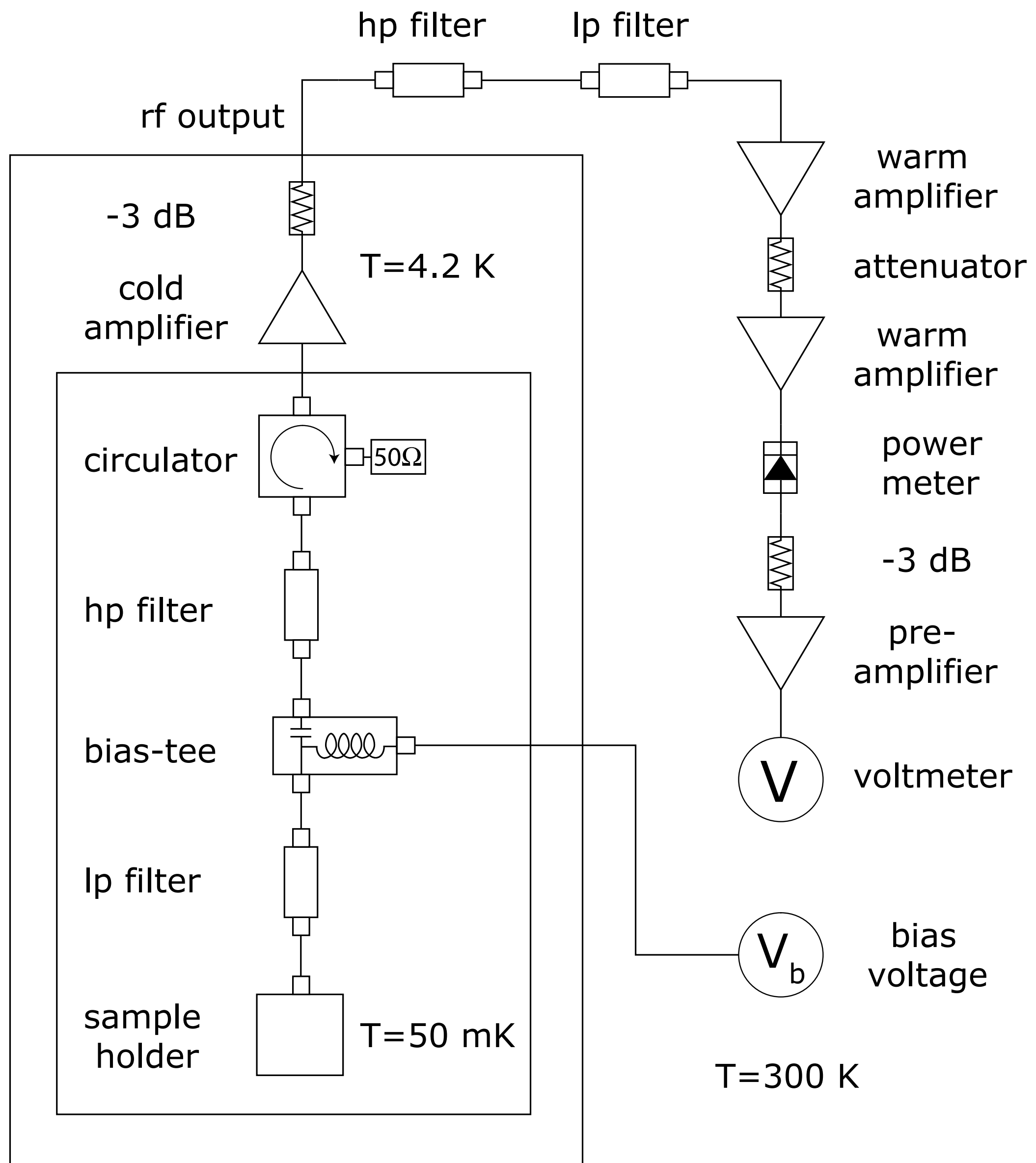

Figure 4.2: Block diagram of microwave noise thermometry setup.

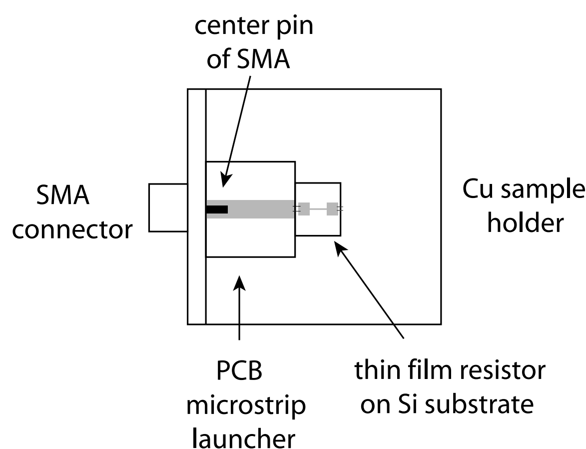

Figure 4.3: The sample holder and microstrip launcher.

Chip mount

The device is mounted on a microstrip launcher sitting in a Cu sample holder (Fig.4.3). The launcher is patterned on a piece of double-sided Cu clad Arlon printed circuit board (PCB). The back ground plane of the board is low temperature soldered onto the sample holder. The microstrip has a characteristic impedance of $50\,\Omega$ to match to the microwave setup, and the line extends the full length of the circuit board. An SMA connector launches microwave signals to the microstrip launcher, with its center pin soldered onto one end of the microstrip. The other end of the microstrip is wire bonded to the thin film resistor, which is fabricated on a Si substrate. The substrate is held closely to the edge of the launcher board, and vacuum grease is used to attach the chip to the sample holder to provide better thermal contact. The other end of the resistor is wire bonded directly to the sample holder, which is the electrical ground. The sample holder is thermally anchored to the mixing chamber of the Oxford Kelvinox dilution refrigerator.

Cold stage rf filtering

In principle, the sample holder is connected to a bias tee, and the microwave noise of the sample is capacitively coupled to a cold amplifier through the ac path of the bias tee. However, the device is extremely sensitive to noises (e.g. thermal radiation from the cold amplifier, rf leakage, thermal radiation of cables from higher temperature stages[1]), they can heat up the electrons in the metal thin film in the absence of bias voltage. So, we take special care to eliminate the excessive noise that could heat up the device, by filtering the rf line between the amplifier and the sample.

The dominant source of radiation noise is the cold amplifier (NRAO L-band amplifier, frequency band 1-2 GHz) that is sitting at 4.2 K. One can model this as two conductors of different temperatures connected by a lossless transmission line (Fig.4.4). At zero bias, the electrons in the thin film resistor are at the bath temper-

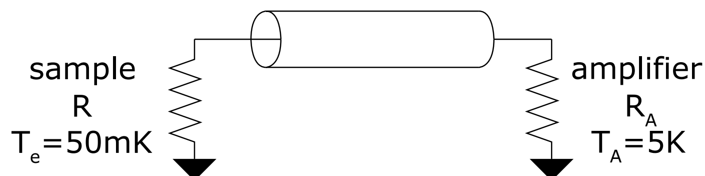

Figure 4.4: Electrons excessive heating by the thermal radiation of the amplifier.

ature $T_e = T_{bath}$. The amplifier is represented as a conductance with the amplifier input resistance R_A, at the amplifier noise temperature ~ 5 K. The thermal radiation power emitted by the amplifier and absorbed by the electron gas in the resistor thin film (Schmidt, Schoelkopf & Cleland 2004*b*) is

$$P = \frac{4RR_A}{2\pi(R+R_A)^2}\int_0^\infty \hbar\omega\left(\frac{1}{e^{\hbar\omega/k_BT_A}-1} - \frac{1}{e^{\hbar\omega/k_BT_e}-1}\right)d\omega. \tag{4.1}$$

If our device has $R = R_A$ and the electron temperature is well below the amplifier noise temperature, $T_e \ll T_A$, the above equation recovers the expression in eqn.(2.14).

[1]See Chapter 2.

At the base temperature 50 mK, the electron-phonon heat conductance G_{e-ph} is extremely small, $\sim 10^{-11}$ W/K. Thus, this excessive radiation noise power in the 0 - 40 GHz band[2] can heat up the electron gas by $\Delta T_e = P/G_{e-ph} \sim 100$ mK.

To block the radiation, we install a PAMTECH cryogenic circulator with frequency band between 1.25 to 1.75 GHz right before the amplifier at the mixing chamber (i.e. at the bath temperature T_{bath}). The circulator is a non-reciprocal three-port device, with each port coupled to the next port in a cyclic order. For the sake of discussion, we denote the port that is connected to the amplifier as port 1. The power coming through this port is mainly coupled to port 2, which is terminated with a 50 Ω termination. Port 2 is coupled to port 3, which is fed by the microwave noise signal from the device, and the signal flows in turn to port 1 and arrives at the amplifier. With the circulator on the rf line, the excessive radiation power from the amplifier is largely diverted to the 50 Ω termination that is thermally anchored at the mixing chamber, and the power is attenuated by at least 20 dB when it arrives at port 3. In addition, the device also receives radiation noise from a 50 Ω conductor at the bath temperature. However, as it is at the same temperature with the device, the radiation power is negligible.

To further attenuate the radiation noise coming out of the circulator, we put a pair of filters between the circulator and the device. A mini-circuits VHP1200 1.2 GHz high pass filter follows the circulator to block the excessive noise below 1.2 GHz. The filter is connected to the Wiltron-Anritsu K250 bias-tee, with frequency band 0.1-40 GHz. Between the bias-tee and the device there is a mini-circuits VLF1700 1.7 GHz low pass filter, that serves the same purpose as the high pass filter; it attenuates signals higher than 1.7 GHz from the above mentioned components. Note that, the

[2]This is the bandwidth of the bias-tee

low pass filter is placed after the bias-tee while the high pass filter is placed before the bias-tee. This arrangement helps to eliminate the noise coming from the dc bias source, but still allowing the low frequency bias signal to pass through. The VLF and VHF filters are chosen over the SLP and SHP filters because of their small size and the limited space in the refrigerator.

With the filtering scheme described above, the excessive noise which radiates down to device is minimized. Meanwhile, the Johnson noise power generated by the hot electrons in the device in the frequency band of the rf line ($\sim$ 1.2-1.7 GHz) is coupled to the cold amplifier without or with little attenuation. A -3 dB is connected at the output of the amplifier to minimize the standing waves in the line.

Room temperature RF setup

The signal coming from the refrigerator rf output is then coupled to the room temperature components. The signal first passes through a 1.2 - 1.7 GHz bandpass filter (it is made of a VHF-1200 1.2 high pass filter and a VLF-1700 low pass filter). The pass band of the filter matches that of the circulator in order to maximize the ratio of signal from the device to the noise signal from the amplifiers. The filtered signal is then amplified by two MITEQ (AFD3-010020-13-sd) 1-2 GHz amplifiers, both having gains $\gtrsim$ 35 dB. An attenuator is inserted between the two amplifiers to prevent overloading the second amplifier by the output from the first amplification stage. The amplified signal is in turn fed to a microwave pulse/CW power detector (Herotek DTM180AA, 1-18 GHz), which is followed by a -3 dB attenuator as a 50 Ω load. The detector is essentially a square law detector, whose output voltage is proportional its input power. With a 50 Ω load, the detector has a sensitivity of 90 mW/mW, with a very fast rising time of 1 ns, which is suitable for pulse detection. Finally, the signal

from the power detector is further amplified by a pre-amplifier and measured by a digital voltmeter.

4.2.2 DC bias line

The hot electrons in the thin film resistor are generated by applying Joule power to the device. The bias voltage V_b source is coupled to the device through the DC port of the Wiltron-Anritsu K250 bias-tee.

DC bias line filtering

There is a need to minimize the excessive rf noise coming down from the DC bias line. The bias-tee itself is an effective rf blocker from ~30 MHz to ~30GHz. To further attenuate the rf leakage noise, the DC line is heavily filtered by three Cu powder filters[3] before it arrives at the bias-tee. The filters are thermally anchored to the 1 K pot, the still (~ 800 mK), and the mixing chamber of the refrigerator respectively. Each of the filters attenuates the rf signal above ~ 300 MHz by approximately 20 dB. For the rf noises below 30 MHz, a mini-circuits BLP1.9 1.9 MHz low pass filter is placed at the DC input of the fridge. However, for performing dynamics measurement, where fast pulses are measured, the BLP1.9 is used since it limits the resolution of the pulse rise time.

AC bias

The DC path of the bias-tee allows signals with frequency below 30 MHz to pass through. Thus, the device can be biased both with a DC source and an AC source below 30 MHz. This is used in our electron-phonon dynamics measurement, where

[3]These are home made filters. The detailed process for making the filters is given in Siddiqi (2002).

square waves of frequency ∼2 KHz – 100 KHz are used to pulse the device. However, the bias-tee limits the rise time of the square wave to ∼ 50 ns, thus limiting the time resolution of the electron-phonon interaction (τ_{e-ph}).

4.3 Electron temperature T_e calibration

In our measurement, we use the low frequency (Rayleigh-Jeans) limit Johnson noise power generated by the hot electrons $P_{JN}(T_e) \sim T_e B$ as the electron thermometer. The actual noise power signal, however, contains Johnson noise from both the hot electrons and the system, i.e. $P_{JN} \propto (T_e + T_N)B$, where the T_N is the system noise temperature that is dominated by the cold amplifier, and B is the bandwidth, ∼500 MHz. The noise power as the input of the square law power meter is converted into voltage at the output $\propto P_{JN}$. The final quantity measured at the voltmeter is expressed as

$$V_d = G(T_e + T_N), \tag{4.2}$$

where G is the effective gain of the rf chain, which includes the gain of the power amplifiers, the sensitivity of the power meter, the gain of the voltage amplifier and other losses from the cables and connections. In order to extract the electron temperature T_e, we need to know G and T_N.

The electron temperature T_e is calibrated by using its own Johnson noise as the calibration standard. When the device is under zero bias, the electrons are at the bath temperature (See Chapter 3), $T_e = T_{bath}$. The bath temperature (the temperature of the sample holder or the mixing chamber of the refrigerator) is well defined by a calibrated RuO resistor attached to the Cu sample holder, which is thermally anchored at the mixing chamber. Thus, the measured voltage output is $V_d = G(T_{bath} + T_N)$. During the calibration, we sweep the mixing chamber temperature from the base

temperature ($\sim$ 50 mK) to near the still temperature $\sim$ 800 mK and back down, in about 30 min. The G and T_N are extracted from the straight line fitted to the V_d vs. T_{bath} curve; the slope gives the effective gain G, and the y intercept gives the system noise temperature T_N.

Fig.4.5(a) shows a typical pair of heating and cooling calibration curves. The curves are taken at zero voltage bias[4]. The curves show a good linear dependence above $\sim$ 80 mK; the G and T_N obtained from the fitting line are 0.6 V/K and 8 K respectively. The heating curve plateaus below $\sim$ 80 mK, indicating the electrons in the film are at a temperature above that of the bath, probably due to imperfect thermal coupling between the sample and the bath. Thus, there is a delay between the heating of the mixing chamber and the electron gas in the device after the heater is turned on. Another possible cause is that the un-filtered excessive noise power heats up the electrons, and the Johnson noise electron temperature thermometer is not sensitive enough below $\sim$ 80 mK. In order to check the effect of the excessive noise, we bias the device with a small voltage so the electrons are heated slightly above the bath (to $\sim$ 120 mK) at the base temperature, and perform the same bath temperature sweep, as shown in Fig.4.5(b). The non-zero bias curves saturate at low temperatures, and the electrons cannot be cooled to the base temperature of the cryostat. However, the drift of the amplifier gain and noise temperature during the temperature sweep could also give similar effects. For instance, the non-zero bias calibration curves in Fig.4.5(b) have "hysteresis" between the heating and cooling sweeps; due to the drift of the amplifier, the electron temperature during the heating sweep appears to be higher than the cooling sweep. However, the amplifier drift does not cause the electron to appear "cooler', as both the non-zero bias curves give higher

[4]The device is under voltage bias. To ensure zero bias, the device is terminated by a 1 MΩ or higher resistance resistor.

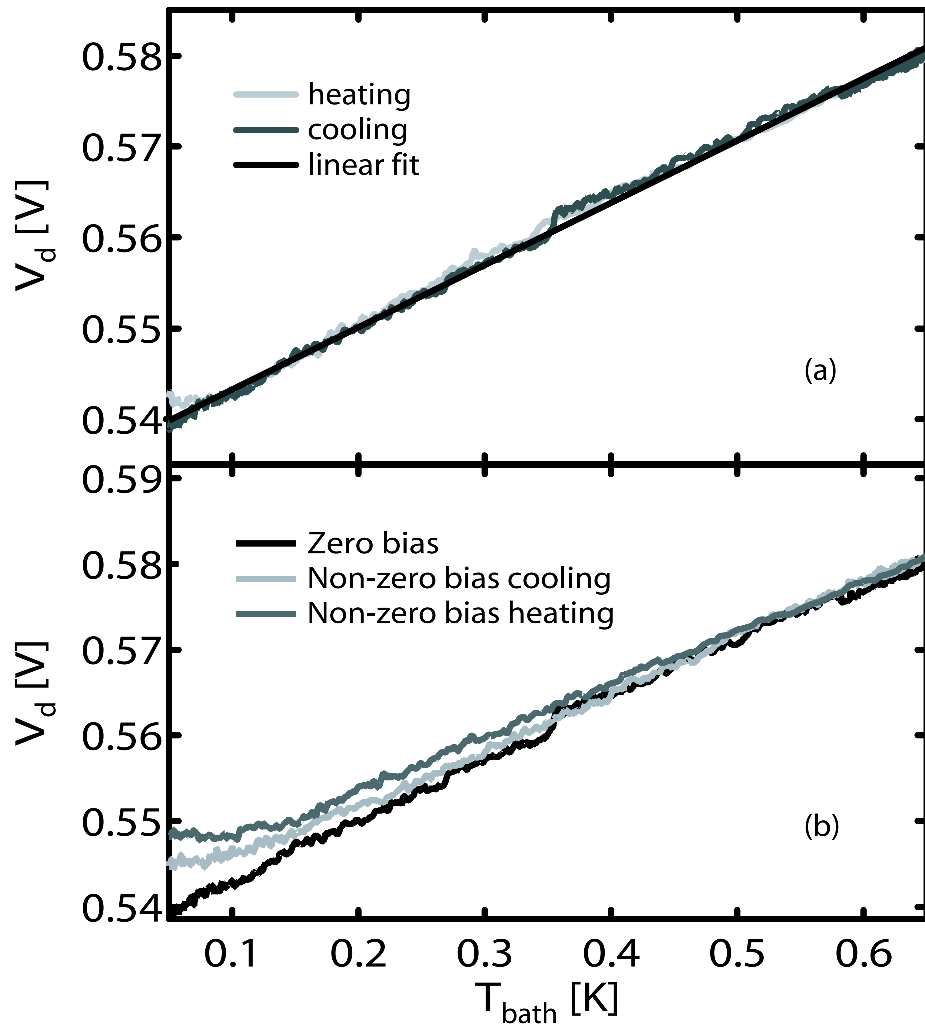

Figure 4.5: Electron temperature T_e calibration.
(a) Johnson noise calibration of T_e by sweeping the bath temperature T_{bath}. (b) Check for excessive noise by comparing zero and non-zero bias temperature sweeps, and the effects of possible amplifier drift.

electron temperature than the zero bias curve. Therefore, regardless of the amplifier drift, we are able to distinguish excessive heating with ~40 mK precision.

4.4 Electron-phonon interaction measurement setups

In our electron-phonon interaction study, we perform steady state measurements for T_e vs. P_{Joule} characteristics and the electron-phonon heat conductance G_{e-ph}, and dynamic measurements for the electron-phonon interaction time τ_{e-ph} and the electronic heat capacity C_e. The setups for these measurements are based on the microwave noise thermometry setup presented in the previous section, but they differ slightly in the bias and data acquisition schemes.

4.4.1 Steady state measurement setup

For the T_e vs. P_{Joule} characteristics, we sweep the DC voltage source (Yokogawa 7651 DC voltage source) applied to the device, and measure the output of the power meter by a digital voltmeter (Keithley digital multi-meter or HP 34401 digital multi-meter). The electron-phonon heat conductance G_{e-ph} can be extracted from the T_e vs. P_{Joule} curves (see Chapter 5).

The electron-phonon heat conductance is also directly measured. Note that, for a small temperature excursion δT_e, the second derivative of the electron temperature T_e with respect to the bias voltage V_b is proportional to the inverse of the electron-phonon heat conductance G_{e-ph}, i.e. $\partial^2 T_e/\partial V_b^2 \propto 1/G_{e-ph}$. Thus, the G_{e-ph} can be measured by using a lock-in amplifier, as shown in the setup scheme below (Fig.4.6). The device is biased at zero voltage, and a small AC excitation ($f \sim 100$ Hz) is applied to the

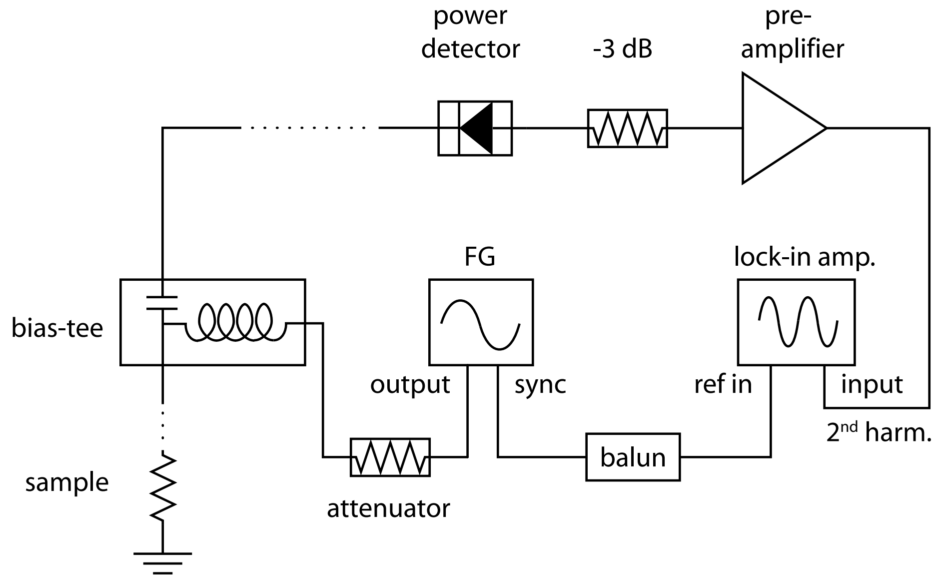

Figure 4.6: Setup for G_{e-ph} measurement.
The dotted lines represent the rf components that are the same as in Fig. 4.2 but are omitted in the plot.

device by a function generator. An attenuator is used to attenuate the output of the function generator to the desired voltage level. The sync signal provides the external reference for the lock-in amplifier (Stanford Research System SR830) through a balun, which breaks the ground loop of the setup. The output of the power meter is then amplified by the voltage pre-amplifier (SRS SR560) and fed to the input of the lock-in amplifier. The lock-in amplifier measures the second harmonic of the signal (i.e. at $2f$), which gives the second derivative of T_e with respect to the small AC excitation.

4.4.2 Dynamics measurement setup

The direct time domain measurement of the electron-phonon dynamics requires fast rising heat pulses and fast data acquisition process that can measure the fast heating and cooling time of the electrons. The data acquisition scheme should also be able to

efficiently average the data to improve the signal/noise ratio in a reasonable period of time. In this measurement, a function/pulse generator (Agilent) applies square wave voltages through the DC port of the bias-tee to the device. The electrons in the

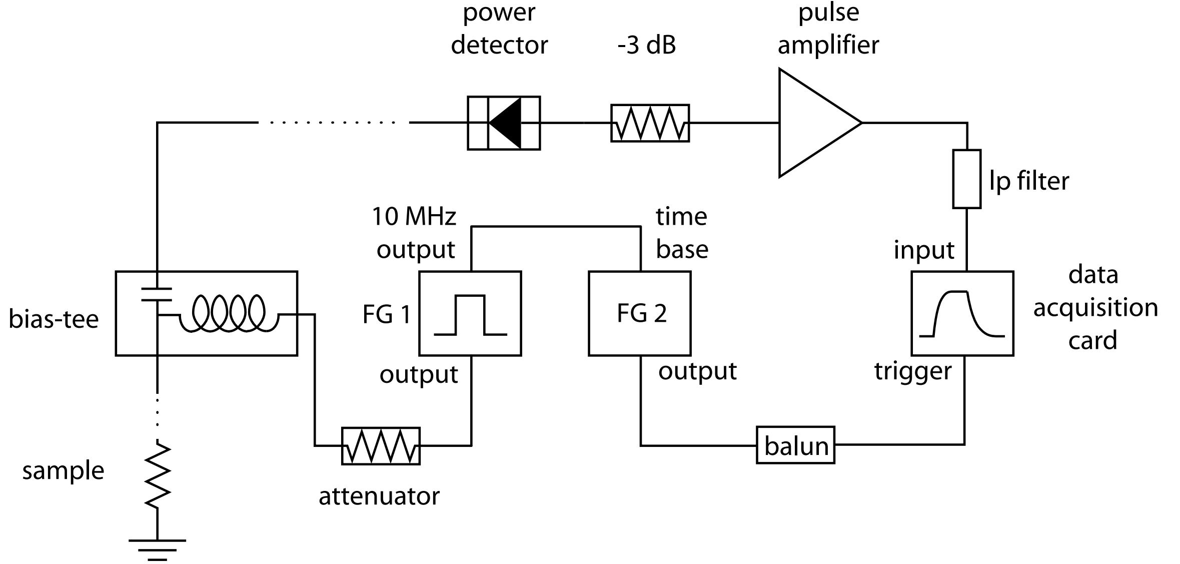

Figure 4.7: Electron-phonon dynamics measurement setup.

thin film heat and cool according to the rise and fall of the square wave, and so does the Johnson noise generated by the hot electrons. The Johnson noise signal from the output of the power detector is amplified by a chain of pulse amplifiers (Analog Devices AD8009) instead of the SR560 voltage pre-amplifier. The pulse amplifiers have less than 1 ns rise time. To resolve the fast electron-phonon time, the final Johnson noise output is recorded in the time domain by a fast digitizer (Acqiris DP110) card. This 8-bit card has a fast sampling rate (1GS/s), wide bandwidth (250 MHz) and a large acquisition memory (2 Mpoints). It is used as a fast digital oscilloscope that can follow fast pulse rise/fall (1 ns), and average the data to provide better signal/noise ratio. To avoid aliasing during digitization, a low pass filter is inserted right before the card input[5]. For a given sampling time interval Δt, the cutoff

[5]Please refer to Nyquist's sampling theorem (Shannon 1948).

frequency of the filter is chosen to be the Nyquist frequency $f = 1/2\Delta t$, according to the Nyquist's sampling theorem. The trigger of the digitizer is provided by a second function generator whose timebase is tied to the Agilent function generator. The function generator also serves as a phase shifter. To break the ground loop in the setup, a balun (Mini-Circuit FTB1-6) is placed right before the trigger input.

Chapter 5

Electron-phonon interaction in disordered thin Au films

In this chapter, we discuss our measurements of the electron-phonon interaction in disordered thin Au films. Both the steady state and dynamic characteristics of the interaction are explored in two groups of devices: long diffusive wires with normal metal conducting leads and short wires in SNS structures.

In the first section, we give a list of the devices that are studied in this work. Basic physical and electrical properties are provided, together with a short description of the device fabrication.

The steady state measurements of the electron-phonon interaction are discussed in the second section. In these measurements, the applied heating power varies much slower than the electron-phonon time, so that the electrons can always achieve a steady state temperature. Both the $T_e(P_{Joule})$ characteristics and the electron-phonon heat conductance are measured under this condition. They are both qualitatively consistent with the theoretical predictions.

In the third and fourth sections, we present our direct time domain measurements of the electron-phonon dynamics. In the measurements, the electrons are heated by fast heat pulses; the rise/fall time of the pulse is much shorter than τ_{e-ph}; therefore

the electron temperature cannot follow the the change of the pulse. By directly measuring the time response of the electron temperature, we are able to extract both the electron-phonon interaction time and the electronic heat capacity. The time quantitatively agrees with the theory, however, the heat capacity is 10–50 times larger than the book value (Ashcroft & Mermin 1976, Kittel 1995). At the end of the fourth section, we give possible explanations for such unusual phenomena.

In the fifth section, we discuss the prospect of using the disordered metal films as phonon cooled hot electron bolometers (HEBs). The sensitivity of the HEB is estimated based on our measured G_{e-ph}, τ_{e-ph} and C_e. We suggest that the ideal sensitivity estimation based on the book value might be overly optimistic. In order to really understand the performance of the HEB, one should carefully measure the actual C_e of the absorber film.

In the last section, we give a short summary of our measurement results.

5.1 Au thin film devices

The devices we study are disordered thin Au films, with thickness d on the order of few hundred Å. Thus the electron mean free path ℓ is dominated by the film thickness, and the films are always in the disordered regime. Moreover, since the thickness of the films is smaller then the thermal phonon wave length $\lambda_T \sim hu/k_B T_p$ ($\sim$ 200 nm at 50 mK) in the metal, and the Kapitza heat conductance at the Au-substrate interface is much larger than electron-phonon heat conductance, the phonons in both the metal and the substrate can be treated as one phonon system, and with a well-defined temperature $T_p = T_{bath}$. The electrons in the metal film are thus interacting with 3D phonons.

The hot electrons in the film are cooled by out-diffusion and they also interact with the phonons in the metal film. The device structures that are suitable for studying the electron-phonon interaction should have the electron-phonon interaction as the dominant cooling mechanism for the hot electrons (see Chapter 3). One class of devices that satisfy such requirement are long diffusive Au thin film wires. If the length of the wire L is much longer than the electron-phonon length, i.e. $L > \pi L_{e-ph} = \pi\sqrt{D\tau_{e-ph}}$, the electrons are predominantly cooled by interacting with phonons (Burke 1997); only those electrons which are very close to the conducting lead (within $\sim L_{e-ph}$) are cooled by diffusing into the leads. Thus, the electrons have a uniform temperature T_e along the wire except for a very short ($\sim L_{e-ph}$) portion close to each end. However, due to the device length constraint set by the electron-phonon length L_{e-ph}, and the requirement of device resistance from the microwave setup, (the device should have resistance close to 50 Ω), the size of the device cannot be very small.

Alternatively, the electron out-diffusion can be blocked by superconductor leads, due to the Andreev reflection of the electrons at the superconductor-normal metal interface. In this case, as long as the wire length is larger than the electron-electron length, $L > L_{e-e}$, the electrons in the film have a uniformly defined temperature T_e. This class of devices are referred as SNS structures in this thesis. They allow us to measure the electron-phonon interaction in much smaller devices; the lower limit of the device length is set by the electron-electron length[1] L_{e-e}, which is 10-1000 times shorter than the electron-phonon length L_{e-ph} below 1 K. For fixed sheet resistance and thickness of the film, in order to maintain the 50 Ω resistance of the sample, the

[1]Please refer to Fig.3.2 for the comparison of the electron-electron and the electron-phonon interaction rates. The characteristic length is proportional to the inverse of the corresponding characteristic rate.

aspect ratio of the sample should be fixed. Hence, the SNS structures can have thin films that are 10^2-10^6 times smaller than the long diffusive wires in volume. Thus the SNS structures are desirable for studying the electron-phonon interaction in nano-scale films, and it is also desirable for the application of an ultra-sensitive photon sources, as the performance improves as the volume decreases (this will be discussed in the end of the chapter).

(a) Long diffusive Au wire

Device	L $^\flat$ (μm)	W (μm)	d (Å)	V (μm^3)	R$_\square$ (Ω)	ℓ (Å) †	D (cm^2/s)‡
Diff−1	40	2	400	3.2	2.5	84	39
Diff−2	1000	30	200	600	1.4	301	139

(b) Nb-Au-Nb SNS structures $^\sharp$

Device	L (μm)	W (μm)	d (Å)	V (μm^3)	R$_\square$ (Ω)	ℓ (Å)	D (cm^2/s)
SNS−1	15	3	200 §	0.9	7.1	59	23
SNS−2	10	0.5	120	0.06	3.8	184	85

Table 5.1: List of devices presented in the thesis.
(a) Long diffusive Au thin film wires, with Au conduction leads. (b) Au thin film wires in Nb-Au-Nb SNS structures. $^\flat$ L, W, d, and V are the length, width, thickness and volume of the Au wire respectively.
† ℓ is the electron mean free path.
‡ D is the 3D diffusion constant, D=$v_F^2\tau/3$, v_F and τ being the Fermi velocity the electron elastic mean free time.
$^\sharp$ The thickness of the Nb leads is 1000 Å.
§ The thin film resistor is made of $Au_{60}Pd_{40}$, and no Ti adhesion layer is used.

The Au long diffusive wires are patterned either by single layer electron beam lithography or photolithography on Si wafers, and the films are deposited in electron beam or thermal evaporator. A thin ($\sim$ 2-4 nm) Ti adhesion layer is deposited before the Au deposition. Fig.5.1(a) is an optical microscope picture of a long Au diffusive wire. The SNS devices require an extra layer of lithography and deposition for the Nb leads that are aligned to the alignment marks deposited with the Au layer, and

the films are deposited by using DC sputtering. To ensure good transparency at the superconductor-normal metal interface, the Au film is cleaned by ion milling before the sputtering. An optical microscope picture of the SNS structure is given in Fig.5.1(b).

A summary of the devices that are presented in this thesis work is given in Table 5.1. All the devices, expcept device Diff−2, are deposited on oxidized single crystal Si wafer, the thickness of the oxide is in the range of 3000 Å∼5000 Å. Device Diff−2 is directly deposited on a bare Si wafer.

5.2 Steady state characteristics

In this section, the measured $T_e(P_{Joule})$ characteristics and the electron-phonon heat conductance G_{e-ph} are discussed. They are both measured under steady state conditions; when the electrons in the Au thin films are heated up by Joule power that varies much slower than the electron-phonon interaction time τ_{e-ph}, the electron gas can reach a steady state with a well-defined temperature T_e, such that the heat flowing from the electrons to the cooler phonons, equals to the input Joule power,

$$P_{e-ph} = P_{Joule} = \frac{V_b^2}{R} = \Sigma V \left(T_e^{p+2} - T_p^{p+2} \right). \tag{5.1}$$

5.2.1 DC heating

First let us consider the system's response to DC heating. At steady state, the electron temperature T_e is determined by the bias voltage V_b or the Joule power P_{Joule} with the following relations derived from eqn.(5.1),

$$T_e = \left(\frac{V_b^2}{R\Sigma V} + T_p^{p+2} \right)^{1/(p+2)}, \tag{5.2a}$$

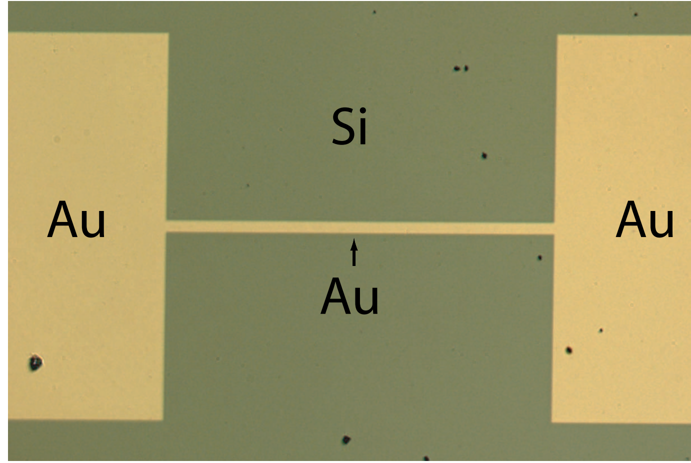

(a) OM picture for device Diff−2, 1 mm×30μm Au wire.

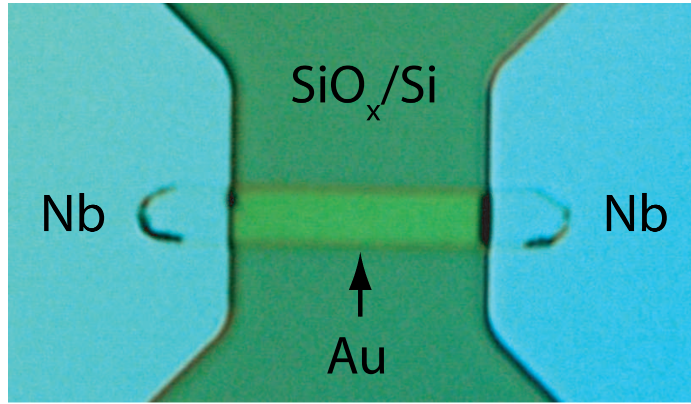

(b) OM picture for device SNS−1, 15μm × 3μm Au wire.

Figure 5.1: Optical microscope pictures for the devices.
(a) Long diffusive Au wire, device Diff−2. (b) Nb-Au-Nb SNS structure, device SNS−1.

or in terms of the input Joule power

$$T_e = \left(\frac{P_{Joule}}{\Sigma V} + T_p^{p+2} \right)^{1/(p+2)} . \tag{5.2b}$$

Fig.5.2(a) gives a typical T_e vs. P_{Joule} curve for DC heating, from device SNS-2, at the bath temperature 260 mK. The dots are the data, and the solid line is derived from eqn.(5.2b) with $T_p = 0.26$ K, where the adjustable parameters are $\Sigma V = 5.0 \times 10^{-10}$ W/K$^{4.2}$ and $p = 2.2$. It shows that at small bias voltage/Joule power, the bias does not provide enough energy to drive the electrons to temperatures significantly above

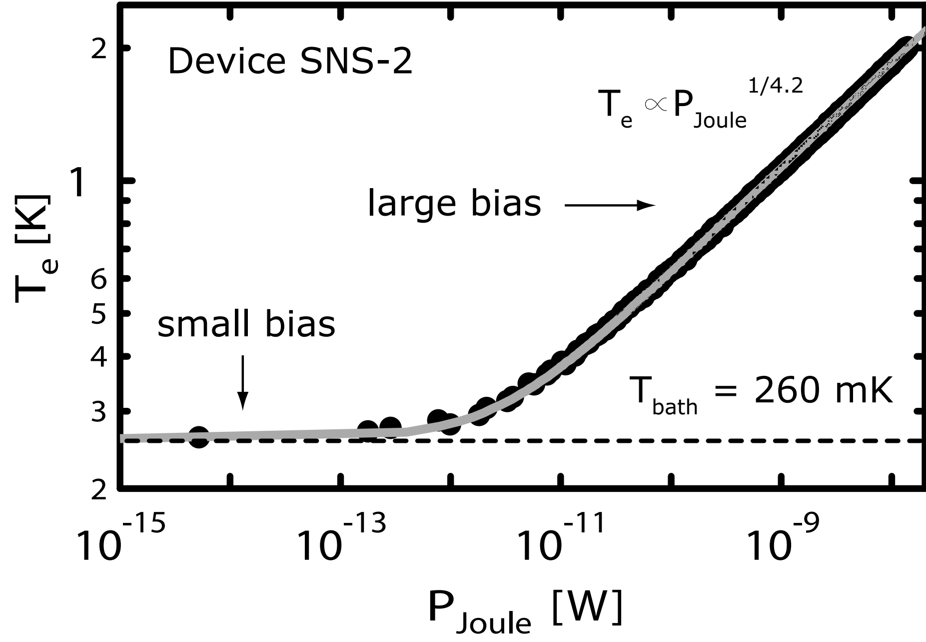

(a) T_e vs. P_{Joule} at $T_{bath} = 260$ mK.

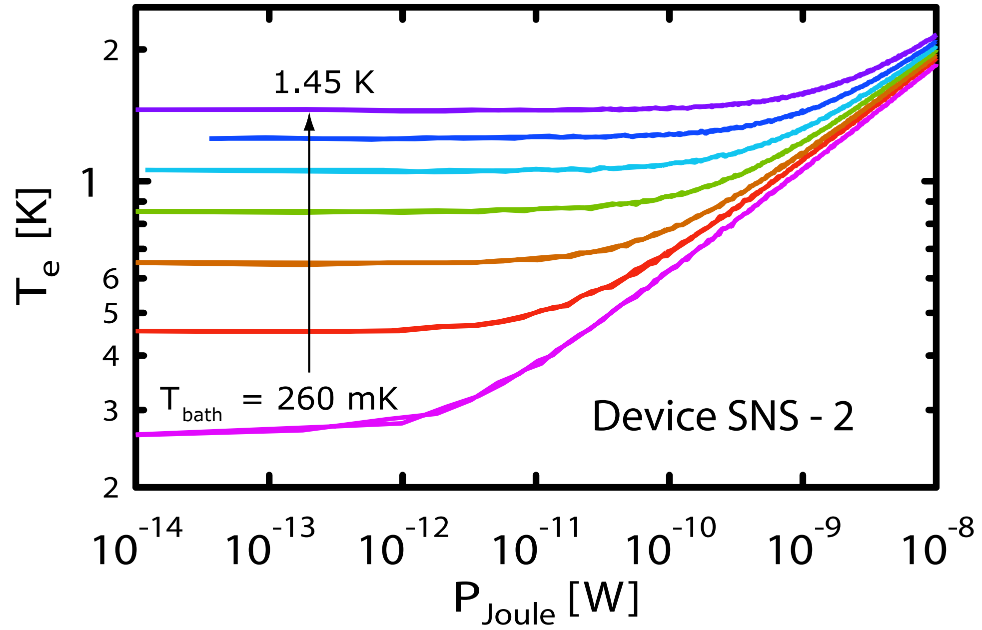

(b) T_e vs. P_{Joule} for bath temperature sweep.

Figure 5.2: T_e vs. P_{Joule} for Au wire in the SNS structure, device SNS-2. (a) At bath temperature $T_{bath} = 260$ mK. (b) At different bath temperatures T_{bath}'s, from 260 mK to 1.45 K.

T_p, thus the electron temperature $T_e \approx T_p = T_{bath}$. This is consistent with eqn.(5.2(b)) as P_{Joule} approaches zero. While for larger bias voltage/Joule power, the electrons and the phonons are decoupled, and the electron temperature only depends on the input[2] as expected from eqn.(5.2) at large bias

$$T_e \propto P_{Joule}^{1/(p+2)}. \tag{5.3}$$

We also measure the T_e vs. P_{Joule} curves at different bath temperatures (Fig.5.2(b)), from 260 mK to 1.45 K. This gives a clearer picture of the relation. For small bias, the electron temperature T_e of each curve approaches to its phonon temperature T_p, or equally the bath temperature T_{bath} of the refrigerator, while for high bias limit, the electron temperatures of all curves approach the same temperature, following approximately the same power law relation, $T_e \propto P_{Joule}^{1/(p+2)}$, regardless of the difference in their phonon temperatures.

The T_e vs. P_{Joule} curves for device Diff-1 and SNS-1 for a single bath temperature are given in Fig.5.3. On the plots, the dots represent the data, and the solid lines approximate the data with the relation calculated from eqn.(5.2(b)), Σ and p being the adjustable parameters. Table.5.2 summarizes these parameters for these devices. The electron temperatures of device Diff-1, SNS-1, and SNS-2 show similar power

Device	p	Σ
Diff-1	1.8	5.0×10^9 W/m^3·K$^{3.8}$
SNS-1	2.2	7.0×10^9 W/m^3·K$^{4.2}$
SNS-2	2.2	8.0×10^9 W/m^3·K$^{4.2}$

Table 5.2: The parameters for $T_e(P_{Joule})$ characteristics calculated from eqn.(5.2(b)).

law dependence on the input Joule power at large heat power limit, i.e. $p \approx 2$. This

[2]There is a crossover bias voltage, above which the electron temperature is solely determined by the bias voltage (Roukes et al. 1985, Roukes 1985).

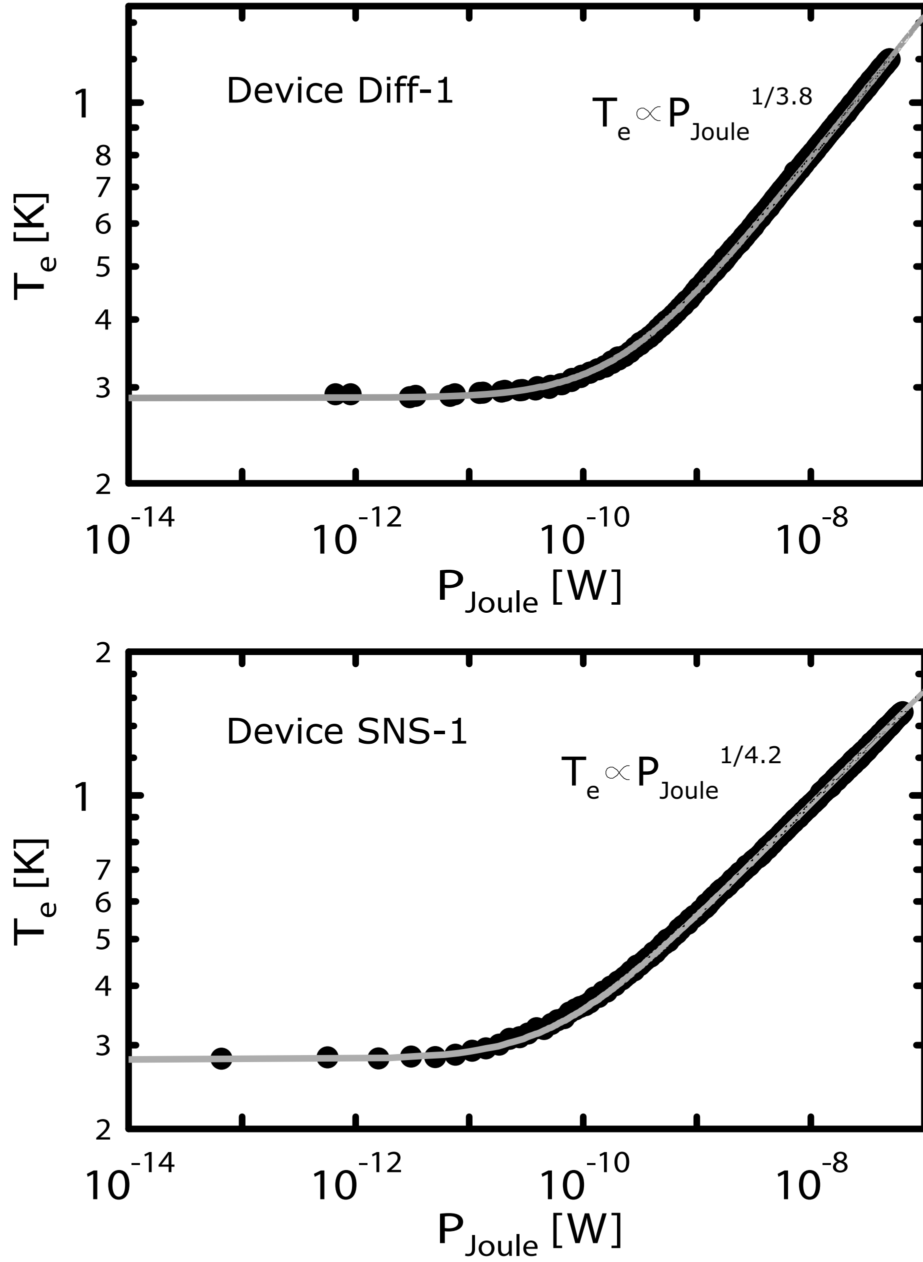

Figure 5.3: The T_e vs. P_{Joule} for device Diff-1 and SNS-1.
The bath temperatures for device Diff-1 and SNS-1 are 290 mK and 280 mK respectively. The data are given by the dots, and the calculated T_e's as functions of the input P_{Joule} are plotted as the solid lines.

is consistent with the theoretical prediction for the electron-phonon interaction for disordered metal films (see Chapter 3). The extracted Σ values are in reasonable agreement among the three devices within a factor of 2, which means that G_{e-ph} scale with the film volume as expected from eqn.(3.5(d)). We notice, however, that the $T_e(P_{Joule})$ characteristics of device Diff-2 deviates from $p \approx 2$, it has $p \approx 3$ instead. The plot in Fig.5.4 is the T_e vs. P_{Joule} curve at the bath temperature $T_{bath} \approx 50mK$. The dots are experimental data, the solid line is calculated from eqn.(5.2(b)), with

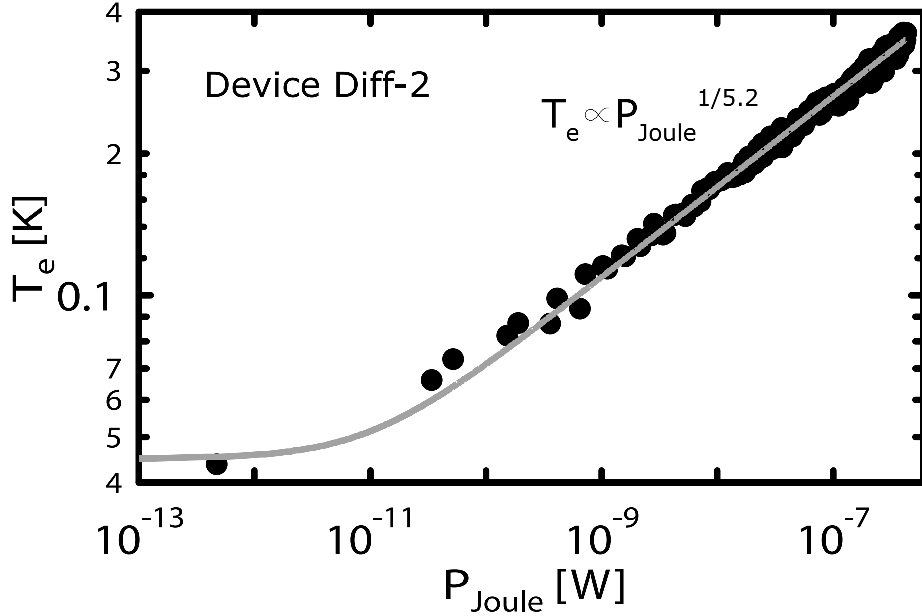

Figure 5.4: T_e vs. P_{Joule} for device Diff-2, long diffusive Au wire. The bath temperature $T_{bath} \approx 46$ mK.

$p \approx 3.2$. The result is not surprising; the device is relatively clean compare to the other three devices, it changes from "dirty" metal to "clean" metal as the bath temperature changes from ∼50 mK to ∼500 mK, therefore a $p \approx 3$ for the "moderate-disordered" regime is expected for the device. We will come back to this point with more details in the later section for electron-phonon time measurements.

5.2.2 The electron-phonon heat conductance from T_e vs. V_b curves

The quantity that characterizes the strength of the electron-phonon interaction is often given by the electron-phonon heat conductance, with the temperature dependence given in eqn.(3.5(d)). In our work, we extract the electron-phonon heat conductance from the small voltage bias part of the T_e vs. V_b characteristics[3]. For small voltage bias, when a steady state is reached in the Au film, the electron temperature is only slightly above the phonon temperature by the amount $\delta T_e = T_e - T_{bath}$. If $\delta T_e \ll T_{bath}$, it is justified to assume G_{e-ph} as a constant. Thus, δT_e is related to the bias voltage as

$$\frac{V_b^2}{R} = G_{e-ph}\delta T_e, \tag{5.4}$$

In other words, the T_e vs. V_b curve has a parabolic shape at the bottom (Fig.5.5), and

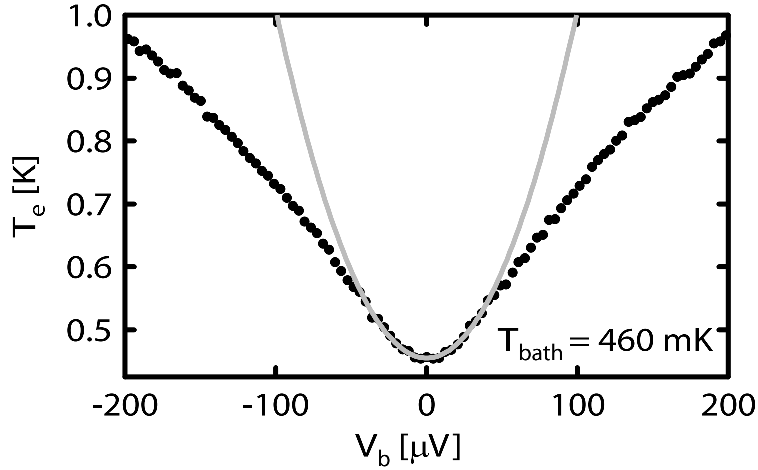

Figure 5.5: T_e vs. V_b curve for device SNS-2.
The bath temperature T_{bath} = 460 mK. The data are given by the dots. The solid line is a parabolic curve $T_e = a + bV_b^2$ fitted to the small bias part of the data. The electron-phonon heat conductance is thus derive from the fitting parameter b as $G_{e-ph} = 1/bR$.

[3] This is essentially the same as the T_e vs. P_{Joule} characteristics. The Joule power is calculated from the bias voltage, $P_{Joule} = V_b^2/R$.

the coefficient of the square term equals to $1/G_{e-ph}R$, which gives a measurement of the electron-phonon heat conductance G_{e-ph}, at the electron temperature equaling to the bath temperature, $T_e = T_{bath}$.

The temperature dependencies of G_{e-ph} obtained from the parabolic fittings for device Diff-1, SNS-1 and SNS-2 are shown in Fig.5.6 (a),(b), and (c) respectively[4]. The open squares represent the data (the dots in Fig.5.6(c) are also data, but measured from a different refrigerator and with a slightly different rf setup), and the solid lines are power law curves with the form $G_{e-ph} = (p+2)\Sigma V T_e^{p+1}$, where p's are integers. The parameters Σ and p for the three devices are summarized in Table 5.3. At high temperatures, the measured G_{e-ph} of all three devices show an approx-

	volume $^\dagger(\mu m^3)$	Σ	p
device -1	3.2	4.4×10^9W/K^4	2
device -3	0.9	7.7×10^9 W/K^4	2
device -4	0.06	8.6×10^9W/K^4	2

† This is the volume of the wire between the conducting leads.

Table 5.3: Power law temperature dependence of G_{e-ph}.

imate cubic temperature dependence. The values of Σ's and p's in Table.5.2 and Table.5.3 agree reasonably well for all three device from the two sets of measurements. Within the three devices, the similar values of Σ's in the two tables indicate that the electron-phonon heat conductances scales linearly with the device volume (within a factor of 2), as expected from eqn.(3.5(d)). This is better illustrated in Fig.5.7, where the electron-phonon heat conductances per unit volume of the three devices are plotted against the electron temperature. However, at low temperatures, G_{e-ph} saturates. For example, in Fig.5.6(a) the grey dashed lined gives a least squares fitting, $G_{e-ph} = G_0 + AT_e^{p+1}$, to the data, with the fitting parameters $G_0 = 3.2\times10^{-9}$

[4] G_{e-ph} for device Diff-2 is measured in a different approach presented in the next section.

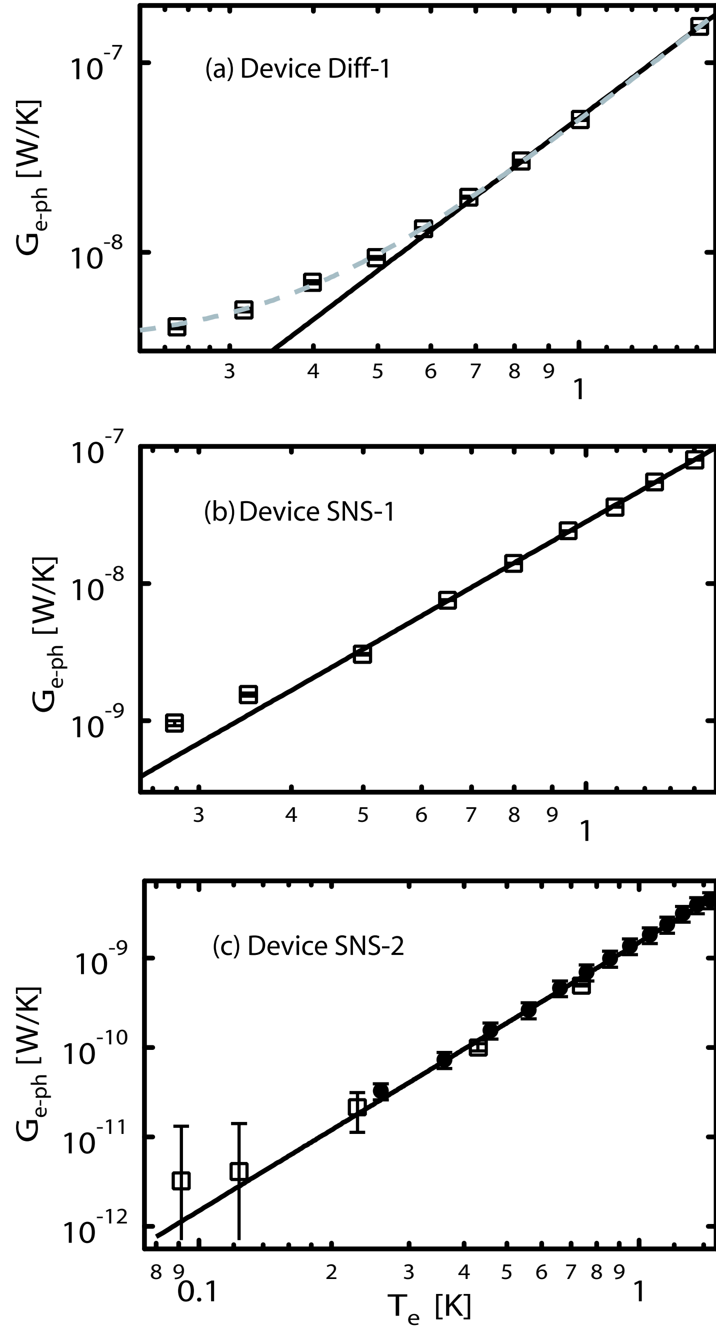

Figure 5.6: The temperature dependence of the electron-phonon heat conductances. Figure (a), (b) and (c) are G_{e-ph}'s for device Diff-1, SNS-1 and SNS-2 respectively. They are extracted from the parabolic fittings of T_e vs. V_b curves. The squares are the data. The dots in (c) are data taken in a different cryostat. The solid lines represent the power law dependence, $G_{e-ph} = (p+2)\Sigma V T^{p+1}$, with integer p.

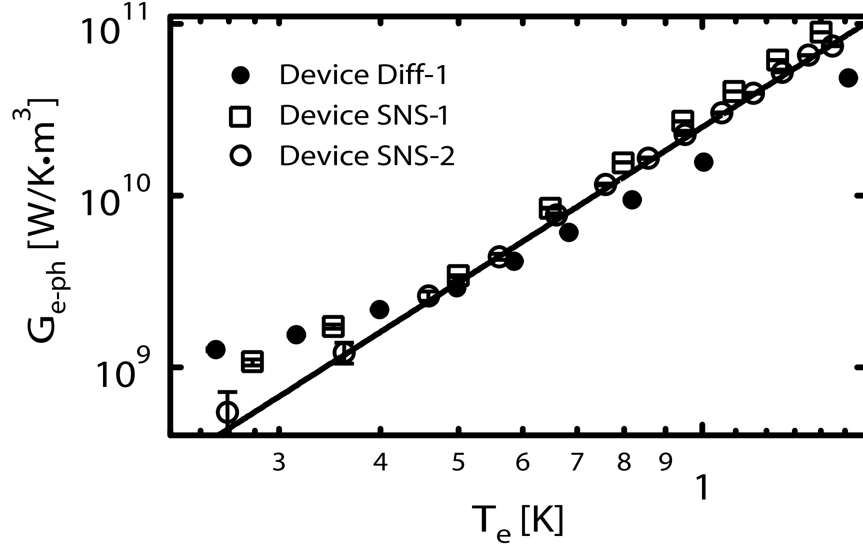

Figure 5.7: Comparison of the G_{e-ph} per unit volume.
The dots, squares, and circles represent the data for device Diff-1, SNS-1, and SNS-2 respectively. The solid line is a $G_{e-ph} \propto T_e^{p+1}$ curve with $p = 2$, as a guide to eyes.

W/K, $A = 4.7 \times 10^{-8}$ W/K$^{3.8}$, and $p = 1.8$. The saturation is possibly caused by excessive heating, uncertainties in the electron temperature measurement, or parallel diffusive heat flow paths for devices without superconductor Andreev reflected mirrors. We will discuss this at the end of the section.

5.2.3 Direct G_{e-ph} measurement with lockin amplifier

The above approach for extracting the electron-phonon heat conductance, however, is not a direct measurement. Moreover the number of data points is rather limited for a given measuring duration; we can acquire one data point every 20 minutes or so. Alternatively, we can use a lockin technique to directly measure the electron-phonon heat conductance from the Johnson noise of the hot electrons.

At zero bias voltage, if a small sinusoidal AC excitation $\delta V_b \sin(\omega t)$ is applied to the device, the change in the electron temperature, δT_e, is derived from the Taylor

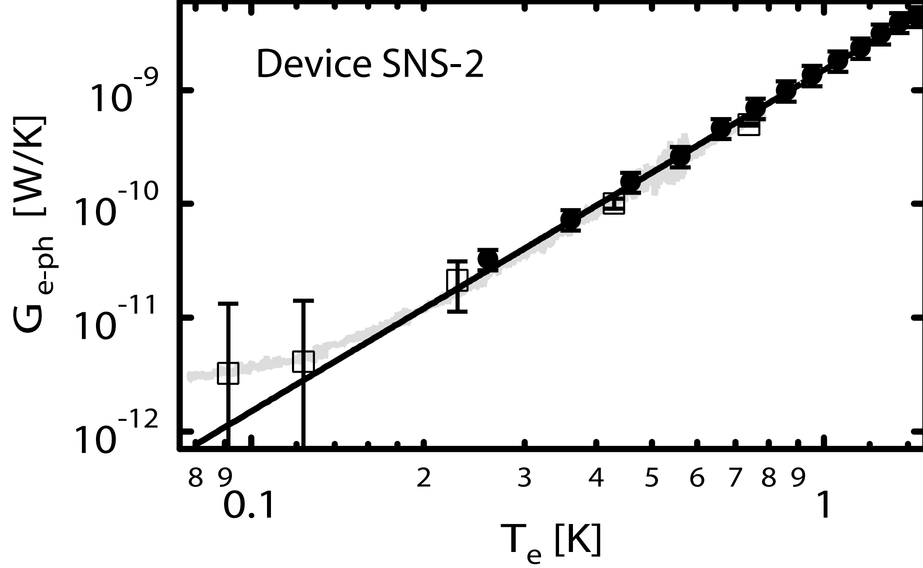

Figure 5.8: The temperature dependence of G_{e-ph} for device SNS-2.
The small grey dots are the data from lockin measurements, the open squares and the large dots are the data taken from parabolic fittings, and the solid line is a power law curve with the form $G_{e-ph} = 1.5 \times 10^{-9} T_e^{p+1}$, $p = 2$.

expansion of T_e as

$$\delta T_e = \frac{\partial T_e}{\partial V_b} \delta V_b \sin(\omega t) + \frac{1}{2} \frac{\partial^2 T_e}{\partial V_b^2} (\delta V_b \sin(\omega t))^2 + o(\delta V_b^3), \tag{5.5}$$

Since the first derivative of the electron temperature $\partial T_e / \partial V_b = 0$ at the bottom of the parabola, the small change in T_e to the lowest order is

$$\delta T_e \approx \frac{1}{2} \frac{\partial^2 T_e}{\partial V_b^2} (\delta V_b \sin(\omega t))^2. \tag{5.6}$$

The second derivative of T_e is equivalent to the coefficient of the parabola, i.e. $\partial^2 T_e / 2 \partial V_B^2 = 1/RG_{e-ph}$, and it can be directly measured by using a lockin amplifier at the 2nd harmonic[5]. This setup allows us to measure the G_{e-ph} continuously at $T_e = T_{bath}$ while sweeping the bath temperature, and the sampling rate is only limited by the lockin amplifier's time constant; we typically measure once every 3 seconds.

[5]See Chapter 4 for details of the setup.

The electron-phonon heat conductance G_{e-ph} from lockin measurement (small grey dots) as a function of the electron temperature T_e for device SNS-2 is plotted in Fig.5.8, overlayed by the data from the parabolic fittings (the large dots and the squares). The solid line is a power law curve $G_{e-ph} \propto T^{p+1}$ with an integer p. The data follow the power law line reasonably well down to about 160 mK, but saturate at lower temperatures. The data are also consistent with the two data sets from the parabolic fitting, and the resulted $p = 2$ is consistent with that from the T_e vs. P_{Joulse} as well.

The lockin technique is also used for measuring G_{e-ph} in device Diff-2, and the results are plotted in Fig.5.9. G_{e-ph} shows somehow different temperature dependence

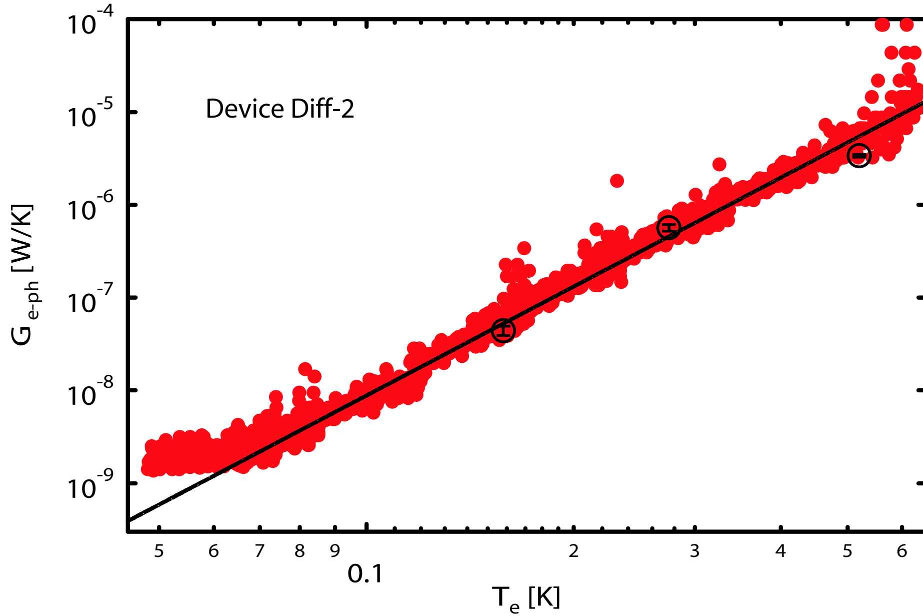

Figure 5.9: Temperature dependence of G_{e-ph} for device Diff-2. The dots are data from lockin measurement and the solid line is a power law curve with the form $G_{e-ph} = 1.3 \times 10^{-4} T_e^{(p+1)}$, $p = 3$. The open circles are a few G_{e-ph}'s measured from the parabolic fitting to the T_e vs. V_b curves.

from the other three devices; the power law index $p = 3$. As mentioned previously, this is due to the lower degree of disorder in the film than the other three devices.

The values of p and Σ extracted from curve agrees well with that from the input Joule power dependence of electron temperature presented in Fig.5.4. Despite the different power law temperature dependence of G_{e-ph} between device Diff-2 and the rest devices, its G_{e-ph} per volume agrees with the other devices qualitatively well, as illustrated in Fig.5.10.

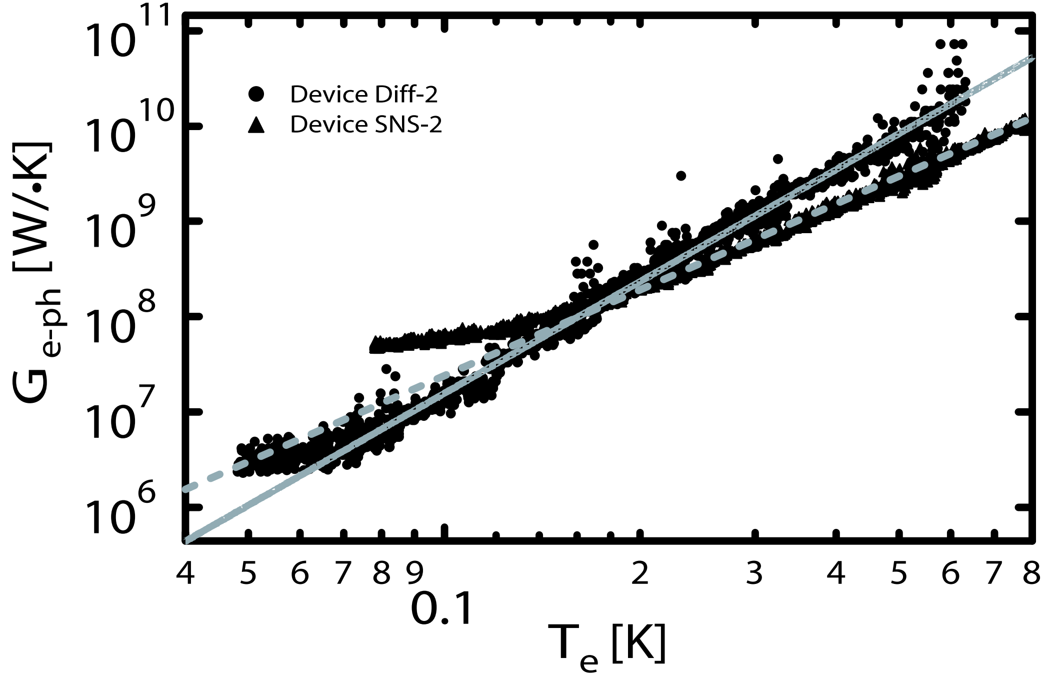

Figure 5.10: Comparison of G_{e-ph} per volume for device Diff-2 and SNS-2. The triangles are data for device Diff-2 and the dots are data for device SNS-2 from lockin measurements. The grey solid line and the dashed line are power law lines ($\sim T_e^4$ and $\sim T_e^3$) that approximate the data for device Diff-2 and SNS-2 respectively.

5.2.4 The saturation of G_{e-ph} at low temperatures

In this subsection we try to give possible explanations to the saturation of G_{e-ph} at low temperatures, using device Diff-2 and SNS-2 as examples.

The excessive thermal radiation from the cold amplifier

The saturation of the electron-phonon heat conductance might be an artifact due to the actually higher electron temperatures; if the measured electron temperatures were lower than the actual values, the data points in G_{e-ph} vs. T_e would shift to the lower temperature side, causing a flatter temperature dependence for G_{e-ph}. Excessive thermal radiations that reach the sample might cause the electrons to be heated above the bath temperature even at zero bias, inducing an electron temperature higher than that of the bath. We have indicated in Chapter 4 that the largest source for the heating is the thermal radiation of the cold amplifier. The radiation in the measurement frequency band, 1.25–1.75 GHz, can be estimated as follows. The amplifier is equivalent to a 50 Ω resistor at its noise temperature $T_A \sim$ 5K. Since $k_B T_A \ll h\nu$ in the whole frequency band, the noise power transmitted to the sample can be calculated in the Rayleigh-Jeans regime as $k_B T_A B \approx 4 \times 10^{-14} W$, $B = 500$ MHz being the system bandwidth. The power is further attenuated about -20 dB as it passes through the cold circulator. Eventually, only about $4 \times 10^{-15} W$ reaches the device. For device SNS-2, even at the lowest measured temperature ($\sim$ 80 mK), this only heats up the electrons by $4 \times 10^{-15}/1 \times 10^{-12} \approx 4$ mK, where $1 \times 10^{-12} W/K$ is the electron-phonon heat conductance at 80 mK. For device Diff-2, this effect is even smaller, since the electron-phonon heat conductance is much larger than that of device SNS-2 due to its large volume. In fact, the noise calibration curves in Fig.4.5(a) gives a good indication of the absence of excessive heating (within 30 mK or so); the temperature dependence of the noise output from the refrigerator agrees very well with a straight line.

Electron temperature uncertainty

We have mentioned in Chapter 4 that the gain and the noise temperature of the cold amplifier might drift during the time of measurement. It is shown in Fig.4.5(b) that at the base temperature of the refrigerator, the measured electron temperature T_e's from two consecutive bath temperature sweep differ by 30 mK or so for device Diff-2 (40 mK or so for device SNS-2, the noise calibration curve is not shown). Our G_{e-ph} temperature sweep in the lockin measurement duration is close to the duration for a noise calibration sweep. We assume that the rates of the amplifier drift for both sweeps are the same. Therefore, we have about 30 mK uncertainty in our electron temperature measurement. In Fig.5.11, we show the G_{e-ph} for device Diff-2 and SNS-2 by taken into account the uncertainties of the temperature. The grey horizontal bars in both plots represent the uncertainty at the lowest measured temperature; for Diff-2 the it is $\sim$ 30 mK at 46 mK, for SNS-2 it is $\sim$ 40 mK at 75 mK. For the device Diff-2, the G_{e-ph} saturation is eliminated within the uncertainty. But the saturation in device SNS-2 can not be completely explained by the uncertainty.

The diffusive cooling at the sample ends for long diffusive wires

In the long diffusive wire sample, device Diff-2, the diffusive cooling of the electrons at the ends of the wire adds additional heat conductance to G_{e-ph}. The measured heat conductance is effectively $G_{eff} = G_{e-ph} + G_{diff}$, where G_{diff} is the effective the diffusion heat conductance. The upper limit of the this additional heat conductance can be estimated by using eqn.(3.9), in the absence of the electron-phonon interaction,

$$G_{diff} \approx (12\mathcal{L}/R)T_{bath} = 6 \times 10^{-9} T_{bath}. \tag{5.7}$$

where $\mathcal{L} = 2.45 \times 10^{-8}$ WΩ/K^2 is the Lorenz number. The diffusion heat conductance, in all measurement temperature, is much smaller than the the measured G_{e-ph};

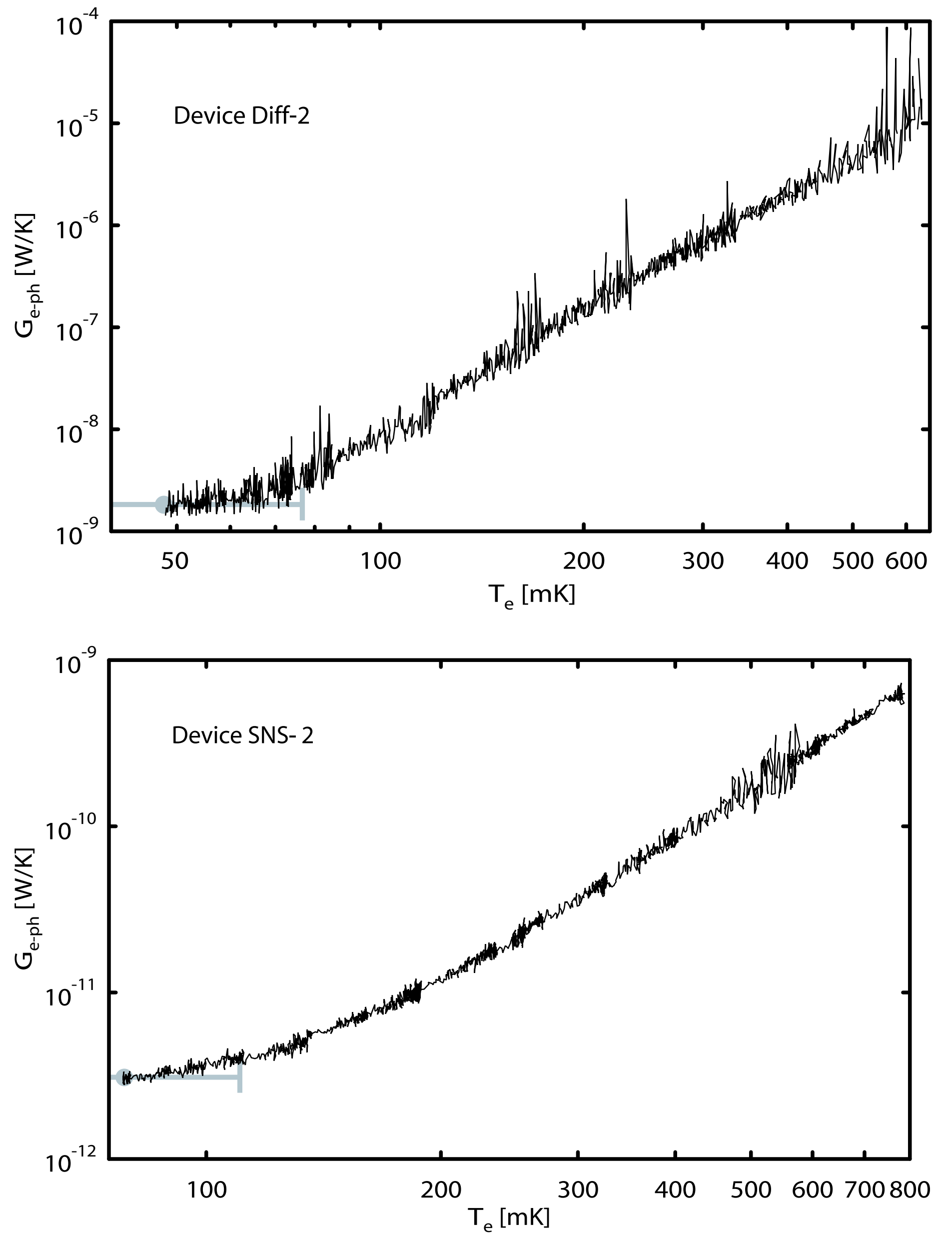

Figure 5.11: The uncertainty in the electron temperature induced by amplifier drifts. It is partially responsible for the saturation of the electron-phonon heat conductance at low temperatures. The horizontal grey bars represent the uncertainties of the electron temperature measurements.

it does not make significant corrections to the results.

5.3 Electron-phonon dynamics

For the direct measurement of the electron-phonon interaction time τ_{e-ph} and the electronic heat capacity C_e, we observe the electron heating and cooling dynamics in the time domain, in response to fast heat pulses. When the electron gas is heated by fast rising/falling heat pulses, whose rise/fall time $\tau \ll \tau_{e-ph}$, the electron temperature T_e is unable to follow the pulses; thus the electrons respond to the heat pulses on the time scale τ_{e-ph}. In this section, we discuss the direct time domain measurement of the electron temperature dependence on long heat pulses. It enables us to extract the electron-phonon interaction time τ_{e-ph} from the exponentially falling and rising of T_e as a function of time. The direct measurement of the electronic heat capacity C_e with short heat pulses will be discussed in the next section.

5.3.1 The electron-phonon time τ_{e-ph}

Let us start with the electrons' time response to "long" heat pulses, from which we measure the electron-phonon time τ_{e-ph}. The pulses used in the measurement are in fact square waves, as shown in the top panel of Fig.5.12. The rise/fall time of the pulse from the function generator is so short ($<$ 10 ns) that we assume the pulse has infinitely sharp edges. The pulse switches between the zero power (off) and a nonzero power level $P_s > 0$ (on), with the on and off times of the square wave much longer than the electron-phonon time τ_{e-ph}. Therefore, the electrons have enough time to exchange energy with the phonons, and eventually reach at a steady state.

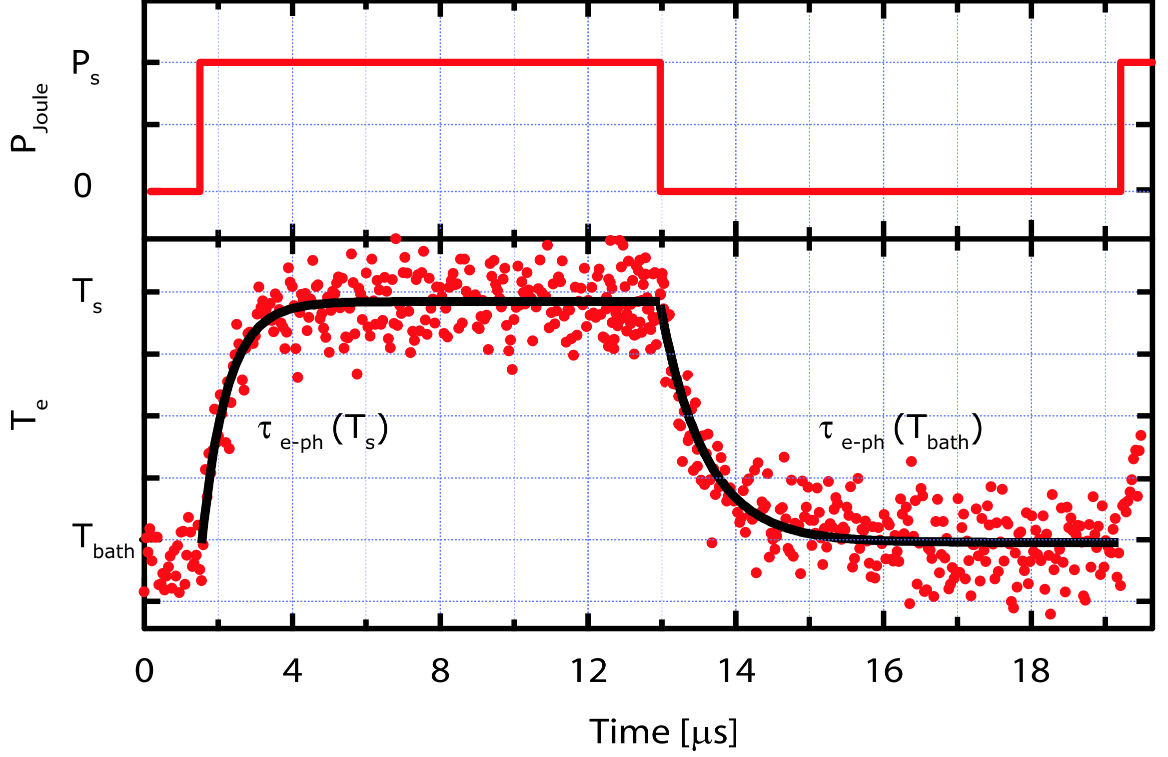

Figure 5.12: The time response of electron temperature T_e to a fast heat pulse. The top panel is a schematics of a square wave heat pulse applied to the device, and the bottom panel is the corresponding time response of electron temperature T_e of device SNS-2. The dots are the data, the solid lines are single value exponential fittings with the time constant as the fitting parameter.

The bottom panel of Fig.5.12 shows the corresponding time response of the electron temperature T_e to the heat pulse. When the heat pulse is on for a time period longer than τ_{e-ph}, the electrons heat up by absorbing energy from the applied electrical field, meanwhile, they cool down by transferring energy to the phonon system. Assuming the electron-phonon interaction is the only electron cooling mechanism, the net energy the electron gas obtained is the difference of the input energy from the electrical field and the energy flowing to the phonons. The heat balance equation is given as follows,

$$C_e(T_e)dT_e = (P_s - P_{e-ph}(T_e))dt, \tag{5.8}$$

where C_e and P_{e-ph} both depend on the electron temperature. For small temperature excursion $\delta T_e = T_s - T_e \ll T_e$, however, it is reasonable to assume C_e and G_{e-ph} are constant. For example, if $\delta T_e/T_e < 1/3$, the fractional change of $C_e \propto T_e$ is $\delta C_e/C_e < 1/3$, and the fractional change of $G_{e-ph} \propto T_e^{p+1}$ is $\delta G_{e-ph}/G_{e-ph} < (1/3)^{p+1} = 1/27$, with $p = 2$, and even smaller for higher values in p (3 or 4). Thus it is justified to write $P_s - P_{e-ph} \approx G_{e-ph} \cdot (T_s - T_e)$. Since $G_{e-ph} = C_e/\tau_{e-ph}$, the electron-phonon time constant τ_{e-ph} is also a constant, and the change in the electron temperature is written as

$$\frac{dT_e}{dt} \approx \frac{T_s - T_e}{\tau_{e-ph}(T_s)} \tag{5.9a}$$

$$T_e(t) = T_{bath} + (T_s - T_{bath}) \left(1 - e^{-t/\tau_{e-ph}(T_s)}\right). \tag{5.9b}$$

Note that, during the time period $\Delta t < \tau_{e-ph}$, starting from the onset of the heat pulse, the electrons only absorb energy from the applied electrical field, and there is no cooling channels for the electrons, as a result, the electrons are heated close to the equilibrium temperature T_s in a very short of time. Thus, the electrons cool down with the electron-phonon time constant at T_s, which can be extracted from the exponential fitting to the pulse rise, with $\tau_{e-ph}(T_s)$ as the fitting parameter. If the pulse duration is sufficiently long compare to the electron-phonon time, the electrons will eventually arrive at a steady state temperature $T_s(P_s)$ that is determined by eqn.(5.2b). Similarly, after the pulse is turned off, the electrons relax to the bath temperature on a time scale of $\tau_{e-ph}(T_{bath})$. The response at the pulse fall is expressed as

$$T_e(t) = T_{bath} + (T_s - T_{bath}) e^{-t/\tau_{e-ph}(T_{bath})}. \tag{5.10}$$

Hence we extract τ_{e-ph} at T_{bath} from the exponential fitting to the electron cooling time response.

The measured electron-phonon interaction time τ_{e-ph} as a function of the electron temperature T_e for device Diff-2, SNS-1 and SNS-2 are plotted in Fig.5.13. The dots,

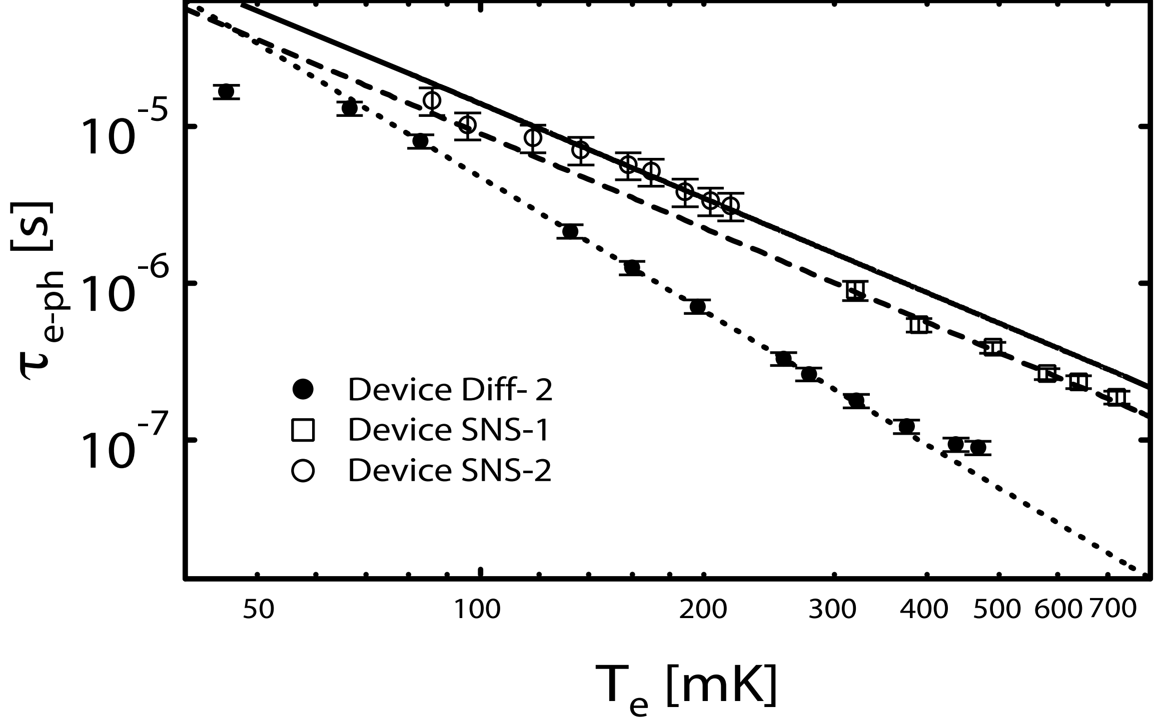

Figure 5.13: The temperature dependence of the electron-phonon time constant The dots, squares, and circles are for device Diff-2, SNS-1 and SNS-2 respectively, and the lines are the corresponding best power law fits, with integer power indices.

the open squares, and the open circles are data for device Diff-2, SNS-1 and SNS-2 respectively. The dashed line and the solid line are the least square power law fits to the data for SNS-1 and SNS-2, with the form $\tau_{e-ph} = \alpha^{-1}T^{-p}$, p being an integer. The dotted line is fitted to device Diff-2, and the two data points at the lowest temperature and the two data points at the highest temperature are excluded from the fitting for the following reasons: During the measurement of the two lowest temperatures, the temperature excursion δT_e is comparable to the bath temperature, the electron-phonon time should not be treated as a constant. Thus the electron-phonon time extracted from the single value exponential fitting curve is shorter than the ac-

tual value. At the two highest temperature, the measured time constant levels off; it indicates that we reach the time resolution limit of the system $\sim$ 80 ns, and what is measured is actually the system time of the setup. The fitting parameters for all three devices are listed in Table 5.4. The power law dependence of the three devices are all

	p	α
Device -2	3	1.4×10^8 s^{-1} $\cdot$K^{-3}
Device -3	2	1.1×10^7 s^{-1} $\cdot$K^{-2}
Device -4	2	0.7×10^7 s^{-1} $\cdot$K^{-2}

Table 5.4: The fitting parameters of τ_{e-ph} temperature dependence. τ_{e-ph} is fitted by the power law $\tau_{e-ph} = \alpha^{-1} T_e^{-p}$, with integer p.

in good agreement with their own $T_e(P_{Joule})$ characteristics and G_{e-ph} measurements discussed in the early sections. Although device SNS-1 and SNS-2 are measured at different temperature range, they have similar values in $\tau_{e-ph}(T_e)$, according to the fitting lines. However device Diff-2 has a different value of p and $\tau_{e-ph}(T_e)$ from the rest devices. The level of disorders in the films accounts for the discrepancy in the power law indices and the values of the electron-phonon time.

5.3.2 The electron-phonon interaction time in the dirty limit

Now it is important to revisit the issue of the “dirtiness” of the thin films. From Chapter 3 we know that the presence of even a little amount of disorder in the metal film could change the electron-phonon interaction time in the film drastically; the τ_{e-ph} depends on both the electron temperature and the electron mean free path ℓ. The level of disorder is determined by the quantity $q_{T,l(t)}\ell$, where $q_{T,l(t)} = k_B T/\hbar u_{l(t)}$ is the wave vector of the thermal phonon, $u_{l(t)}$ being the longitudinal (transverse) velocity of sound in bulk Au, $u_{l(t)} = 3240$ m/s (1200 m/s). $q_T \ell = 1$ is the dividing

point for clean and dirty metals; metal films with $q_{T,l}\ell > 1$ and $q_{T,t}\ell > 1$ are in the clean limit, films with $q_{T,l}\ell < 1$ and $q_{T,t}\ell < 1$ are in the dirty limit, and films with $q_{T,l}\ell \sim 1$ and $q_{T,t}\ell \sim 1$ are in the moderate disordered regime. In general, the electron-phonon interaction rate τ_{e-ph}^{-1} is dominated by the interaction between the electrons and the *transverse* phonons. So here we only evaluate the level of disorder according to the transverse phonons, i.e. $q_{T,t}\ell$, as shown in Fig.5.14, $q_{T,t}\ell$ is plotted

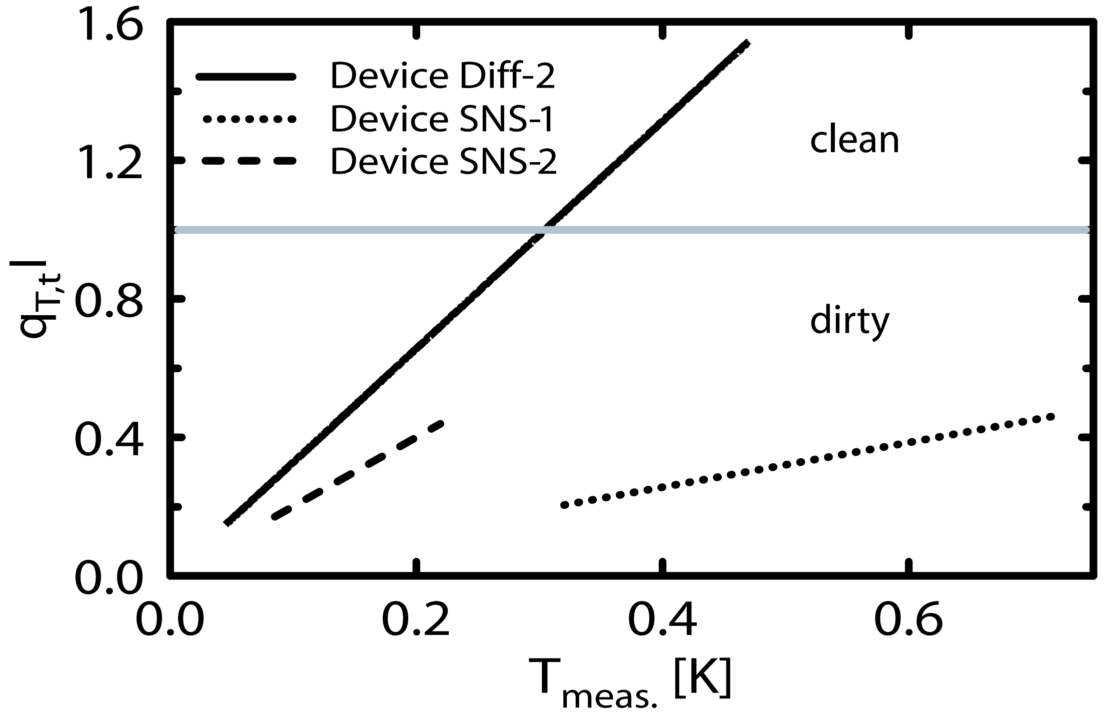

Figure 5.14: The level of disorder of devices the measurement ranges. The quantity $q_{T,t}\ell$ for the devices are plotted in black lines. The grey line in the plot divides the "clean" and "dirty" metal regimes.

against the measurement temperature $T_{meas.}$ for each device. The grey horizontal line at $q_{T,t}\ell = 1$ divides the clean and dirty regimes. It is clear that device SNS-1 and SNS-2 are in the dirty regime in the whole measurement temperature range. Device Diff-2, however, changes from dirty metal to clean metal as temperature increase; it is in the so-called "moderate" disordered regime.

The data of device SNS-1 and SNS-2 can be well explained by the theory for dirty metal films with incomplete phonon-dragged impurities, eqn.(3.27), with $\mathcal{L} \approx 2000$ Å. The comparison of the data and the theory is given in Fig.5.15. The squares and

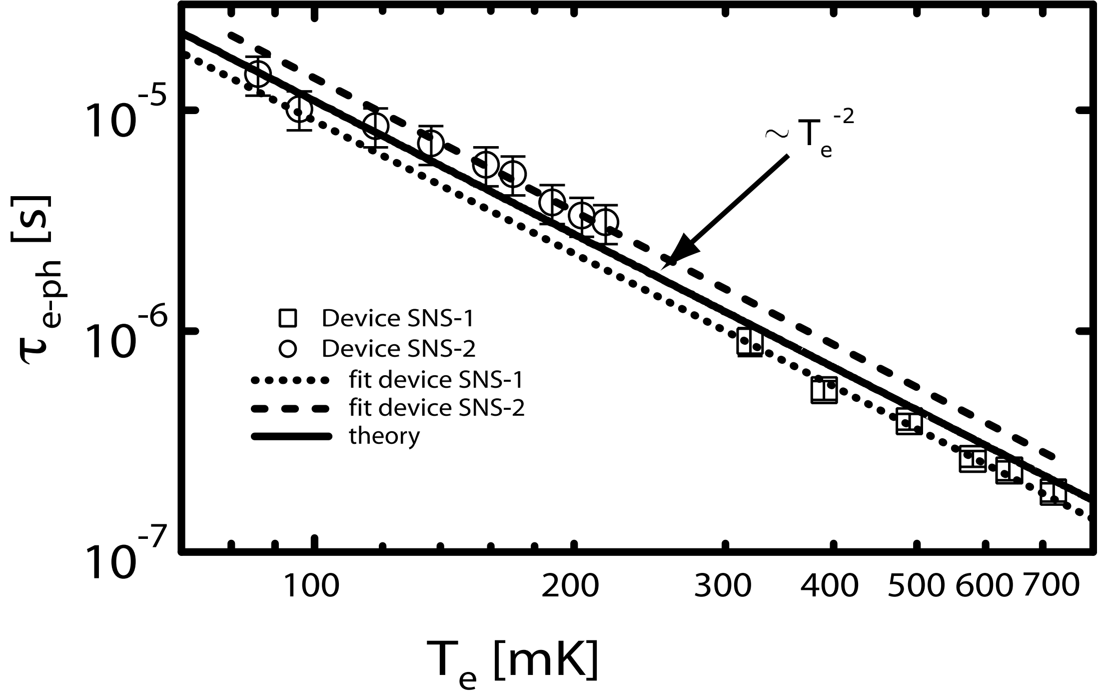

Figure 5.15: Comparison of τ_{e-ph} data and theory for device SNS-1 and SNS-2. The symbols are the data, the dotted line and the dashed line are the corresponding least square power law fits. The solid line gives the theoretically calculated time constant from eqn.(3.27).

the dotted line are the data and the least square T_e^{-2} fit for device SNS-1, and the circles and the dashed line are for device SNS-2. The solid line that pass between the two fitting curve is the theory, and it explains the data for both devices within a factor of two.

5.3.3 The electron-phonon interaction time in the moderate disordered regime

The electron-phonon interaction time for device Diff- 2 cannot be explained by the theory just in a single disorder regime; it changes from the dirty limit to the clean limit as the temperature increases above $\sim$ 300 mK, as indicated in Fig.5.14 by the grey line. In this regime, the transverse phonon dominates the electron-phonon interaction rate. The electron-phonon time can be calculated by evaluating the integration in eqn.(3.19) for $q_{T,t}\ell \sim 1$, with $\mathcal{L} \to \infty$, that is assuming the impurities are completely dragged by the thermal phonons[6]. This has been used by Sergeev & Mitin (2000) to successfully explain the data on Cu measured by Roukes et al. (1985). The evaluation of the integration is not in the scope of this thesis. However, for a good approximation, we calculate the electron-phonon time from both the dirty limit and the clean limit, by using the complete phonon drag expressions in eqn.(3.22) and (3.23) and plotted them with the data in Fig.5.16. The solid line is the time in the dirty limit, and the dashed line is in the clean limit. We can see that the calculated time brackets our data, and at the crossing temperature ($\sim$ 300 mK), it coincide with the measurement.

To summarize, we have measured the electron-phonon interaction time of disordered Au thin films in the dirty limit and the moderate disordered regime. The data can be explained by the theory (Sergeev et al. 2002) qualitatively.

[6]The electron-interaction in the intermediate regime does not strongly depend on the presence of the static impurities (see Chapter 3), thus we use the complete phonon-drag theories for the calculationSergeev & Mitin (2000).

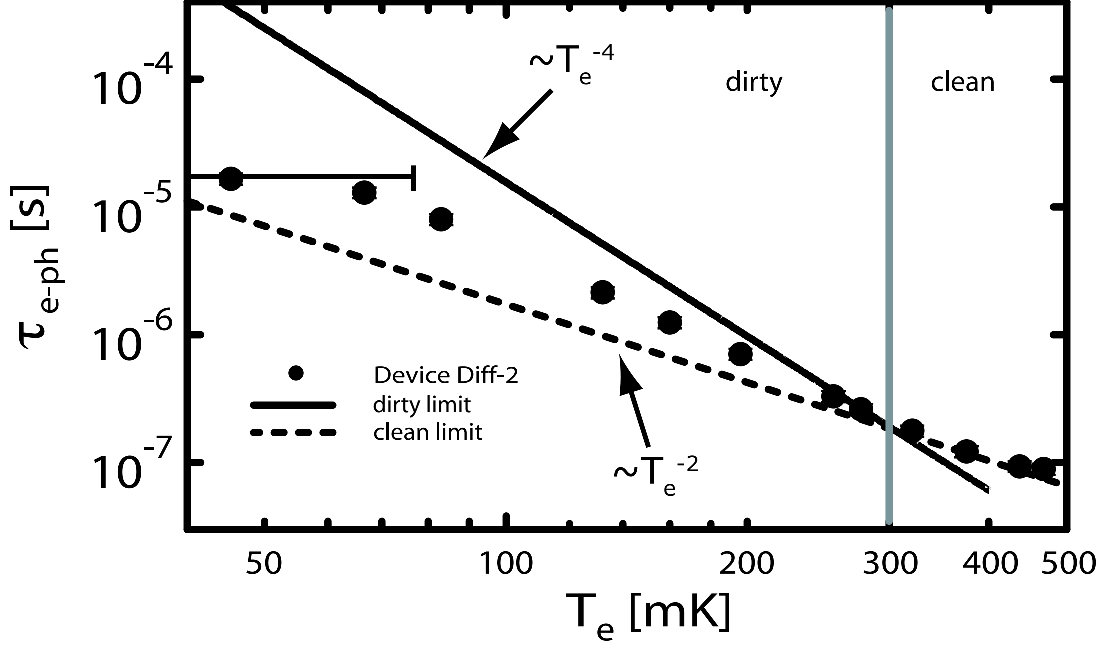

Figure 5.16: The comparison of data and theory for device Diff-2. The data are represented by the dots. The solid line and the dashed lines are the time constants calculated from the theory, for dirty limit and clean limit respectively.

5.4 The electronic heat capacity C_e

Our technique also enables us to measure the low temperature electronic heat capacity C_e of nano-scale metal thin films, that are deposited onto insulating substrate. Owing to the electron-phonon decoupling in the metal film at low temperatures, we are able to directly access the thermal processes of the electron gas, and measures only the electronic heat capacity, separating the capacities from other subsystems of the film (e.g. the phonon heat capacity).

5.4.1 The electronic heat capacity C_e from G_{e-ph} and τ_{e-ph}

With the measured G_{e-ph} and τ_{e-ph}, the electronic heat capacity C_e of the thin metal films can be derived from $C_e = G_{e-ph}\tau_{e-ph}$. The electronic specific heat (the electronic heat capacity per unit volume) for device Diff-2, SNS-1 and SNS-2 are plotted in Fig.

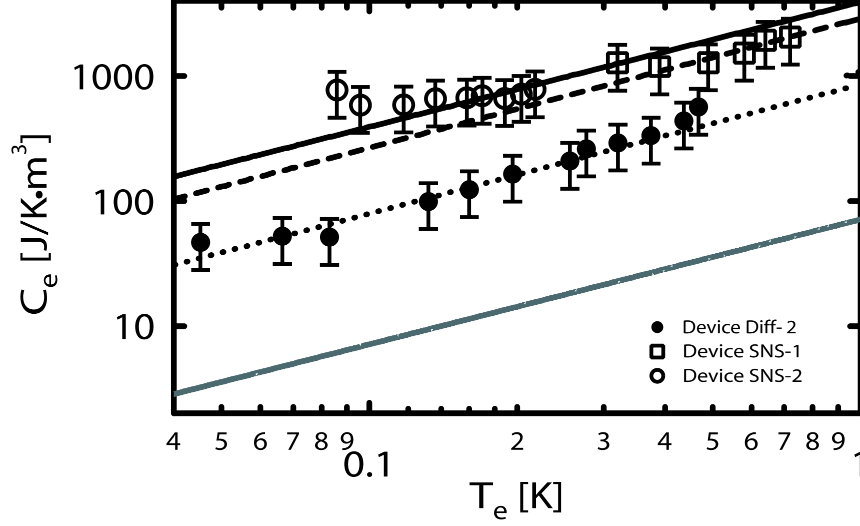

Figure 5.17: Comparison of the derived electronic specific heat for the devices. The symbols are the data. The dotted line, dashed line and the solid black line are power law fits to the devices. The grey line book value specific heat (Ashcroft & Mermin 1976, Kittel 1995).

5.17, as functions of electron temperature T_e. The dots, open square, and open circle are the specific heat calculated from the measured G_{e-ph} and τ_{e-ph}, for device Diff-2, SNS-1 and SNS-2 respectively. The dotted line, the dashed line, and the solid black line represents the corresponding linear fits to the data. For comparison, the solid line gives the electronic specific heat for bulk Au calculated from the book value (Ashcroft & Mermin 1976) Sommerfeld constant $\gamma = 0.729$ mJ/mol·K^2, with equation

$$C_e = \gamma \frac{n}{N_A} T_e, \tag{5.11}$$

where $n = 5.9 \times 10^{28}$ m^{-3} is the electron concentration in Au, and N_A is the Avogadro's constant.

The specific heat for all three devices is approximately a straight line as a function of electron temperature, as also can be seen from the fitting parameters of G_{e-ph} and τ_{e-ph}. However, the values of the devices do not complectly agree with each other; the specific heat of device SNS-1 and SNS-2 are consistent within a factor of 2, while

they are 3–5 times larger than device Diff-2. Moreover, even the specific heat of device Diff-2 is about 10 times larger than the book value. Possible explanations for the discrepancy are given in the end of the section. Before getting into any detailed data comparison, let us first show the electronic heat capacity measured from an alternative approach.

5.4.2 The electronic heat capacity C_e from calorimetry measurements

In this subsection, we describe a dynamic calorimetry approach for measuring the electronic heat capacity. This is a direct measurement of C_e, and it also provides a good cross check on the results from the product of G_{e-ph} and τ_{e-ph}.

Calorimetry is a direct approach for measuring heat capacity by observing the relation between the heat transferred to the system under study and the change of the system's temperature. When applied to electron gas, the relation is expressed

$$C_e = U/\Delta T_e, \tag{5.12}$$

where U is the heat/energy flowing to the electron gas, and assuming a constant electronic heat capacity. The assumption is valid when the change in the electron temperature ΔT_e is much smaller than the electron temperatures of the initial and final states. If the electrons are heated up by a constant Joule power P_{Joule} for a certain period of time Δt, the electronic heat capacity is given by

$$C_e = P_{Joule}\Delta t/\Delta T_e. \tag{5.13}$$

To perform our dynamic electron calorimetry, we apply a very short heat pulse to the device, and record the temperature response of the electron gas in the time domain. An example of the measurement is shown in Fig.5.18. The top panel is

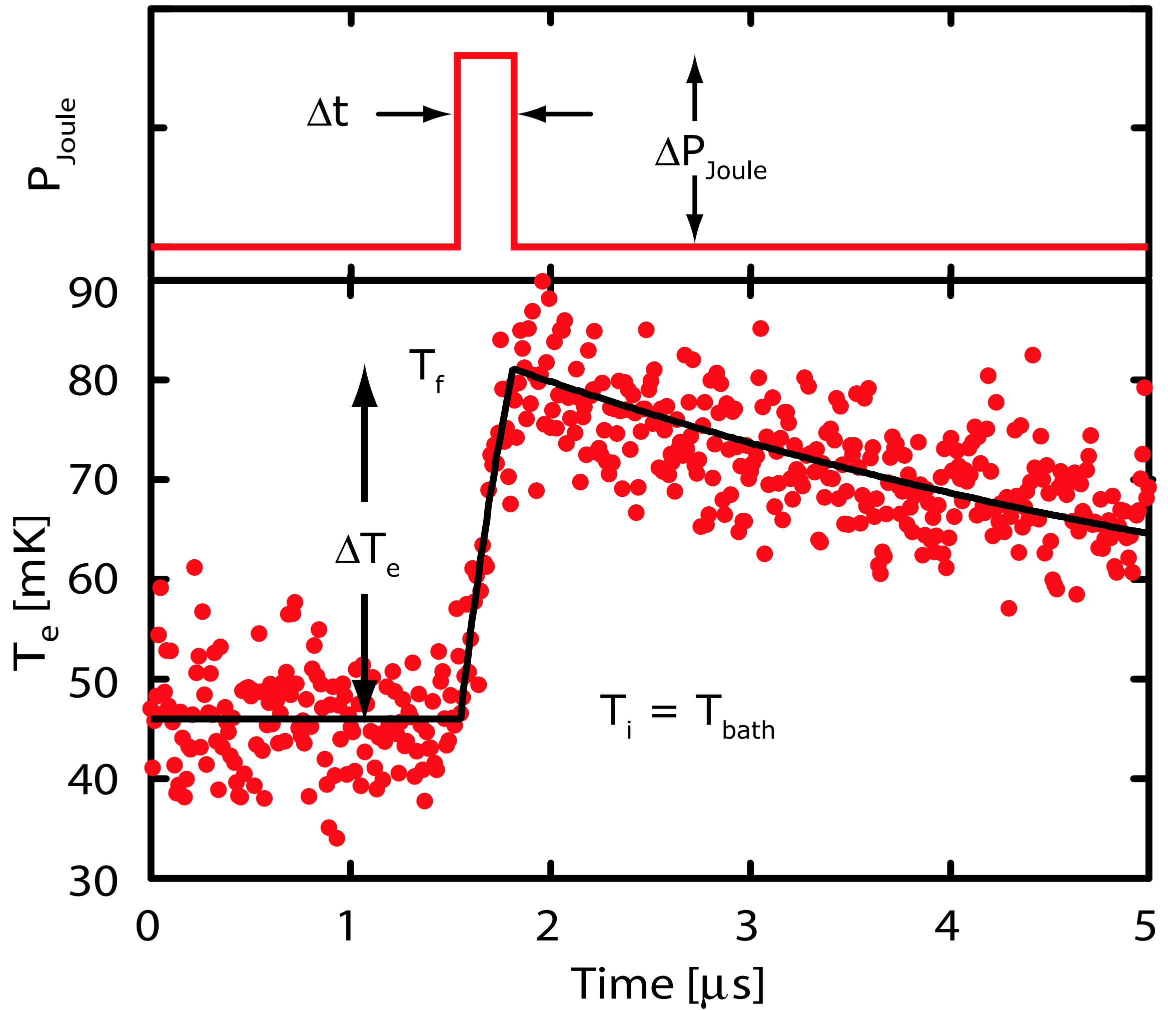

Figure 5.18: The calorimetry approach for measuring the electronic heat capacity. The top panel is the applied heat pulse, and the bottom panel is the corresponding electron temperature response. The dots are the data and the solid line is guide to eyes.

the applied heat pulse, during the very short pulse on time Δt, the pulse delivers constant Joule power to the device. The bottom panel of Fig.5.18 demonstrates the corresponding electron temperature T_e response to the short heat pulse. The dots are the data and the solid line is a guide to the eyes. During the on time of the pulse, the electron gas is heated from its initial temperature $T_i = T_{bath}$, to its final temperature T_f. If the pulse time $\Delta t \ll \tau_{e-ph}$, the electron gas heats up by absorbing energy from the heat pulse, and there is no heat flowing out from the electron gas to the phonons. The speed of the heating is only limited by the bias bandwidth of the setup, that is about 50 ns due to the bias-tee. The pulse duration has to by longer than the time resolution of the setup ($\sim$ 80 ns), such that we can follow the temperature change, therefore the electron temperature T_e increases linearly with the time at a rate $\Delta T_e/\Delta t = \Delta P_{Joule}/C_e$. After the pulse is turned off, the electron gas cools by interacting with the phonons on the electron-phonon interaction time scale. Fig.5.19 plots a set of data for the electronic calorimetry of device Diff-2. The curves are the time responses of the electron temperature for pulses with a fixed power but different pulse durations. The top most curve (data in solid triangles) is the response to a pulse whose duration is much longer than the electron-phonon time τ_{e-ph}, and the electron gas eventually reaches a steady state.

Note that, the simple linear relation between the electron temperature increase $\Delta T_e = T_f - T_{bath}$ and the pulse duration Δt, does not always hold; there are certain constraints. First, the pulse length Δt should be very short and the pulse power should be small, such that $\Delta T_e \ll T_e$, thus the electronic heat capacity C_e can be assumed to be a constant. Fig.5.20(a) shows the time response of the electron temperature T_e to pulses with relatively short durations comparing to τ_{e-ph}, 0.1 μs, 0.25 μs, and 0.5 μs, In addition, we plot a straight line (the dashed grey line) along the pulse rise.

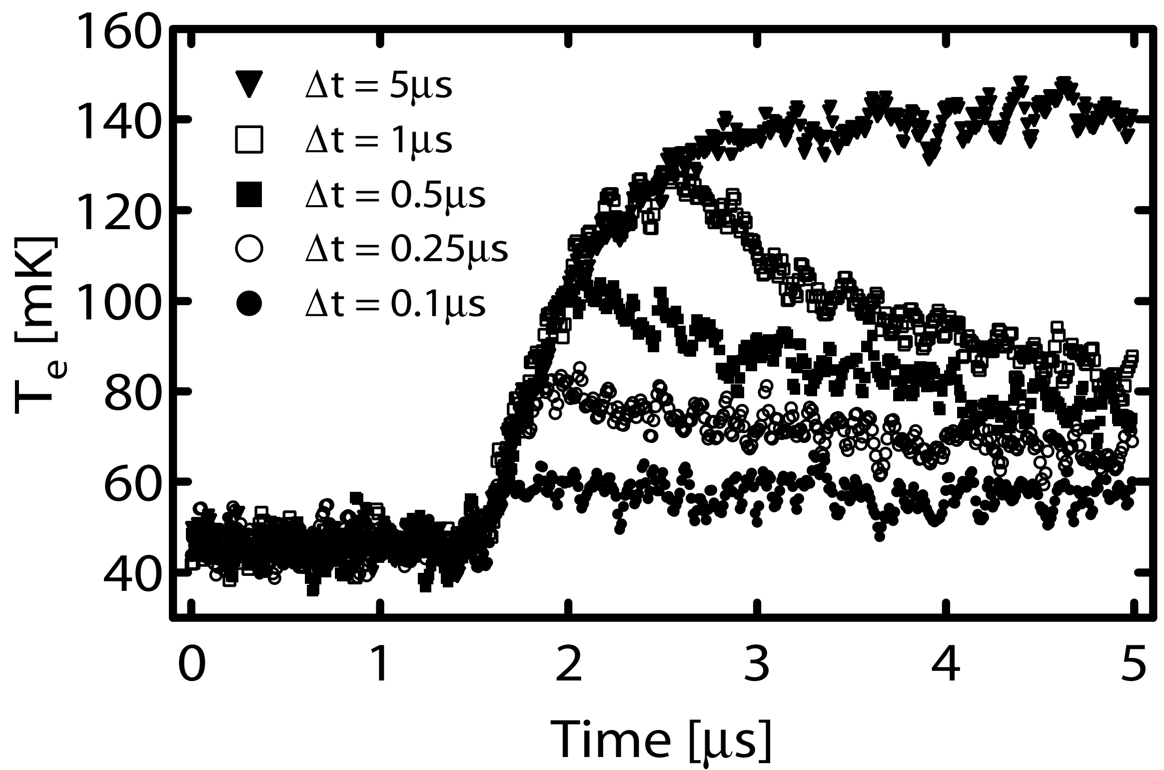

Figure 5.19: The electron temperature responses to heat pulses for device Diff-2. The heat pulses have the same power during the on time, but they have different pulse duration. The bath temperature is $T_{bath} = 44$ mK.

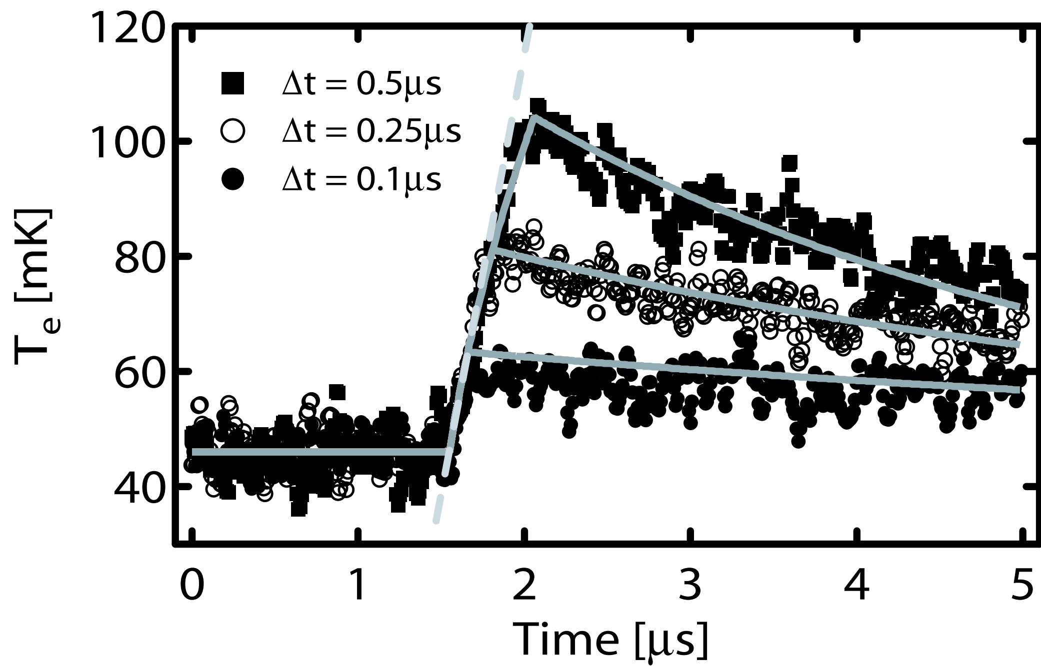

(a)

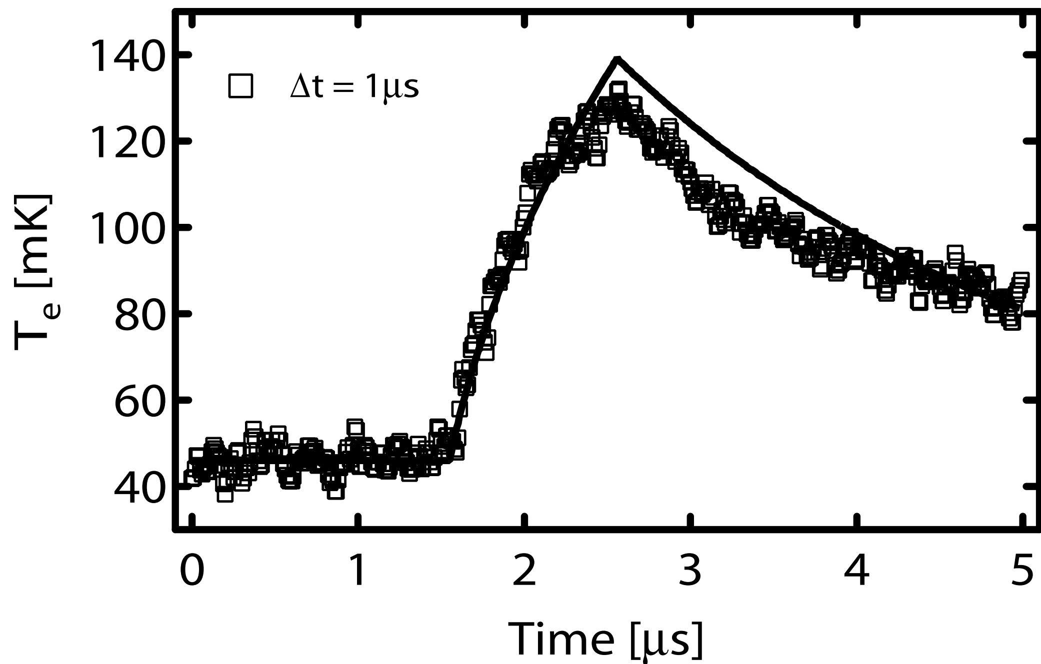

(b)

Figure 5.20: The time response of electron temperature T_e to short heat pulses. (a) The T_e response of device Diff-2 to pulses that are much shorter than τ_{e-ph}. No cooing is involves. (b) The T_e response to a pulse whose duration is comparable to τ_{e-ph}, the electrons starts to transfer energy to the phonons, indicated by the deviation of the data points from the solid line.

The pulses with $\Delta t = 0.1$ μs and 0.25 μs roughly follow the line, but the pulse with Δt=0.5 μs shows a nonlinear time dependence and deviates from the straight line at higher electron temperatures, since the electronic heat capacity ($C_e \propto T_e$) increases as the electrons heat up, and the rate of temperature change decreases. In this case, the electron temperature response is better described by a changing $C_e(T_e)$ as follows

$$\delta T_e = \frac{\Delta P_{Joule} \cdot \delta t}{C_e(T_e)} = \frac{\Delta P_{Joule} \cdot \delta t}{C_0 T_e}, \tag{5.14}$$

where δT_e is the small temperature excursion at temperature T_e, in response to a short period of time δt. The electronic heat capacity is assumed to depend on T_e linearly, $C_e(T_e) = C_0 T_e$. The data in Fig.5.20(a) are overlaid with the calculated T_e from the above relation in grey solid lines. A single parameter, $C_0 = 8.5 \times 10^{-5}$, is used for all three curves, which describe the data reasonably well. It is interesting to look in to the T_e time response to a longer pulse. As the pulse duration becomes comparable with the electron-phonon interaction time, the electron-phonon cooling channel is open; the electrons cool down while absorbing energy from the heat pulse. This is illustrated in Fig.5.20(b), for the electron temperature response to a 1 μs long heat pulse. The open squares are the data, the solid line is calculated from the above relation (the electron-phonon time at 130 mK is about 1 μs, as shown in Fig.5.13). The data follow the curve from the bath temperature to about 120 mK, that is about 75 ns from the onset of the pulse. The data then start to deviate from the curve, indicating that the electrons are losing energy to phonons.

In conclusion, we directly measured the electronic heat capacity C_e by using dynamic calorimetry with short heat pulses, assuming constant C_e. We also extracted the heat capacity by fitting the data with a temperature dependent $C_e = C_0 T_e$. Both data show good agreement with the electronic heat capacity derived from G_{e-ph} and τ_{e-ph}. The results of the specific heat for a couple of temperatures are summarized

T_e (mK)	C_{cal}	C_0	$C_{G\tau}$	C_{book}
45	35	35	47	3.2
84	73	66	52	6

Table 5.5: Summary of the measured electronic specific heats.
C_{cal} and C_0 are from calorimetry measurements with constant and changing heat capacity respectively. $C_{G\tau}$ is calculated from the measured G_{e-ph} and τ_{e-ph}. C_{book} is the book value (Ashcroft & Mermin 1976, Kittel 1995)

in Table 5.5, together with estimation from the book value. The unit of all listed specific heat is J/K·m^3. The three sets of data are in reasonably good agreement, but are about 10 times higher than the book value.

5.4.3 Possible explanations of the large measured C_e

Magnetic impurity

It is known that the presence of magnetic impurities in metal can drastically change the heat capacity of the metal at low temperatures (Chatenier & Miedema 1966). The magnetic impurities introduce two-level systems with energy splitting $k_B\Delta$, which induce large peaks in the heat capacity (Fig.21(a)), known as *Schottky anomalies*. Each two level system contribute about $k_B/2$ to the heat capacity at its peak value. We can roughly estimate the density of magnetic impurity that can induce a heat capacity 10 times larger than that of the electrons. The electrons that contribute to the electronic heat capacity is about T_e/T_F ($T_F = 6.4\times10^4$ K is the Fermi temperature of Au) of the total electrons, and each of these electrons gives k_B to the heat capacity. Therefore, a concentration of $20 \times T_e/T_F$ for the magnetic impurity can cause the measured electronic heat capacity to be 10 times larger than its actual value. At 1 K, this requires 0.03% magnetic impurity in Au. However, the peak value is only available at temperature $T \sim \Delta$, and Δ lies in the range 1$\sim$100 mK (Kittel 1995). For a measurement temperature above 100 mK, each two level system contribution

to the heat capacity is much smaller than $k_B/2$. Fig.21(b) is an example for the effect of Schottky anomaly to the low temperature heat capacity (Chatenier & Miedema 1966) of Au with $\sim 0.1\%$ Fe impurity, for temperatures below about 1 K, the heat capacity is only about 3–4 time larger than that of the pure metal. If we naively scale the result with the concentration of the Fe impurity, we need about 1% of Fe impurity to account for the 10-50 times larger heat capacity we measured. However we know that it is impossible for our films to have such high magnetic impurities. The Au films are evaporated from 99.9999% pure Au source, in a deposition system free of magnetic impurity [7]. Therefore, this phenomenon by itself cannot explain our large measured heat capacity.

Although it is impossible to have such a high magnetic impurity concentration *in* the Au film, other forms of two level systems can exist on the thin film's surface and introduce extra heat capacity to the system. The property of the film surface is very different from that of bulk. There could be dangling bonds, on the surface. Also a few atomic layers of glass state film can form at the end of the Au evaporation, and cover the surface of the Au film. Both can introduce very high concentration of the two level systems on the film surface. Each of the two level systems could contribute as much as $k_B/2$ to the heat capacity. Since our Au is only about 100–200 atomic layers thick, even a monolayer of glass state with 100% density of two level systems on the surface is equivalent to $\sim$1% of magnetic impurities *inside* the film. According to the measurement in Fig.5.21(b), the surface states could easily cause a factor of 30 increase in the measured electronic heat capacity.

[7] The deposition system — the PLASSYS e-beam evaporator is designated for making superconductor junctions. Even a small amount of magnetic impurity can degrade the performance of the junction.

Parallel cooling channels

The surface states might provide a possible explanation to the enormously high heat capacity. However, in order for such model to be consistent with the rest of the measurement results, namely the electron heat conductance G_{e-ph} and the interaction time τ_{e-ph}, a thermal structure that is different from that in Fig.3.1(b) is needed. The modified structure (Fig.5.22) suggests an electron cooling channel that is parallel to the electron-phonon cooling channel. In the scheme, all the phonons, including the phonons in the metal film, in the substrate, and in the thermal bath, are considered as one phonon system at T_{bath}, as the Kapitza heat conductance in each phonon subsystem pair is very large compared to the electron-phonon heat conductance. The electrons now have two parallel cooling channels. One channel is the traditional phonon cooling channel, where the electron-phonon heat conductance is from that of the book value. The other channel is an energy transferring path that connects the electron gas to some thermal mass (e.g. the surface states), denoted as C_x, with heat conductance G_{e-x}. The thermal mass C_x also transfers energy to the phonon system, through heat conductance G_{x-p}. If the thermal link G_{e-x} is much larger than the electron-phonon interaction in the film, and is also much larger than the link G_{x-p}, the electron gas and the thermal mass are thermally "shorted", as depicted in the effective thermal diagram in Fig.5.22(b), they are combined into one thermal mass with the effective thermal capacity $C_{eff} = C_e + C_x$. C_{eff} transfers heat to the phonon system with the effective heat conductance $G_{eff} = G_{e-ph}+G_{x-p}$. Under these assumptions, our measured heat capacity, heat conductance, and the time constant are in fact C_{eff}, G_{eff} and $\tau_{eff} = C_{eff}/G_{eff}$. From previous sections, we know that the measured time constant is in good agreement with the electron-phonon interaction theory, so we assume $\tau_{eff} \approx \tau_{e-ph}$, which suggests that $C_x \approx AC_e$, $G_{x-p} \approx AG_{e-ph}$,

and $G_{e-x} \gg AG_{e-ph}$ where A ranges from 10 to 50 for different devices we measured. In other words, the unknown thermal mass (e.g. could be the two level systems) must couple with the phonons 10–50 times stronger than the electrons do, furthermore, it has to couple to the electrons even more strongly. Although we do not have good knowledge on the exact mechanism for heat transfer from the surface states to the electrons and the phonons of the metal film, it is hard imagine $G_{x-p} \approx AG_{e-ph}$, and $G_{e-x} \gg AG_{e-ph}$.

Another possible parallel cooling path for the electrons is heat transferring to the leads. In the SNS structures, the electron gas in the Au film can interact either with the phonons of the Au film or with the superconducting Nb leads at the ends. At the interface of Au and an ideal superconductor, and at temperatures well below the critical temperature T_c (about 6 K for our Nb film), the heat conductance is expected to drop exponentially as the temperature decreases (Andreev 1964), and it is much smaller than the G_{e-ph}. This does not satisfy our assumptions, therefore the large heat capacity cannot be explained by the model. However it is worth mentioning that it is well known in the detector community (Li et al. 2003), that at the Au–Nb contact, Nb could form metallic oxides, which may form local trapping sites. These traps might change the thermal properties at the Au–Nb interface, and allow the electrons to transfer heat to the Nb leads. In the future, it is interesting to invest the electron-phonon interaction in SNS structures where good transparent NS interface can be formed.

In the long diffusive wire sample, device Diff-2, whose conduction leads are also Au, it is possible for electrons to transfer heat to the leads by out diffusion. As discussed in previous section, the diffusion heat conductance is estimated as $G_{diff} = 6 \times 10^{-9} T_{bath}$. In our measurement temperature range, it is much smaller than the electron-phonon

heat conductance G_{eph} (Fig.5.24). Even when compared to $G_{e-ph}/10$, i.e. the "G_{e-ph}" according to the book value C_e, the G_{diff} is much smaller for temperature above 100 mK or so, and not much larger for lower temperatures. Therefore, there is no possible additional thermal path that can help to explain the anomaly in our measured electronic heat capacity.

In conclusion, to our knowledge, there is no plausible explanation for the unusually large electronic heat capacity in our Au thin films; at very low temperatures ($\lesssim 1$ K), the electronic heat capacity in disordered Au thin films on Si and oxidized Si substrates is 1–2 orders magnitudes larger than the book value. The above discussion cannot explain our large measured C_e with a satisfactory thermal model that can also explain the measured G_{e-ph} and τ_{e-ph} as the same time.

5.5 Applications in ultra-sensitive sub–mm HEB's

Besides the application in low–power sub–mm photon source, another very interesting application of the weak electron-phonon interaction is using nano-scale thin metal films as ultra-sensitive phonon–cooled sub–mm hot electron bolometers (HEB's) or hot electron direct detectors (HEDD's) (Nahum & Richards 1991, Gershenson et al. 2001).

5.5.1 The concept of the phonon–cooled HEB

Phonon–cooled HEBs utilize the weak electron-phonon interaction at low temperatures and the very small absorber volumes to achieve ultra high sensitivity for sub-mm photon detection. The devices are essentially same as the phonon cooled hot electron photon sources; they use metal thin film wires as photon absorbers, whose ends are connected to conducting leads. Fig.5.24 shows the thermal structure of the HEB, and

the operation concept of the photon detection. The HEBs are proposed to operate at very low temperatures, at which the electrons and the phonons in the metal film absorber are decoupled, and the phonons in the metal and the substrate are considered as one phonon system at the bath temperature T_{bath}. When a photon impinges on the absorber metal thin film, it heats up the electrons in the film the just as does an applied Joule power. The ends of the absorber wire are terminated by superconductor leads, which are used as Andreev reflection mirrors, so the photon generated hot electrons cannot cool by out-diffusion. The only thermal path for the electrons is thus the weak electron-phonon interaction, hence the name *phonon* cooled HEB. In steady state, the photon power P that is absorbed by the detector is measured by the temperature change of the electron gas, $\Delta T_e = P/G_{e-ph}$, assuming the photon power is very low, and the induced electron temperature excursion is very small compared to the initial bath temperature.

The intrinsic sensitivity of the phonon cooled HEBs is limited by the thermodynamic fluctuation and it is determined by the electron-phonon heat conductance of the absorber material:

$$NEP = \sqrt{4k_B T^2 G_{e-ph}}, \tag{5.15a}$$

since $G_{e-ph} = C_e/\tau_{e-ph} = \gamma V T_e/\tau_{e-ph}$, the NEP is equally expressed as

$$NEP = \sqrt{4k_B T^3 \gamma V/\tau_{e-ph}}, \tag{5.15b}$$

where γ is the Sommerfeld constant. For a given operation temperature, the sensitivity improves as the volume of the absorber decreases and the electron-phonon time increases.

The use of superconductor Andreev reflection mirrors, as discussed in previous chapters, makes it possible to have the length of the absorber wire shorter than the

electron-phonon length, $L < L_{e-ph}$. However, to ensure a uniform thermal distribution of the hot electrons in the wire, its length should be longer than the electron-electron length $L > L_{e-e}$, such that the electrons in the absorber can fully thermalize. These conditions can be satisfied in very low temperatures, for instance, below ~1 K for Au (Fig.3.2). Therefore, L_{e-e} sets the lower limit of the absorber length L. Let us now estimate the feasible minimal volume of the absorber wire, using Au as the example. The thickness d of the absorber should be large enough so that the film is continuous, therefore $d \sim 100$ Å. At this value, the evaporated Au films[8] have sheet resistance $R_\square \approx 4\ \Omega$. Thus the aspect ratio on the films is fixed for a given absorber resistance. For instance, if 50 Ω is required from the rf input matching to the antenna, the ratio of the absorber length to the width is $L/W = 12.5$. The minimal volume is thus $V = 8 \times 10^{-4} L_{e-e}^2\ \mu m^3$, with L_{e-e} in μm. To illustrate the minimal device volume, in Fig.5.25 we plot the theoretically expected temperature dependence of both the electron-electron length[9] L_{e-e} and the corresponding the minimal volume V_{min}.

The electron-phonon interaction time τ_{e-ph} can be controlled by adjusting the level of disorders of the films, as discussed in Chapter 3. Depending on the properties and the density of the disorders in the film, the electron-phonon time shows different temperature dependence, $\tau_{e-ph} \propto T_e^{-p}$, p=2–4. Regardless of the actual form of the temperature dependence, τ_{e-ph} drop quickly with temperature below 1 K, and it is usually longer than 1 μs. To give an idea of the potentially high sensitivity of the phonon cooled HEB, we estimate the NEP with eqn.(5.15b) at 100 mK for

[8]These are the Au films deposited in our PLASSYS e-beam evaporator from 99.9999% purity Au source. The sheet resistance $R_\square = 4\Omega$ is estimated from the measured $R_\square$ for 200 ÅAu film, deposited under the same conditions.

[9]This is calculated for quasi-1D wires with eqn.(3.1(a))

a Au film with the minimal volume (0.06 μm^3) and 10 μs electron-phonon time[10], $NEP \approx 1.5 \times 10^{-19}$ W/$\sqrt{Hz}$. This is what is expected from future sub-mm and far-infrared (FIR) radioastronomy missions photon detectors (Mather et al. 2002), and is 2 orders of magnitude better than the state-of-art conventional HEBs (Gershenson et al. 2001).

The sensitivity can be further improved by using metal films that have the weakest electron-phonon interaction ($\tau_{e-ph} \propto T_e^{-4}$) as the absorber material; the weaker the interaction, the longer the interaction time. This dependence has been observed in complete phonon-drag strong disorder ($q_T l \ll 1$) Ti, Hf (Gershenson et al. 2001), and Bi (Komnik et al. 1994) thin films. The measurement by Gershenson et al. (2001) suggests a record 25 ms electron-phonon time for Ti and Hf films at 40 mK. They project a 2–3$\times 10^{-20}$ W/$\sqrt{Hz}$ NEP for 0.025 μm^3 Ti (or Hf) films at 100 mK.

5.5.2 Potential problems for the HEB performance

The above estimated sensitivities for the phonon cooled HEB are very promising. However there are several potential problems suggested by our electron-phonon interaction results that could degrade the HEB performance. It is interesting to discuss the performance of device SNS-2 as an HEB, since its volume is approaching the minimal absorber volume when the temperature is below 140 mK. In Fig.5.26 we compare the actual NEP calculated from the measured electron-phonon heat conductance (the dots) and the NEP estimated from the book value electronic heat capacity (the solid line).

[10] Approximate value for the measured τ_{e-ph}'s for device Diff-2, SNS-1 and SNS-2.

The larger electronic heat capacity

The estimations of the NEPs from above are all based on one assumption — the electronic heat capacity of the absorber film is calculated from the book value Sommerfeld constant γ (e.g. Ashcroft & Mermin (1976), Kittel (1995)). To our knowledge, there is no experiment on single material[11] that explicitly measures both the electron-phonon heat conductance and the electron-phonon time together, the value of one quantity is always inferred from the measured quantity, assuming the book value electronic heat capacity. Thus, there is no check on the electronic heat capacity. Our measurements discussed in the previous sections suggest that the book value electronic heat capacity might not be accurate at very low temperatures in nano-scale thin films; the measured electron heat capacity is 10–50 times larger than the book value. The actual NEP for device SNS-2 when used as an HEB is thus about one order of magnitude worse than that from the book value, i.e. $\sim 1 \times 10^{-18}$ W/$\sqrt{Hz}$.

It is worth mentioning that if this large electronic heat capacity also exists in the Ti and Hf in Gershenson's (Gershenson et al. 2001) work, the NEP falls in the 1–2$\times 10^{-19}$W/$\sqrt{Hz}$ range, which barely satisfies the photon-noise-limited NEP for future FIR missions.

The saturation of G_{e-ph} at low temperatures

The sensitivity of the HEB can be also improved by working at lower temperatures. However our measured G_{e-ph} in the SNS structure (device SNS-2) saturates at low temperatures, with the value $\sim 3 \times 10^{-12}$ W/K. As a result, the improvement of the device sensitivity also slows down towards the low temperatures; the NEP$\propto T$ instead of $T^{2.5}$, assuming a cubic temperature dependence of G_{e-ph}. The NEP of the

[11] Schmidt, Yung & Cleland (2004) have measured both the electron-phonon heat conductance and the electron-phonon time together, however, the composition of the sample film is very complicate.

device cannot reach the expected photon-noise-limited NEP$\sim 1 \times 10^{-19}$W/$\sqrt{Hz}$ at a reasonable working temperature ($\gtrsim$ 50 mK).

The volume scaling

Finally, the sensitivity of the phonon cooled HEB scales with the square root of the absorber volume $NEP \propto \sqrt{V}$; naively we can improve the sensitivity by decrease the volume. However, there is a lower limit for the size of the absorber, and the lower the operating temperature, the larger the size limit. We can estimate the "ultimate" NEP (i.e. the NEP for the film with the minimal volume for given temperatures), for the Au film in device SNS-2, using the measured electron-phonon interaction time and the book value electronic heat capacity scaled up by a factor of 50. The temperature dependence of such quantity is demonstrated in Fig.5.27. The best sensitivity we can get, at temperature above 50 mK, is $\sim 2 \times 10^{-19}$W/$\sqrt{Hz}$.

In brief, it is important, for the application of the phonon–cooled HEB, to fully understand the electron-phonon interaction in the actual absorber material with the actual device geometry, and at the operation temperature. When estimating the sensitivity of the device, the book value electronic heat capacity should be used with extra caution.

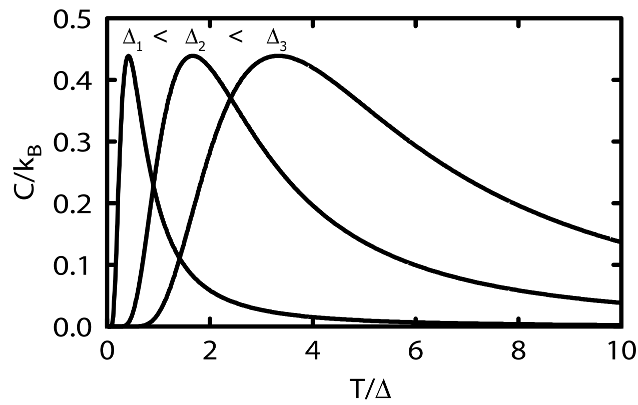

(a) The heat capacity induced by two level systems

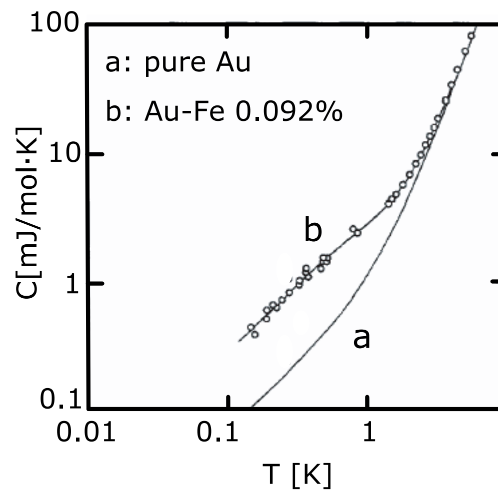

(b) The measurement of heat capacity for Au with $\sim 0.1\%$ magnetic (Fe) impurities. The figure is adopted from Chatenier & Miedema (1966), Fig.6.

Figure 5.21: The Schottky anomaly.

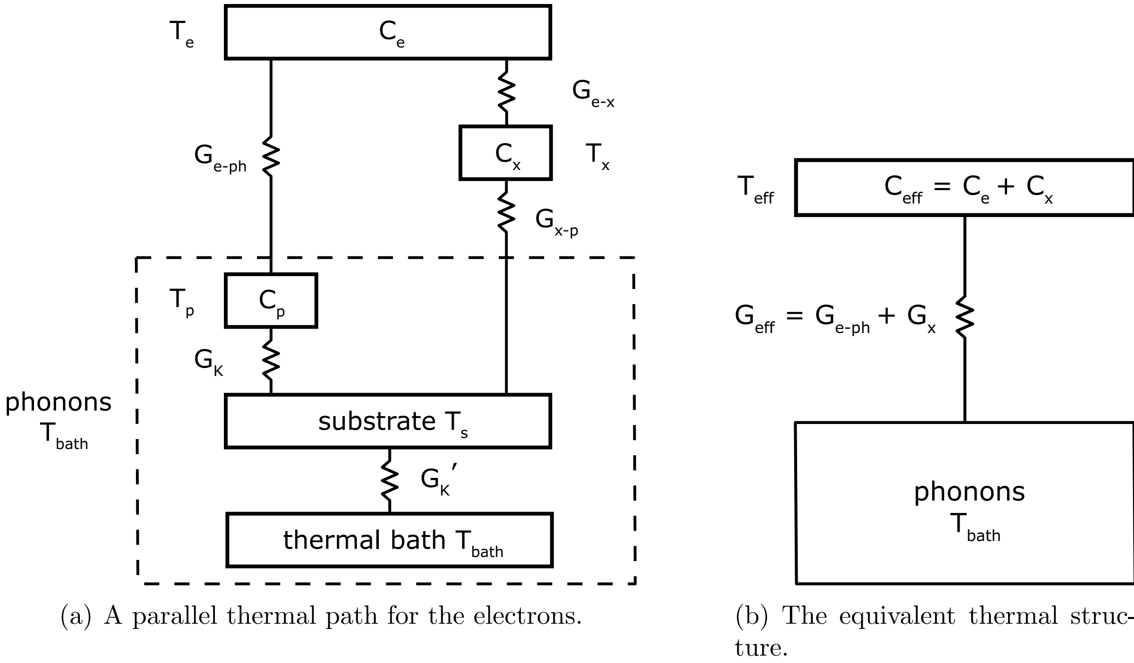

(a) A parallel thermal path for the electrons.

(b) The equivalent thermal structure.

Figure 5.22: Possible thermal structure that leads to large G_{e-ph} and C_e.

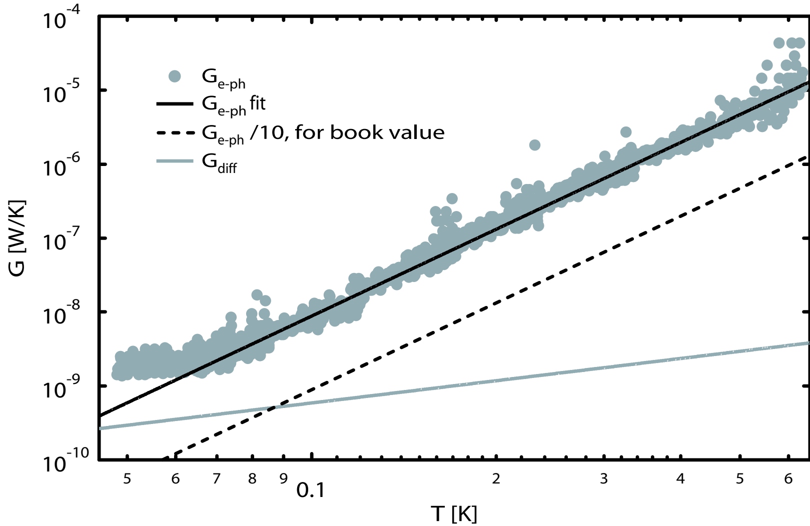

Figure 5.23: Comparison between G_{diff} and G_{e-ph} for device Diff-2.

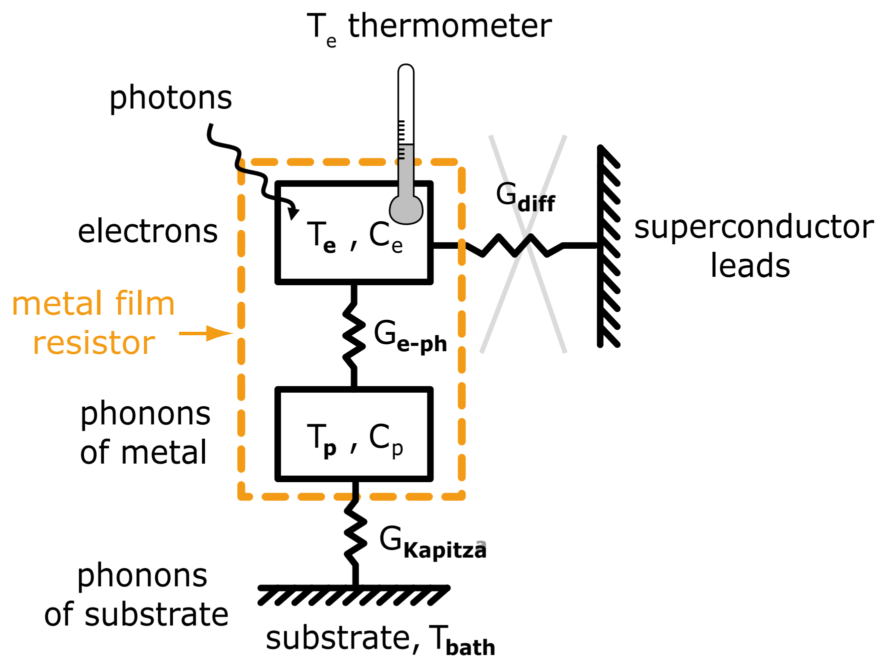

Figure 5.24: The thermal structure of the phonon cooled HEB.

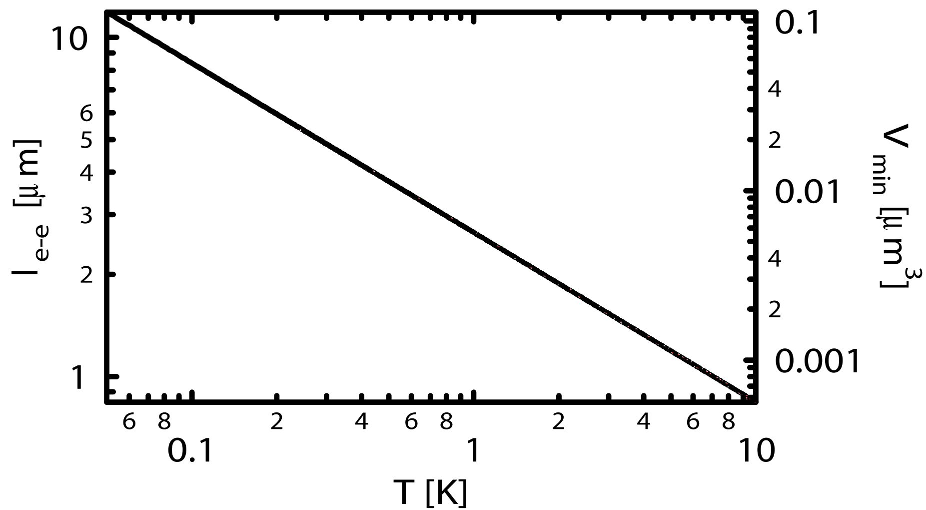

Figure 5.25: The minimal volume of the phonon cooled HEB absorber. Both quantities are functions of the operating temperature.

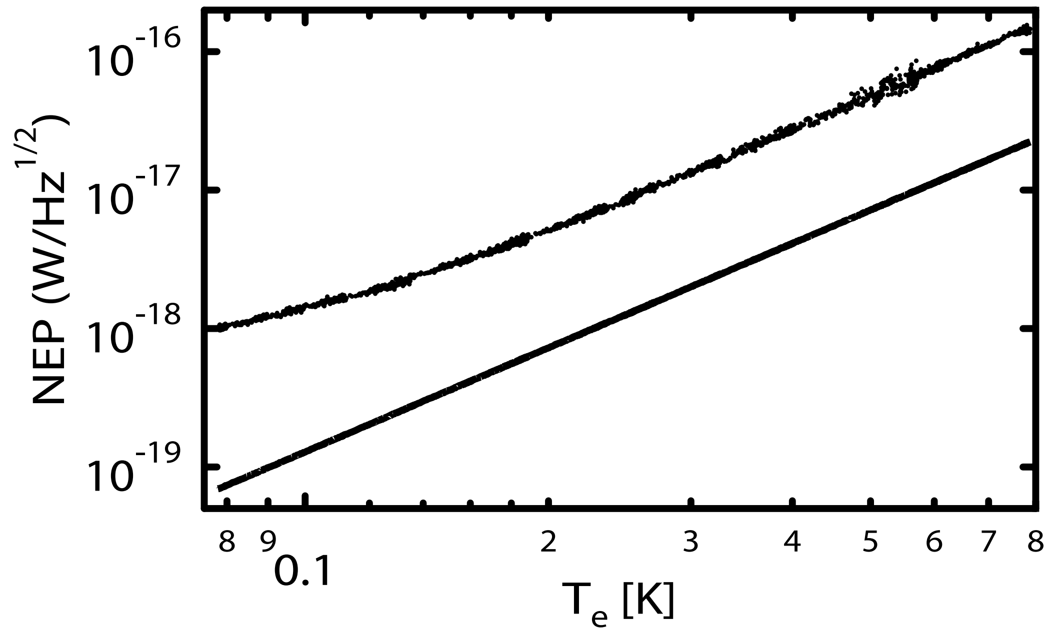

Figure 5.26: The NEP for an HEB with our Au thin film as the absorber
The NEP from our Au film are the dots, and the calculated NEP for an absorber with the book value electronic heat capacity is the solid line.

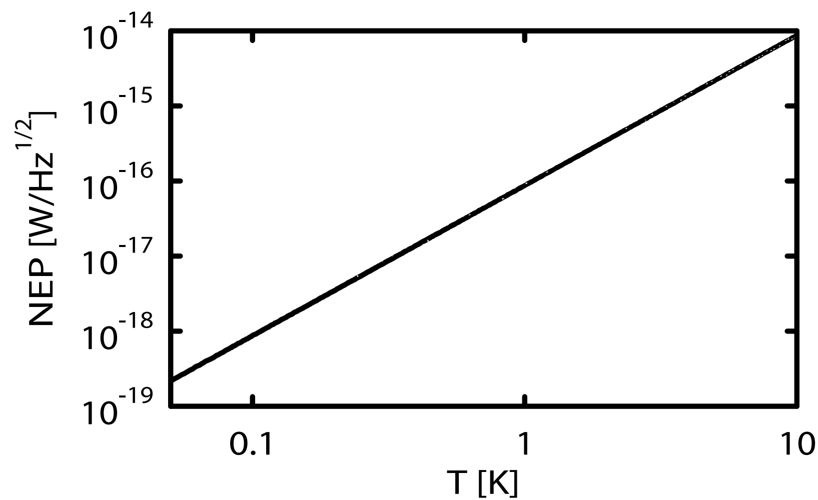

Figure 5.27: Ultimate sensitivity for our Au thin films as the phonon–cooled HEB.

Chapter 6

Designs for superconducting high frequency coplanar bandpass filter

The superconducting coplanar bandpass filter is a very important part of the photon detector on-chip calibration scheme. In this thesis work, we explore the designs of such filters at the desired calibration frequencies, 100–200 GHz. Due to the high frequency of the filters, the designing and testing process are rather complicated. In this chapter, we describe two possible designs for the coplanar bandpass filters.

6.1 On-chip calibration scheme

We have discussed the properties of phonon cooled hot electron photon sources in previous chapters. The sources are essentially metal thin film wires on insulating SiO_2/Si substrates. In order to utilize the source to calibrate a sub-millimeter detector, a proper calibration scheme is needed to couple the source and the detector. Since both the source and the detector are planar structures, it is desirable to integrate all components of the calibration scheme on to one single substrate. The calibration circuit can thus be fabricated by using standard micro-fabrication techniques. Also the coplanar structure avoids the complication of making vias to connect structures on both sides of the substrate. In this thesis, we refer to this coplanar scheme as the

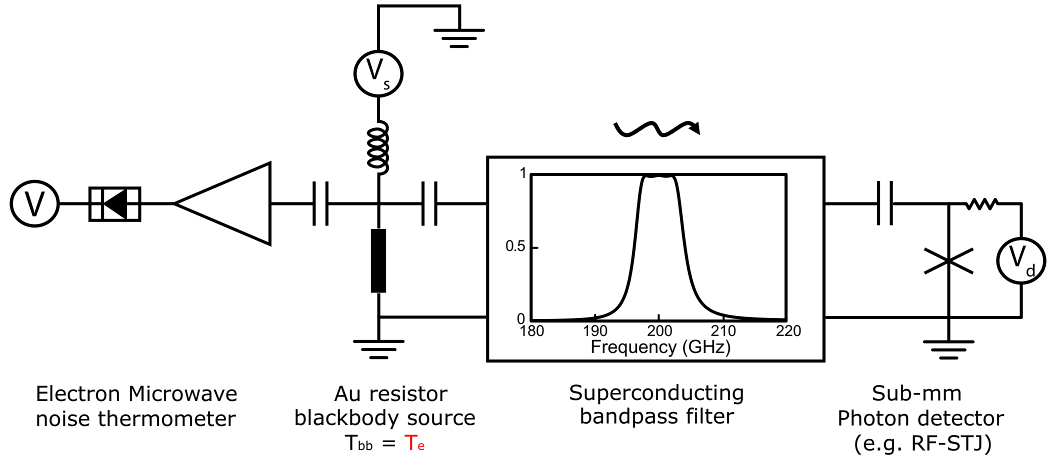

Figure 6.1: Block diagram of the on-chip photon calibration scheme. The hot electron photon source (left) and the STJ detector (right) are connected by a superconducting coplanar filter. The diagram also shows the bias and readout scheme of the source, and the bias of the detector.

on-chip photon detector calibration scheme. A block diagram of the scheme is given in Fig.6.1. The metal thin film photon source and the detector are connected by a coplanar superconducting bandpass filter. In this calibration scheme, the temperature of the photon source is measured simultaneously as it is transmitting photons to the detector. The electron thermometry—the dynamic microwave Johnson noise thermometry works in the Rayleigh-Jeans limit (∼1–2 GHz), while the source works in the Wien limit (∼ 100–200 GHz) for calibrating the detector.

The superconducting coplanar bandpass filter is a very crucial component in the calibration scheme. Besides selecting photons for the detector, it also provides electrical connection between the source and the detector. The filter consists of multiple sections of coupled transmission lines with characteristic impedance of 50Ω, which matches to that of the source, therefore photons transmitted from the source are not reflected by the filter. The filter is made of superconductor, which gives very much lower electrical loss than the best normal metal conductors. The filter also severs as

the superconductor lead for the source, so the length of the source metal film wire can be much shorter than the electron-phonon length, thus a very small volume. This implies that the electron-phonon heat conductance in the film is very small, and the sensitivity of the source is very high. The filter also forms DC isolation between the source and the detector, since both components need to be biased by DC source during operation, for example the electrons in the source are heated up by a voltage source V_s.

In the rest part of the chapter, we explore two possible designs for such filters, and their simulated frequency response.

6.2 Lumped element filter prototype

The designing of microwave filters usually starts from the designing of lumped element prototype; it is rather complicated to model the microwave component from scratch, while the theories for lumped element filters are well establish. After the prototype is designed, the lumped elements are replaced by proper microwave structures to form the microwave filters.

The basic building blocks of the bandpass filters are series LC circuits and parallel LC circuits shown in Fig.6.2(a) and (b) respective. A bandpass filter usually consists of a chain of these blocks in alternative orders, as illustrated in Fig.6.2(c), and the number of the blocks, N, is called the *order* of the filter. In general, the higher the order, the flatter the pass band, the sharper the cutoff at the band edges, but it comes with the price of more complicated circuits, and higher attenuation in the band. The order of the filter can be chosen according to the filter design requirements, such as the attenuation in the pass band, the cutoff in the stop band, and the bandwidth. For

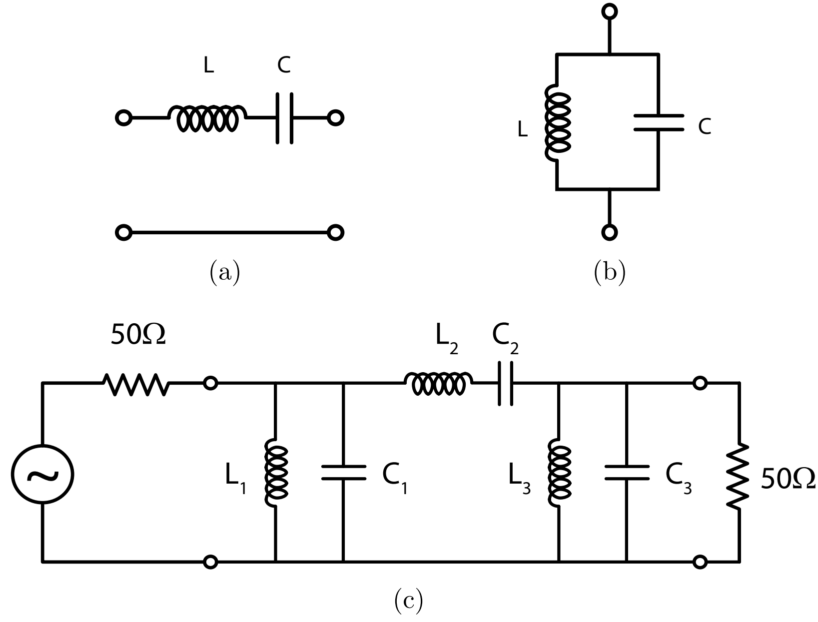

Figure 6.2: Lumped element model for bandpass filter.
(a)(b) Basic bandpass filter building blocks. (c) A bandpass filter of order 4 in driven by AC source with 50 Ω output impedance, and terminated by a 50 Ω load.

example in this thesis work, the center frequency of the filter is 200 GHz, and it is sufficient to have 10% bandwidth, less than -0.5dB attenuation in the pass band, and -20 dB attenuation at a bandwidth away from the center frequency. These requirements are satisfied with a filter with $N = 3$. In addition, equal-ripple (or Chebyshev) model (Pozar 1998) is used in our design. The filter has equal amplitude ripples in the pass band, and it is used to obtain sharp cutoff at the edges of the pass band. In Table 6.1 we list the values of the inductors and the capacitors of an $N = 3$ equal–ripple filter (Fig.6.2(c)), with 0.5 dB ripples, 200 GHz center frequency, and 10% bandwidth.

L_1	C_1	L_2	C_2	L_3	C_3
0.64 nH	1.0 fF	3.6 pH	0.17 pF	0.64 nH	1.0 fF

Table 6.1: The components of a 200 GHz equal–ripple bandpass filter.
The filter has 0.5 dB equal–ripple in the pass band, with $N = 3$ and 10% bandwidth.

6.3 The capacitively coupled CPW resonators bandpass filter

The lumped element design can be realized with capacitively coupled coplanar waveguide (CPW) resonators. This section covers the detailed physical layout of the filter, the integration of the filter to the source and detector, and the simulated frequency response.

6.3.1 Filter layout

CPW as suggested by its name is a coplanar transmission line, whose components are all on the same side of the substrate (Fig.6.3(a)). The two infinitely wide metal

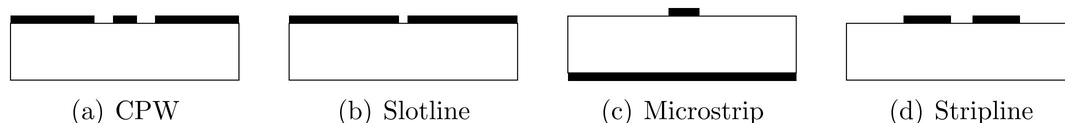

(a) CPW (b) Slotline (c) Microstrip (d) Stripline

Figure 6.3: Transmission lines.
The side views of three different flavors of transmission lines appeared in the thesis. (a) Coplanar waveguide (CPW), (b) slotline, (c) microstrip line, (d) coplanar stripline.

planes on the both sides of the center conductor pin are the side ground planes, and Quasi-TEM modes can propagate along the two gaps. The advantage of using the CPW is that all components of the calibration circuit can be on one side of the substrate, and no vias are needed to couple the source and the detector to the back ground plane (e.g. for microstrip).

A piece of lossless transmission line is equivalent to a LC resonator. If several CPW resonators are coupled together, the lumped element model in Fig.6.2(c) can be realized. In fact, it has been proven (Pozar 1998, See references within) that three

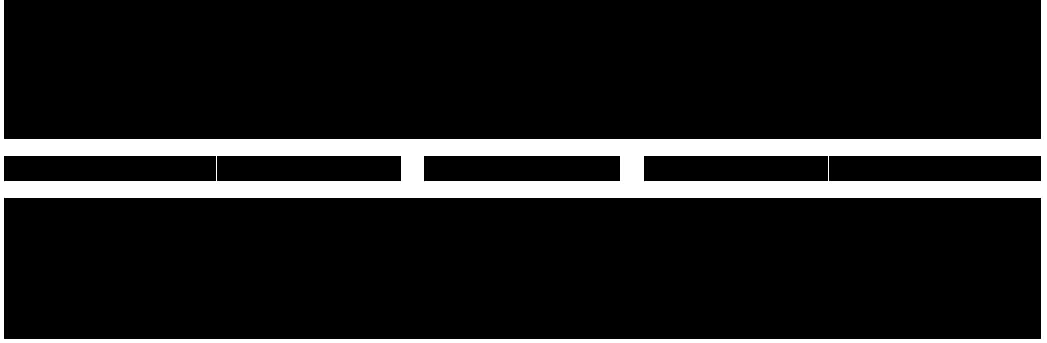

Figure 6.4: The physical layout of the capacitively coupled CPW resonators bandpass filter.

capacitively coupled CPW resonators of the proper lengths is equivalent to the circuit. The physical layout of the filter is given in Fig.6.4. The filter is on a 300 μm thick Si substrate (with dielectric constant $\epsilon_r = 11.9$), and the width of the center conductor pin is 10 μm and the gap between the center pin and the side ground planes is 7 μm. The filter design is targeted at 200 GHz working frequency. The filter consist of three CPW resonators (1,2 and 3 from left to right), and their electrical lengths and physical lengths are given in Table 6.2. The four gaps (1,2,3 and 4 from left

	1	2	3
Electrical length θ (°)	155.8	166.5	155.8
Physical length l (μm)	267	285	267

Table 6.2: Resonator lengths for 200 GHz bandpass filter
The electrical and physical lengths of the resonators are calculated based on the cross-sectional dimensions of the CPW line described above.

to right) along the center conductor pin are effectively capacitors, the gap widths and the corresponding effective capacitances as listed in Table 6.3. The width of the gap is decided by the desired capacitance, the larger the capacitance, the smaller the gap. Note that the 5.54 fF capacitors are very large, and the corresponding gap width is very small, which might cause difficulties in device fabrication. Alternatively,

	1	2	3	4
Gap width (μm)	0.5	3	3	0.5
Capacitance (fF)	5.49	1.93	1.93	5.49

Table 6.3: Capacitances of the coupling capacitors in 200 GHz CPW bandpass filter. The capacitance are simulated in Sonnet based on the dimensions of the structure.

interdigital fingers can be used to increase the coupling area with larger gap width, consequently increase the capacitance.

Limited by the equipments in our lab, we cannot directly measure the frequency response of this 200 GHz filter. Instead, the response of the filter is simulated in quasi-3D (3D planar) microwave simulators, such as Sonnet, Microwave Office from AWR, and Serenade from Ansoft. The software calculates the electromagnetic field distribution for a given layout, which consists multiple layers of planar structures, thus the name "quasi-3D" simulator. The simulation result of the 200 GHz filter is given in Fig.6.5. The filter has a center frequency ~195 GHz, a ~ 5% bandwidth,

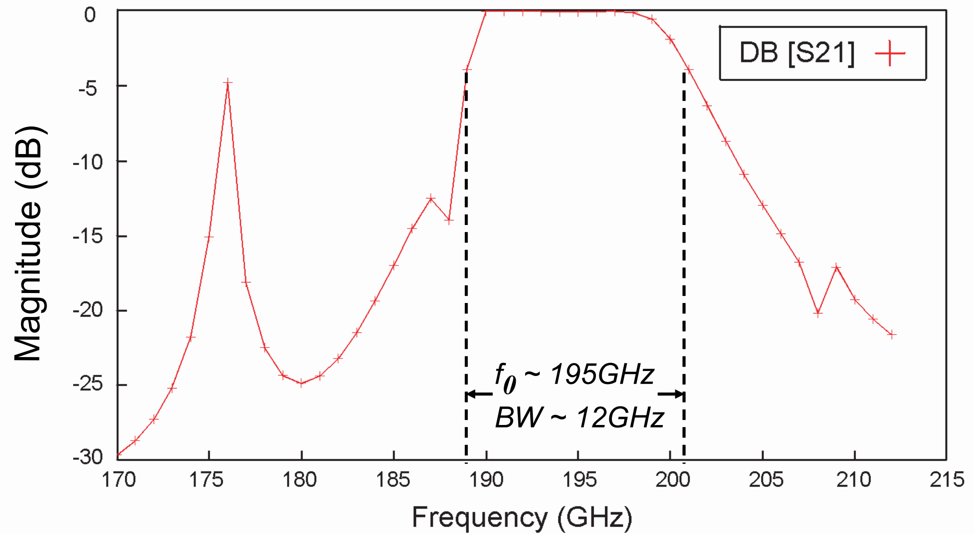

Figure 6.5: 200 GHz CPW bandpass filter simulation with Sonnet.

and less than 0.5 dB attenuation in the passband[1].

6.3.2 CPW–slotline balun

The CPW line is an unbalanced transmission line, but the photon source and the absorber of the photon detector both require balanced feed lines. Therefore output of the CPW filter have to be converted to a balanced transmission line — slotline. The slotline is essentially two infinitely wide conductor planes coupled at the side, and the electromagnetic field propagates along the gap between the two planes (Fig.6.3(b)). A CPW–slotline balun is needed between the two flavors of transmission lines (Simons 2001). Fig.6.6 demonstrates a layout of a broad band CPW–slotline balun. A quarter wave radial stub is opened in one of the CPW's side ground plane, which suppress electromagnetic field between the center pin and the upper ground plan near the end of the balun. The radial stub is chosen over a square stub to provide wider transition bandwidth. Also a thin gap is made at one side of the balun, the gap along 135° in Fig.6.6, to form DC block between the source and the detector. Air bridges (the grey lines) are needed to connect the two ground planes at the discontinuities to ensure equal potential. The balun itself is a very complex structure to simulate and to understand. The required air bridges make it even harder to approach technically; the size of the feature at the discontinuity is very small (the radius of the slot is about 100 μm at 200 GHz), it is very hard to make by using a simple wire bond. Instead, it would need to be make by using additional lithography steps. Therefore, the CPW bandpass filter might not be the best candidate for our calibration scheme.

[1] The peak at $\sim$ 175 GHz could come from the box resonance imposed by the simulation requirement.

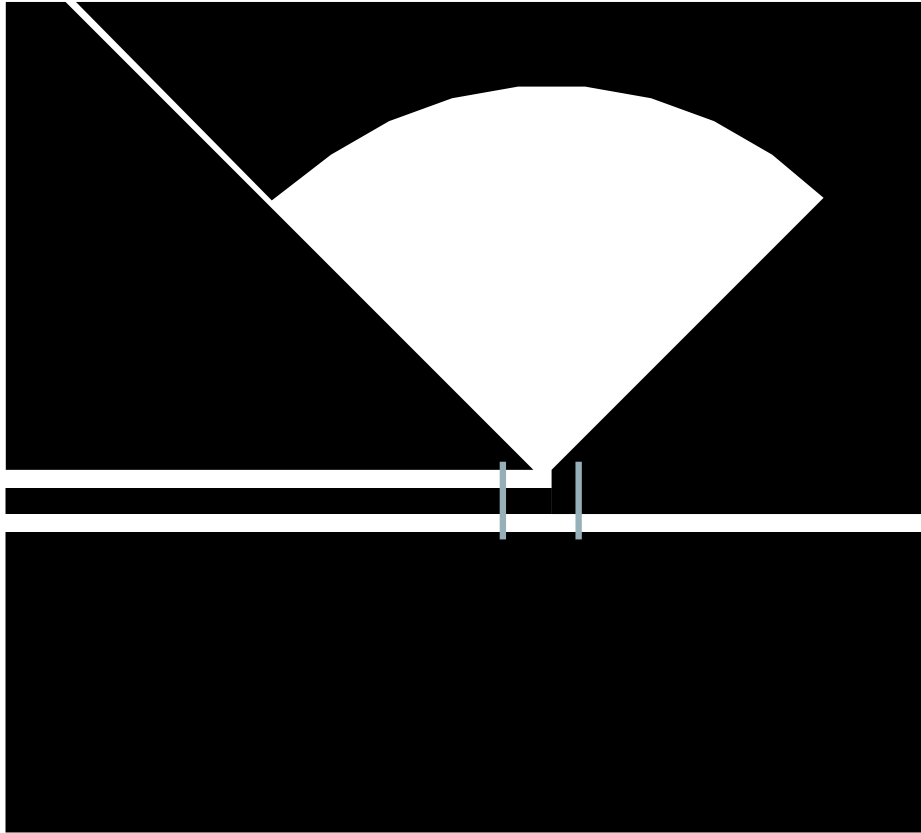

Figure 6.6: Broadband CPW–slotline balun.

6.4 The edge coupled microstrip bandpass filter

Another candidate for the coplanar bandpass filter is an edge coupled microstrip bandpass filter. The side view of a microstrip is given in Fig.6.3(c), it comprises a conductor on one side of the substrate, and a back ground plane on the other side. In this structure, we can avoid the complicated issue of designing the balun. In addition, since there is no side ground plane in the microstrip, the microstrip resonators can couple to one and another at the edge to increase the coupling capacitance. The filter also naturally provides DC block between the source and the detector.

6.4.1 Filter layout and simulated frequency response

A schematic layout of an edge coupled microstrip bandpass filter is shown in Fig.6.7. The filter is made of three edge coupled microstrip resonators, and it is equivalent

Figure 6.7: The schematic layout of an edge coupled microstrip bandpass filter.

to the lumped element prototype given in Fig.6.2(c). The frequency response of the filter is simulated in Microwave Office, shown in Fig.6.8. The passband is centered at 200 GHz, with bandwidth $\sim 10\%$. The attenuation in the passband is less than 0.3 dB.

Quarter wavelength radial stub DC ground

The microstrip is not a coplanar structure, its conductor pin and the ground plane are on different sides of the substrate. For low frequency applications, vias are often made to connect devices on the top side to the back ground plane. However, this is impractical for our 200 GHz filter; the width of the microstrip line is about 30 μm wide, it is very hard to make vias with simple single layer micro-fabrication techniques. Alternatively, we can place a "ground plane" on the top side of the substrate, by using a radial quarter wavelength stub, shown in Fig.6.9. The radius of the stub is a quarter wavelength at 200 GHz. The radial end of the stub is shorted to the ground, and the other end of the stub is transformed in to a RF open. Thus, at the left end of the

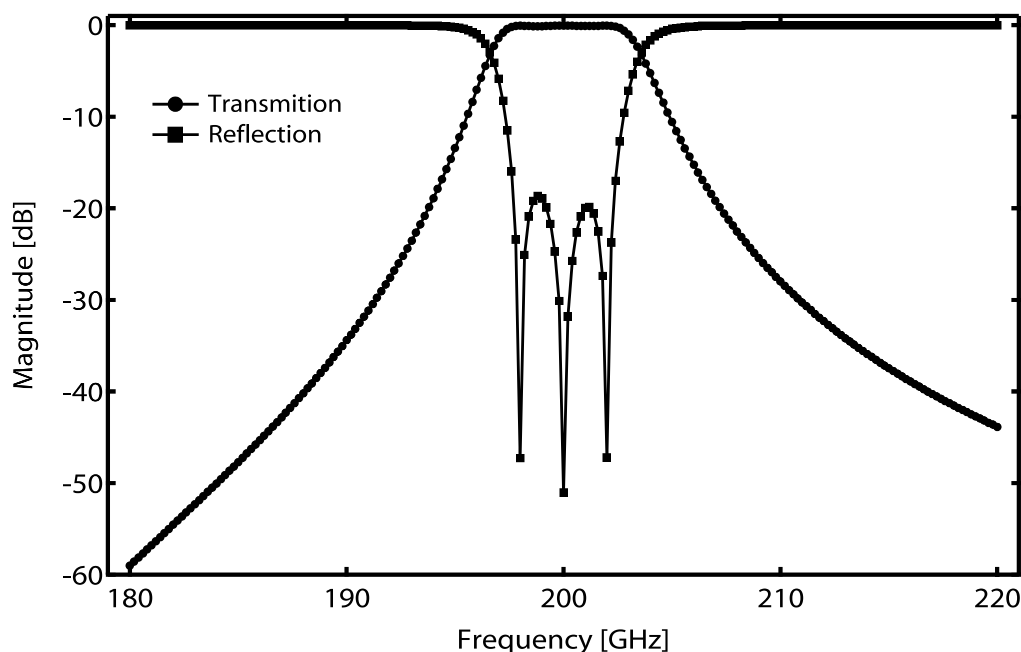

Figure 6.8: Frequency response of the 200 GHz microstrip bandpass filter. The simulation is done with Microwave Office.

source, the radial stub gives good RF ground, but it gives DC open for a wide range of frequencies centering at the quarter-wave frequency (200 GHz).

RF choke structures for DC bias

Another issue is how to DC bias the source and the detector. We can lose some of the photons generated by the source since they can also propagate into the DC bias lines. The solution is to use RF chokes to block the RF photons. The RF chokes are essentially stepped–impedance low pass filters. The physical layout and the equivalent lumped element circuit are illustrated in Fig.6.10. The thin wires are high impedance transmission lines and the wide wires are low impedance transmission lines. Intuitively, the high impedance part works as an inductor and the low impedance part works as a capacitor. They form the equivalent low pass filter circuit in Fig.6.10(b). When used as DC bias line, the RF choke allows the DC signal from the bias electronic

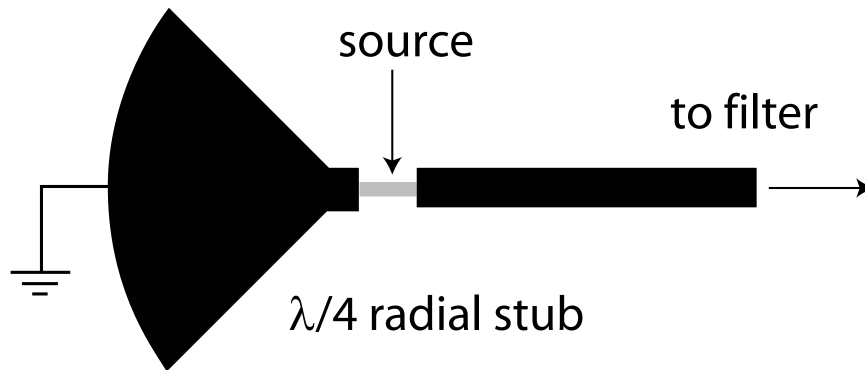

Figure 6.9: A quarter wavelength radial stub as RF ground.

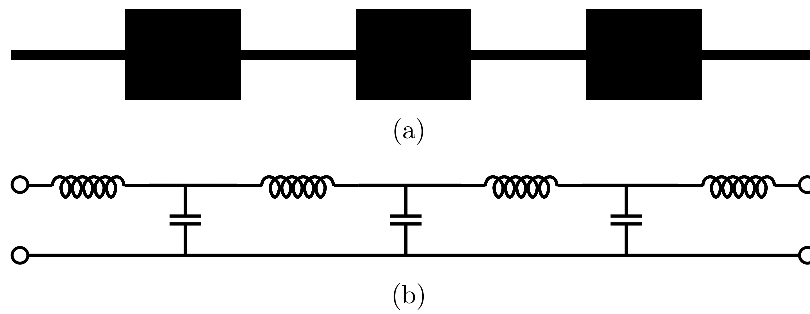

Figure 6.10: RF chokes for DC bias.
(a) The physical layout. (b) Equivalent lumped element circuit.

to pass through, and blocks the RF photons from entering the bias line. A schematic for DC biasing the source is shown in Fig.6.11.

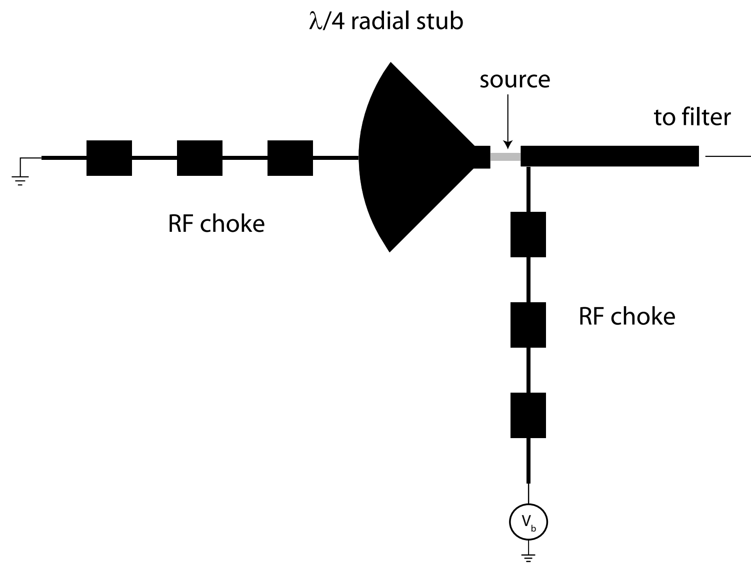

Figure 6.11: The DC bias scheme for the photon source.

Chapter 7

Fabrication of On-chip Calibration Integrated Circuit

Before the on-chip filter is fully developed, we have designed a simplified version of the on-chip calibration scheme for testing sub-mm detectors(Prober et al. 2004). In this chapter, I first briefly describe the device. In the second section, an overview of electron-beam (e-beam) lithography is given, followed by a detailed fabrication process of the on-chip calibration device based on the equipment available to us in the last section[1].

7.1 Integrated On-Chip Calibration Circuit Design

In this simplified version of on-chip calibration circuit, the coplanar filter is replaced by a transmission line of coplanar stripline structure, as illustrated in Fig.7.1 (Prober et al. 2004). The source is a Au microbridge with large thicker Au pads on both sides as conducting leads and also as part of the coplanar stripline (the left part in Fig.7.1(a)). The rest part of the coplanar stripline is made of Nb. Capacitors are made

[1]The fabrication process was first designed by C. Wilson and L. Frunzio. The process presented here is an improved version of the original design

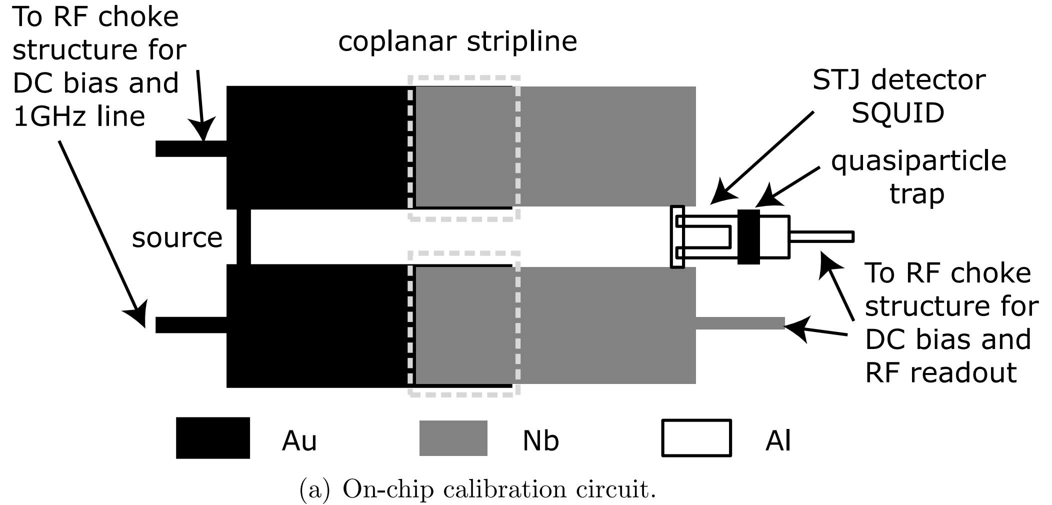

(a) On-chip calibration circuit.

(b) Equivalent circuit

Figure 7.1: Schematic of the simplified on-chip calibration circuit. (a) The schematic block diagram of the circuit. (b) The equivalent lumped element circuit.

at the overlap of the Au and Nb coplanar striplines to provide DC block between the source and the detector, and are is indicated in the dashed-line rectangles. The Au and Nb plates serve as the two conductor plates of the capacitor and the thin SiO_x film sandwiched between the plates is the dielectric. The superconducting tunnel junction (STJ) detector is a superconducting quantum interference device (SQUID)[2] with two $Al/Al_2O_3/Al$ superconductor-insulator-superconductor (SIS) junctions in parallel, and the absorbor Al strip connected to the Nb stripline. RF choke structures are connected to the DC and 1 GHz microwave noise readout line of the Au source

[2]In the original design by C. Wilson and L. Frunzio the STJ detector is a single $Al/Al_2O_3/Al$ junction.

at places indicated by the horizontal wires on the figure. Similarly, the DC bias and RF readout of the STJ are also connected through RF chocks.

The Au source is designed to have very small volume $0.5\,\mu m \times 0.1\,\mu m \times 0.01\,\mu m$, so that the amount of power needed to heat the electron gas in the film is very small. The small volume of the source also minimizes the hot phonons ($E_{phonon} > E_{gap}$ of Al) in the substrate. Such phonons, if propagate to the Al absorber, could break Cooper pairs in the Al film, creating the same effect as photons being detected. Due to the very small contact area of the source and the substrate ($0.05\,\mu m^2$), the Kapitza heat conductance between the film and the substrate is very small. Hence, the number of phonon excitations that can transfer into the substrate from the film is very small. Moreover, the thick normal Au contacts allow the hot electrons in the Au to be quickly cooled by diffusing into the contacts before they emit hot phonons. For the unavoidable small number of hot phonons in the substrate, there are normal metal cooling fins placed on the substrate to help absorbing the hot phonons and thermalize them to lower temperatures. Also large thermal Au pads deposited on the corners of the substrate, and wire-bonded to the sample holder with Au wires, cool the whole chip very efficiently to the bath temperature. Finally, the distance between the source and the detector is so large ($\sim 30\ \mu m$) that the phonons are largely attenuated ($> 10^2$).

The coplanar stripline has a characteristic impedance of $\sim 50\ \Omega$, that matches to the Au source resistance $\sim 50\ \Omega$. Therefore the source together with the stripline forms a one-dimensional blackbody radiator as described in Chapter 2. The coplanar stripline is essentially a pair of coupled microstrip lines that are very close to each other; the distance between the two conductor strips is much smaller than that between the conductor plates and bottom of the substrate which is in close contact with

the back ground plane – the Cu sample holder (Fig. 7.2.). Thus the electromagnetic

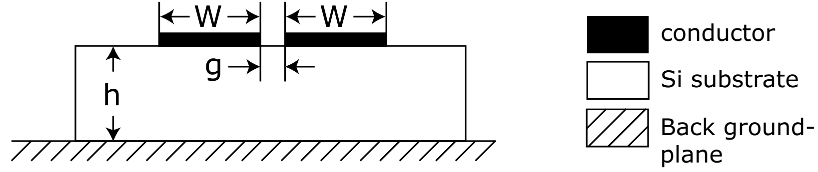

Figure 7.2: Cross-section of a coplanar stripline.
The two conductor lines are of same width W, g is the gap width between the lines, and h is the thickness of the substrate.

field concentrates at the gap between the coupled lines; the microwave propagates along the gap, and the back ground plane is no long relevant. The characteristic impedance of the coplanar stripline can be calculated by using W, g, and h for perfect conductor and lossless substrate (Simons 2001). In our sample, the dimensions of the stripline are W = 30 μm, g = 3 μm, and h = 381 μm (for standard single side polished 2″ Si wafer). A more realistic value can be obtained by using the TXline Transmission Line Calculator from Applied Wave Research, inc., which also takes into account the loss of the substrate and the finite conductivity of the conductors.

The Al absorber of the detector also has the resistance of $\sim 50\ \Omega$, such that the arrived blackbody radiation can be completely absorbed. The SQUID structure helps suppressing the Josephson current in the junctions with magnetic field threading through the SQUID loop. As a result, the detector could have lower dark current, hence higher sensitivity.

7.2 Fabrication Process Overview

The devices we are interested are planar structures with submicron features. In order to fabricate such small features, we use electron-beam (e-beam) lithography. A typical Si based e-beam lithography fabrication process used in our research is

given in Fig.7.3.[3] A brief description for each step is given in the rest of this section.

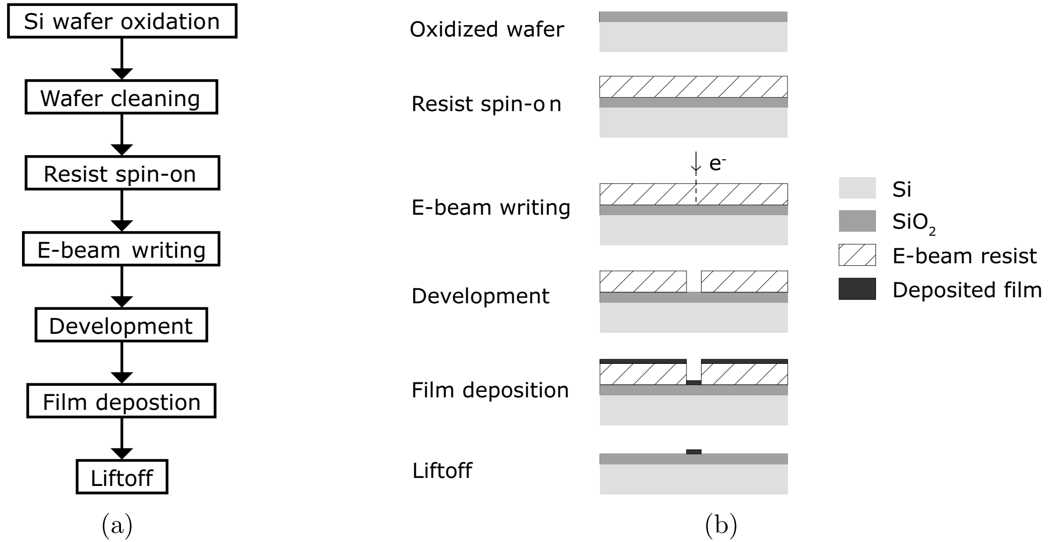

Figure 7.3: Steps of e-beam lithography process.

An equipment-specific and process-specific discussion of the fabrication process and parameters for the on-chip calibration circuit are given in the next section.

7.2.1 Wafer Oxidation

The wafers we used in our device are (100) single crystal Si wafers. They are essentially mechanical supports for the devices. In order to provide better electrical insulation, a thin layer of SiO_2 is thermally grown on the surface of the Si wafer by steam oxidation; water steam is applied to a hot furnace ($\sim$ 1000°), where the Si wafers are oxidized through

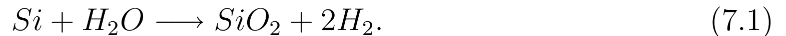

$$Si + H_2O \longrightarrow SiO_2 + 2H_2. \tag{7.1}$$

[3]The fabrication process we used here are compatible with the standard semiconductor microfabrication process. Details can be found in most microfabrication books (Jaeger 1993, Madou 2002).

7.2.2 Resist Process

Before the e-beam resist is spun onto the oxidized Si wafer, the wafer needs to be cleaned very carefully to remove particle contaminations and organic contaminations on the surface. This is usually done by rinsing the wafer in organic solvent with ultrasonic agitation.

The e-beam resists are chemicals that are sensitive to electrons. When exposed to electrons, the bonds of the long polymer chains in the resist are broken, so that the exposed resist dissolves in the developer much faster than the unexposed part[4]. The resist usually comes in liquid solution form and is applied to the wafer which is held on a vacuum chuck, and then spun at high speed (several thousand rpm) for about 60 seconds to produce a uniform layer over the whole wafer, and to get rid of the excessive resist. The thickness of the resist depends on the viscosity of the resist and the spinning speed (the resist manufacture usually provides spin curves for costumers' reference).

The typical e-beam resists are PMMA (polymethyl methacrylate) positive resist in anisole and MMA (copolymer) resist in ethyl lactate from Microchem. The standard Microchem PMMA includes 495,000 and 950,000 molecular weights (MW) in a wide range of concentration in anisole solvent. For example, the " 950PMMA A8 " resist is 8% solution of 950,000 MW PMMA in anisole solvent. In general, the higher the MW, the slower the resist dissolves in the developer, and the higher the resolution of the resist. The solid concentration of the PMMA affects the thickness of the spun resist layer on the wafer, that is, at a fixed spinning speed, the higher the concentration, the larger the thickness of the resist.

The MMA resist is a mixture of PMMA and methacrylic acid in ethyl lactate

[4]This is for positive resist. For negative e-beam resist, the exposed part is harder to dissolve.

solvent. For instance, " MMA(8.5) EL15 " resist is a 15% solution of PMMA with 8.5% methacrylic acid in ethyl lactate solvent. The addition of the methacrylic acid gives the MMA a higher dissolution rate than PMMA in developers. Therefore, the MMA can be used as a " sacrificial " bottom layer in an MMA/PMMA double layer resist, so that a large controllable resist undercut can form below the PMMA layer, as shown in the following schematic (Fig.7.4).

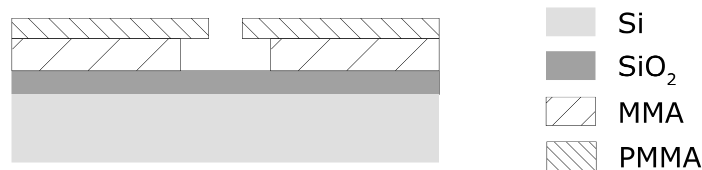

Figure 7.4: MMA/PMMA double layer e-beam resist with controlled MMA undercut.

7.2.3 E-beam Lithography

E-beam lithography is a process to transfer patterns of very small planar structures (down to $\sim$ 50nm) to the e-beam resist. The following description of the e-beam lithography process is based on our FEI XL30 Sirion high-resolution scanning electron microscope (SEM) equipped with a Scanservice High Speed Beam Blanker and J.C. Nabity Nanometer Pattern Lithography System (NPGS). For more systematic instruction on micro/nona fabrication using e-beam lithography please refer to (Nabity n.d., Rooks 1987, Rai-Choudhury 1997).

E-beam Lithography with FEI SEM

The electron beam of the FEI XL30 Siron SEM is generated by the field emission filament in the gun chamber and accelerated by a high voltage (30 KV for lithography purpose). The beam is then confined and focused by several apertures and lenses along the SEM column. Finally a focused beam of certain spot size comes out from

the SEM tip and arrives at the sample sitting in the sample chamber. In the FEI SEM, there are seven spot sizes for the focused beam, labeled from 1 to 7; the larger the number for the spot size, the larger the size of the beam area, the higher the beam current, the lower the resolution of the writing. In addition, a high speed beam blanker is installed below the electron gun. The blanker can be turn on and off very fast to block and unblock the beam when needed.

The focused beam can be deflected by coils in the SEM column to a certain extend to scan across the wafer. For a given working distance (WD), which is the distance between the tip and the substrate when the beam is focused, the maximum area the beam can reach on the substrate (the writing field of the beam) by deflection is fixed, and the area scale inversely with the microscope magnification. The writing field of our SEM extends 187 μm in both x and y directions at 1000 magnification at 10 mm WD. The critical small structures ($< 1\ \mu m$) are usually written at the smallest spot size (spot size 1) and high magnification ($\sim \times 1000$). The intermediate structures ($> 1\ \mu m$) are written with a slightly larger spot size (spot size 4). And the large contact pads are written with the largest spot size (spot size 7) at low magnifications ($\sim \times 100$) to reduce the writing time. The corresponding beam currents for these spot sizes are approximately

Spot size	1	4	7
Beam current (pA)	23.5	530	70,000

Table 7.1: Beam currents for different spot sizes of FEI XL30 SEM.

During actual writing, the beam is controlled externally by the NPGS program installed on a computer connected to the SEM. The program reads the patterns designed in a CAD program and raster-scans the beam on the resist accordingly. The program also controls the beam blanker; the blanker is off during most time of

writing, but it is turned on during the time the beam is moving between two entities, in order to prevent unwanted connections between the entities.

Nabity Nanometer Pattern Lithography System (NPGS)

The NPGS by Nabity (n.d.) is a pattern generation program that reads the design of the device and controls the electron beam of the SEM to " write "(expose) the resist with designed exposure parameters.

The device is designed in the DesignCAD software embedded in the NPGS. The entities in the design have different exposure parameters according to their dimensions. Such parameters include: microscope magnification, beam spot size (or beam current), exposure dose, line spacing, center-to-center distance. The first two has been discussed above. The exposure dose is the amount of charge deposited in to the resist for certain unit dimension. In our application, we refer to the dose as area dose in $\mu C/cm^2$. The beam expose the resist point by point while writing. The line spacing is the distance between two adjacent raster lines and the center-to-center distance is the distance between the centers of two adjacent points within a line. These two parameters are usually set to be the same, and together with the dose decide the exposure point size. While designing the device in DesignCAD, entities of different materials and exposure parameters are assigned into different layers and colors.

For very demanding lithography, the direction of the raster sweep within a given entity and the order of the entities being written within a layer are very important. During writing, at the ends of each raster line, the beam makes a sudden stop and turns in the opposite direction (serpentine scan). Thus the sides that are perpendicular to the raster lines tend to be rougher than those along the lines. One needs to set the sweep side (the side where the writing will start and is parallel with the raster lines) of each entity according to the design requirement. For instance, the

sweep side of a long wire should be set at one of the longitudinal side. In most of the writing layers, there are more than one entity. After finishing writing one entity, the beam quickly jumps to the starting point of the next entity and starts writing immediately. However, the beam tends to become unstable after the jump, and the larger the distance the beam travels, the more unstable it becomes. Therefore, the entities should be put into the optimal order such that the distance between the end point of an entity and the starting point of the next entity is minimized.[5]

Often time, a device requires multiple layers of e-beam lithography and the patterns of different layers need to align to each other. NPGS provides a program " AL " to align different lithography layers by using pre-deposited alignment marks without exposing the writing area. An example is given in Fig. 7.5. When the AL

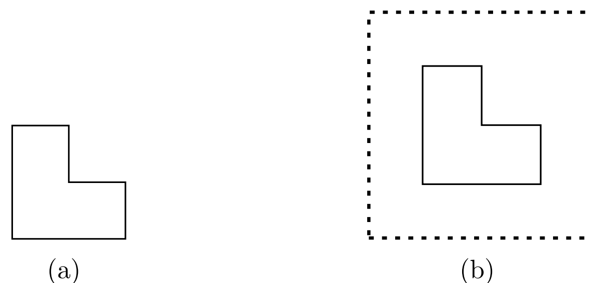

Figure 7.5: Patterns for e-beam lithography alignment.
(a) Alignment mark. (b) Alignment window (dashed line) with overlay (solid line). The overlay can be moved manually within the window to align to the alignment mark.

program is called, the e-beam scans the alignment window. Once the alignment mark is found in the window, one moves the overlay in the window to align with the mark. The program records the finial displacement of the overlay from its original position, calculates and moves the beam to the correct aligned position. There could be multiple windows for each set of alignment step. The size of the window determines the

[5]An other way to solve such problem is to put a " dump point " close to the starting point of an entity (Nabity n.d.). The beam sits at the dump point and stabilizes before it starts writing again.

accuracy of the alignment; the larger the alignment windows, the coarser the alignment. But it is very hard to begin the alignment with finding the alignment marks in very small windows. Thus, for very fine alignment, we can start with a set of large alignment windows to coarsely adjust the position of the beam, so that it is easier to find the fine alignment marks in the set of smaller alignment windows.

Once the device is designed, the patterns are loaded into a " run file ", where the exposure parameters are assigned to the entities with different design colors and layers. The run file can load multiple designs and alignment patterns as well. During writing, the NPGS program reads the patterns in the order they are listed in the file and their exposure parameters, and calls the PG program to control the SEM writing accordingly. If alignment patterns are in the run file, the NPGS loads the AL program to perform the alignment before writing the actual patterns.

Proximity Effect

When the electron beam impinges on the resist, the electrons experience complicated scattering process, and also create secondary electrons (Rai-Choudhury 1997). These cause a water drop shape electron profile in the resist, as illustrated in Fig.7.6(a), so

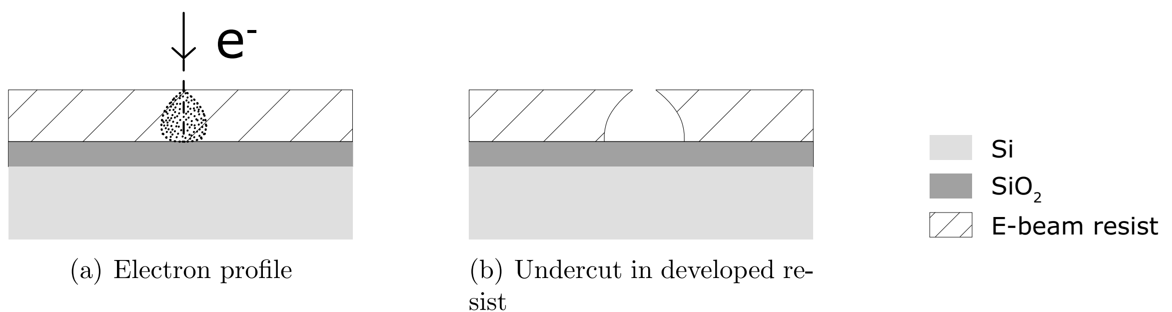

(a) Electron profile

(b) Undercut in developed resist

Figure 7.6: The proximity effect in e-beam lithography.
(a) The electron profile in the resist during the e-beam exposure. (b) The undercut resist after development.

that the actual area of the resist being exposed is larger than the initial beam size

up to a factor of 10, and an undercut is form in the developed resist (Fig.7.6(b)). Therefore, the beam not only exposes the resist along the path of the scan, it also exposes the area around the path. This is call the proximity effect. It limits the smallest line-width that can be written. Therefore the design of patterns located very close to each other should take into account the proximity effect.

7.2.4 Development

After the e-beam resist is exposed, molecular chain scission occurs in the exposed resist. As a result, there is a very high contrast of dissolution in the developer between the exposed and unexposed regions of the resist, i.e. when the exposed resist is completely dissolved by the developer, the unexposed resist still covers the Si wafer underneath.

The MMA/PMMA developers are blends of methyl isobutyl ketone (MIBK) and isopropanol (IPA), where MIBK is the active developer solvent, and IPA is the non-solvent that dilutes MIBK to control the speed of the resist dissolution. In general, the developer with higher amounts of IPA is less aggressive, and produces higher resolution structures in the resist. We use 1:3 MIBK to IPA as our developer for fabricating sub-micron devices.

7.2.5 Film deposition

The designed device patterns are now transferred to the resist. The surface of the Si wafer is cover by the resist mask, except for places where the patterns are supposed to be. The desired material is then deposited to the whole wafer, but only sticks to the Si at the resist windows, the rest resides on top of the resist and is washed away during liftoff. Electron-beam (e-beam) evaporation and sputtering are used in our processes for deposition of Au, Al, SiO_x and Nb thin films.

E-beam evaporation

E-beam evaporation is a form of physical evaporation deposition (PVD). PVD is the process of heating the source material to the point of vaporization, transporting the material vapor to the sample substrate where the vapor condenses to form a thin film. It is usually used for deposition of materials with relatively low melting point, e.g. Au, Al, Ti, Cu. During e-beam evaporation, the source material is put in a high temperature crucible (graphite crucible), a high-intensity electron-beam with an energy $\sim$ 20 KeV is focused onto the source to melt the material locally. The deposition is performed in vacuum chamber to avoid contamination and to control the composition of the deposited film. The low pressure in the chamber enables the material gas molecules to have very long mean free path (on the order of 1 m, which is longer than the source-substrate distance). Therefore, the evaporation deposition is directional; shadows of the resist patterns can be transferred to the substrate. This phenomenon is the basis for making superconductor-insulator-superconductor (SIS) junctions by **double angle evaporation**. Fig. 7.7 illustrates the typical process for making $Al/Al_2O_3/Al$ junctions with the method. An MMA/PMMA double layer e-beam resist is used to produce controllable large undercut ($\sim$ 3-5 μm). The pattern of the SIS junction consists of strips that are perpendicular to each other. At the spot where the two strips are closest ($\sim$ 1 μm), due to the large undercut in the resist, a suspended resist bridge occurs, as indicated in Fig.7.7(a) in the dotted line. In the first evaporation layer, the Al is evaporated perpendicular to the substrate, so that the resulted two Al strips are separated from each other (Fig.7.7(b)). After the sample cools down, low pressure dry O_2 is injected into the vacuum chamber to oxidized the Al at room temperature for a certain amount of time. The chamber is then pumped back to the desired vacuum level for the second evaporation, which

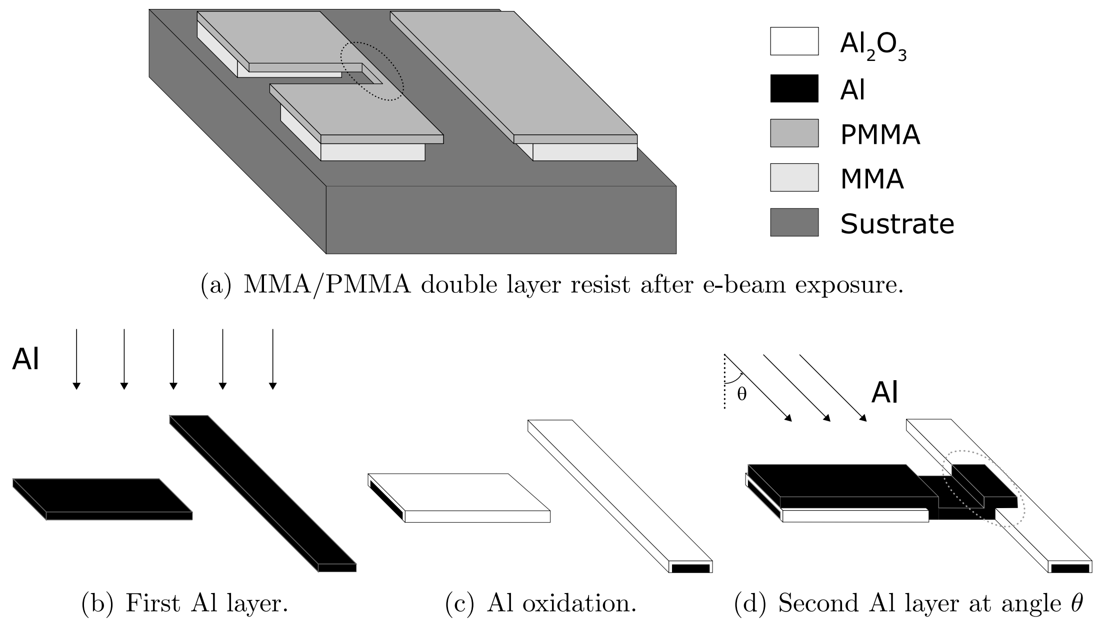

(a) MMA/PMMA double layer resist after e-beam exposure.

(b) First Al layer. (c) Al oxidation. (d) Second Al layer at angle θ

Figure 7.7: Schematic of double angle evaporation.
The scheme is used for fabricating $Al/Al_2O_3/Al$ SIS junctions.

is done at an angle θ with respect to the first deposition direction. Thus the Al deposited on the sample is shifted by $\Delta x = t \tan\theta$ relative to the first deposition layer, t being the thickness of the resist, and the material molecules can access the area under the suspended resist bridge. As a result, the second layer of the horizontal line falls on top of the the first layer of the vertical line, and an $Al/Al_2O_3/Al$ junction is formed at the overlap (indicated in the dashed line in Fig.7.7(d)). The second layer of the vertical line is shifted away from the structure and falls on the vertical resist wall which is washed away during liftoff.

DC Sputtering

However, e-beam evaporation is not suitable for materials with very high melting point, such as Nb and Ta. The amount of heat needed to melt such materials could melt the crucible and damage the resist on the wafer such that contaminations are introduced into the deposited film, or the system simply cannot produce high enough

power to melt the source material. For deposition of these films, we need to introduce the sputtering process. Sputtering is a physical process where the atoms of the solid source target are knocked out from the surface due to the bombardment of chemically inert energetic ions (e.g. Ar^+), and condensed on the sample substrate. The Ar^+ ions are supplied by a plasma generated by the system between the target and the substrate; low pressure Ar gas is filled in to the vacuum chamber of the sputtering machine, and a high voltage is applied to ionize the gas to generative a fluid of positive ions and electrons in a quasi-neutral electrical state. The ions are then accelerated towards the target (cathode) by high DC voltage.

7.2.6 Lift off

After deposition, the whole wafer is covered with the deposited material. The unwanted films are stripped off by soaking the sample in appropriate solvent, which dissolves the remaining resist on the substrate, and washes away the films on top.

7.3 Fabrication of On-chip Calibration Device

7.3.1 Device layout

The actual physical layout of the on-chip calibration device is given in Fig.7.8. The large Nb pads are bonding/contact pads. They are connected to the fine structures (patterns circled in the dashed line) through thin Nb wires which are essentially low pass lines. The Au "L" shapes patterns are alignment marks, with the outer set of the four large marks for coarse alignment to $\sim 5\,\mu m$, and the inner set of intermediate marks for alignment as good as $1\,\mu m$. The Au rectangular strip overlapping with the Al structures is the Au quasi-particle trap. The large Au bar at the bottom of

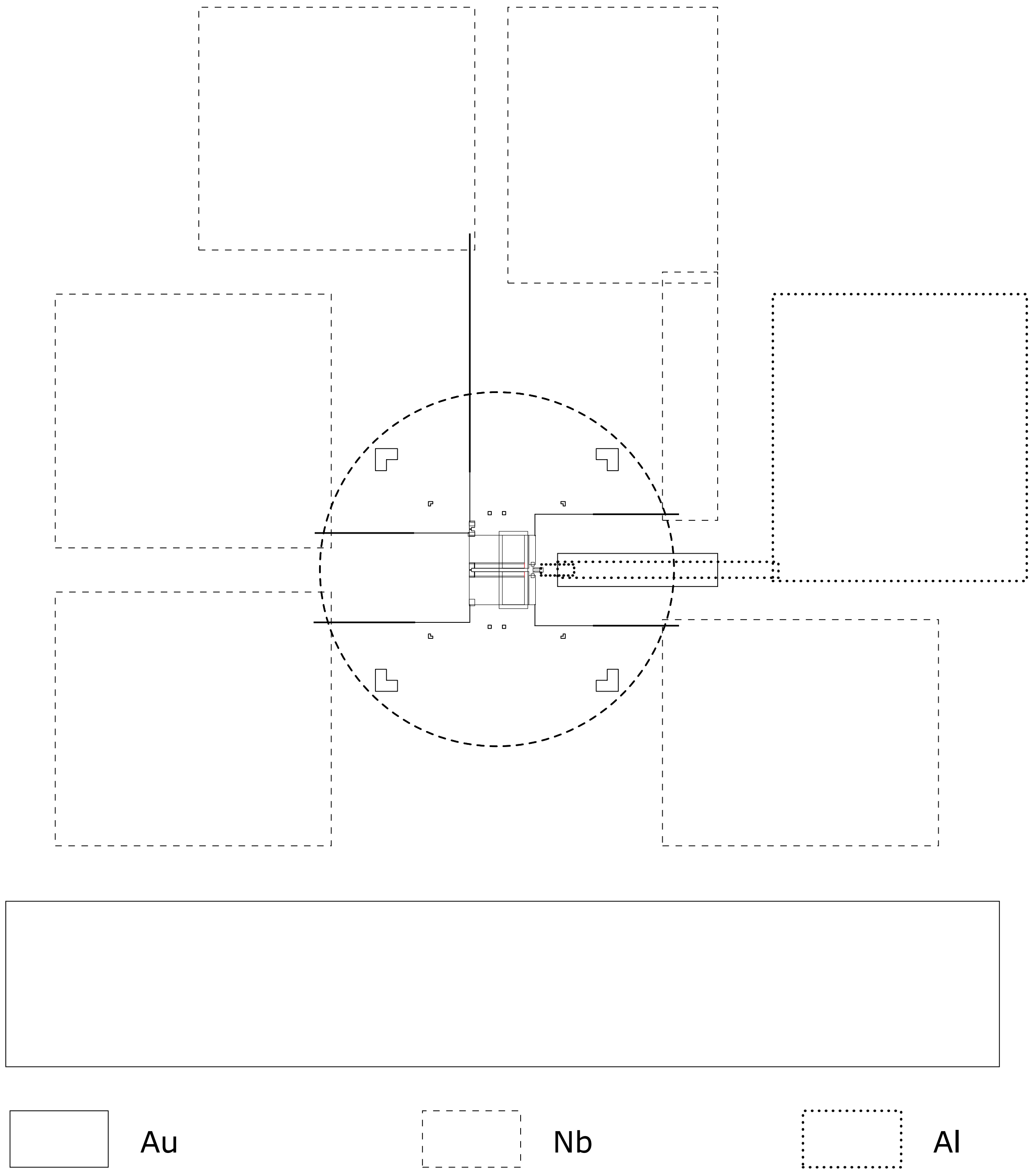

Figure 7.8: On-chip calibration device layout at microscope magnification of 150. The structures in the dashed circle are fine features of the device written at magnification of 1200.

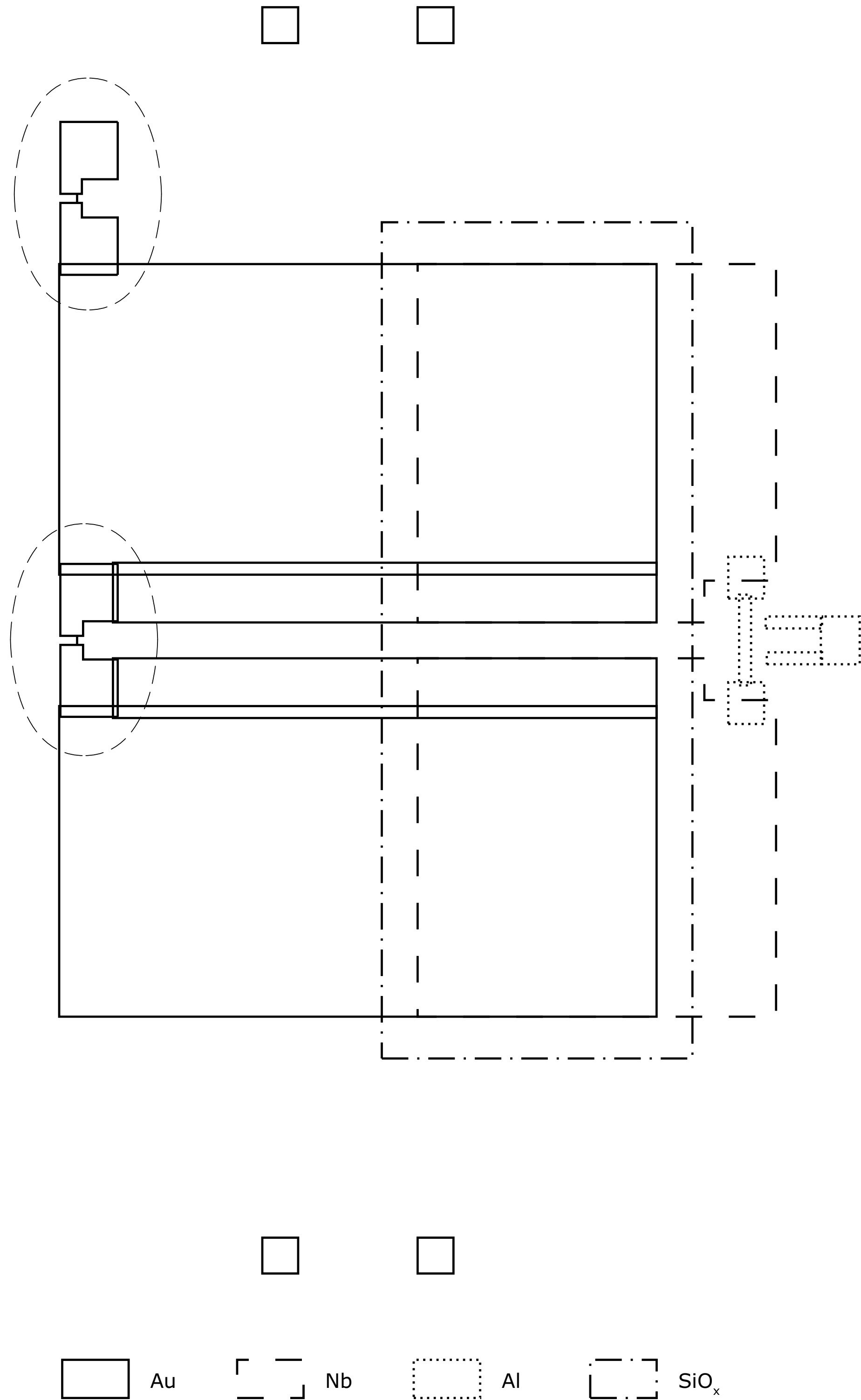

Figure 7.9: Zoom-in on the source-stripline-detector structure.
The contact pads and wirings are not shown. The patterns in the dashed ovals are Au microbridge sources.

the device is the “ cooling fin ” described in the previous section. The STJ detector, shown on the right, has an Al strip extending over the Au trap, and connected to the Al contact pad.

A zoom-in layout for the fine structures, i.e. the source-stripline-detector, is given in Fig.7.9. The device consists of four layers of materials – Au, SiO_x, Al, and Nb. The Au layer includes fine alignment marks (the four small square at the top and the bottom of the figure, and can be used for alignment as good as 0.25 *mu*m), coplanar stripline, and two microbridge sources (shown in the dashed line ovals). The bottom source is the real source that is electrically connected to the detector to supply photons. The source at the top is a “ blind ” source, which is electrically isolated from but thermally connected to the detector; the source does not transmit photons to the detector, but when heated by Joule power, it can emit hot phonons into the substrate to break pairs in the detector absorber. With the “ blind ” source, we can test the effect of phonon heating on the detector. The SiO_x is shown as the dotted-dashed rectangle overlapping the Au and Nb stripline, which is indicated by the dashed line polygons. The dotted line patterns are the Al SQUID for STJ detectors.

The fabrication has four layers of electron-beam lithography and film deposition. Each layer involves the following steps: e-beam resist spin-on, e-beam writing/exposure, resist development, material deposition, resist liftoff. In what follows, I give the detail steps and parameters specifically for the on-chip calibration circuit fabrication.

7.3.2 Wafer Oxidation

Before the actual fabrication takes place on the wafer, a thin layer of SiO_2 is thermally grown on the surface of the 2″ Si wafer to form an insulating layer. The oxidation

process is given as follows:

- Pre-oxidation wafer cleaning. All beakers and tweezers used for the cleaning should have never contacted any other metals. New beakers, tweezers, and quartzwares should be cleaned before using for the wafer cleaning process. The following cleaning step should be strictly followed in order to avoid contamination of the furnace.
  - Rinse in Acetone with ultrasonic agitation for 3 minutes.
  - Rinse in running de-ionized (DI) water for 1 minute.
  - Rinse in Methanol with ultrasonic agitation for 1 minute.
  - Rinse in running DI water for 2 minutes.
  - Soak in BOE (buffered oxide etchant) for 30 seconds to strip the native oxide on the Si wafer. No glasswares and ultrasonic agitation should be used in this step.
  - Rinse in running DI water for 2 minutes.
  - Transfer wafers into a beaker prefilled with fresh Methanol. The wafers can be move to the furnace loading area in the beaker.
  - Blow dry the wafers with dry N_2 gas, and load the wafers onto the furnace boat.
- Steam oxidation. The wafer boat is then put into a high temperature furnace filled with water steam. The conditions of the oxidation are

7.3.3 Pre-resist wafter cleaning

Each time before the e-beam Resist (or photoresist) is spun onto the wafer, the wafer needs to be cleaned by the following process

Temperature	Time	Thickness
1000°C	80-100 min.	4000-5000Å

Table 7.2: Steam oxidation parameters.

Rinse in Acetone with ultrasonic agitation for 60 seconds.
Rinse in Methanol with ultrasonic agitation for 30 seconds.
Blow dry with dry N_2 gas or spin dry for 30 seconds on the spinner.

Table 7.3: Pre-resist wafer cleaning.

7.3.4 First material layer – Au

Resist Process. The resist used for the Au layer is and MMA/PMMA double layer. The resist is spun on the whole 2″ wafer, which is then diced into $\sim 1 \times 1$ cm^2 pieces. The parameters for the resist process is listed in Table 7.4.

Resist	MMA(8.5) EL7	950 PMMA A8
Spinning speed (rpm)	3000	5000
Spinning time (s)	60	60
Baking temperature (°C)†	170	170
Baking time (min.)	1	30
Cooling time (s)‡	60	60
Resist thickness (nm)	200	500

† This is the temperature reading on the digital display of the hot plate. The actual surface temperature might be lower, $\sim 150 - 160$°C.
‡ The sample is place on a room temperature metallic surface.

Table 7.4: Au layer resist process.

E-beam Lithography. The Au layer has a couple of patterns with features that have very small line-width ($\sim$ 0.1 μm), and are very close to each other, thus the proximity effect needs to be considered.

1. The two sources are $0.5\,\mu m \times 0.1\,\mu m$ microbridges with large Au pads on both

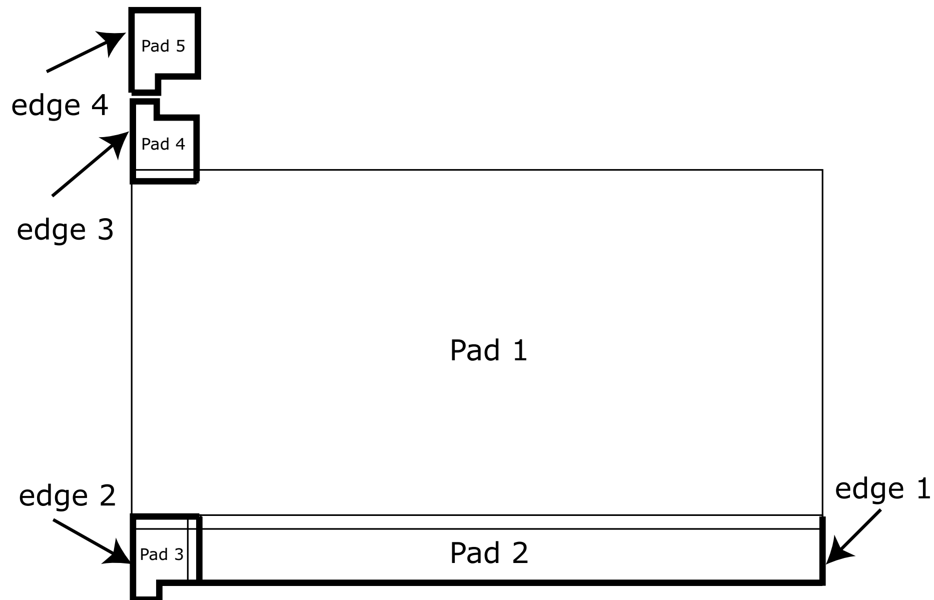

Figure 7.10: Segments of the conductor strip for proximity effect correction.

ends. The pads defining the length of the microbridge ($0.5\,\mu m$) are very close to each other, therefore, if both pads were fully exposed, very large dose would be deposited at the gap region. As a result, the writing in this area tends to be overexposed, and it is very hard to define a very narrow bridge.

2. Similar problem exists in the coplanar stripline that consists of two 30 μm long strips with a 3 μm gap in between. It is very important to maintain a well-defined gap distant along the full length of the stripline[6]. However, the dose from the proximity effect does not have well-define spacial distribution, the edges of the conductors becomes “fuzzy”.

To solve these problems, the big gold pad is divided into a few segments as shown in Fig.7.10. The large rectangle (pad 1) makes up most part of the conductor strip, thus, it is written at a relatively high dose to give full exposure. The smaller rectangle

[6]The characteristic resistance of the coplanar stripline strongly depends on the gap between the two conductors

(pad 2), overlapping with the large rectangle at the top edge, defines the edge of the coplanar stripline gap. It is designed to be slightly underdose, so that there is little proximity effect along the gap edge, and the dose from the large rectangle pad helps to fully expose the majority of the pad except for the edge. In order to define the edge, a single pass line[7], denoted by the thick black line (edge 1) along the lower and right sides of the rectangle on Fig.7.10, is written to add a little extra dose to make a clean " cut " of the resist. Similarly, the small polygon (pad 3) at the lower-left corner defines the length of the microbridge, and a single pass line (edge 2) along the sides of the polygon gives a sharp edge at the side that contacts the bridge.

The blind source is slightly different from the real source that sits between the conductor strips; only the lower polygon pad (pad 4) barely contacts the large conductor strip, while the upper polygon is far away from the strip. Thus the proximity effect does not have strong influence on the lower polygon and has even less effect on the upper one. So the doses for these two polygons should by different between themselves and higher than the polygons at the real source.

The typical exposure parameters for the small critical structures, i.e. the microbridges and the small polygon pads, are given in the following tables.

Au Film deposition. The deposition is done in the PLASSYS e-beam evaporator, with a 99.9999% purity Au source. The Au microbridges are thin films of thickness $10\,nm$, while the rest of the Au structures require thicker film. This is realized in one deposition by using double angle evaporation; a thin (10 nm) layer of Au is first deposited perpendicular to the substrate to form the sources, then a thicker second layer is deposited for the rest thicker Au structures with the substrate tilted at an

[7] A single pass line means during writing, the beam passes along the designed line once, without raster scanning. The width of the line depends on the dose and spot size of the beam.

(a) SEM settings

Magnification	1200
Working distance	10 mm
Spot size	1
Beam current †	23.5 pA
Center-to-Center distance	10 nm
Ling space	10 nm

(b) Area dose (μC/cm^2)

Source	Blind source	pad 3	pad 4	pad 5	edge 2-4
155	160	225	290	300	210

Table 7.5: Exposure parameters for Au critical structures
† The beam current is measured current impinging on the Faraday cup.

angle θ with respect to its original position, and the image of the sources are shift to the side of the resist wall. The film thickness of the second layer is $d \cos \theta$, where d is the reading of the evaporator's crystal monitor, i.e. the thickness of the film if it were deposited perpendicular to the substrate.

It is well know that Au does not stick well to SiO_2 surface. So a thin layer of Ti film is pre-deposited as a " sticking " layer. Since a SiO_x film is to be deposited on top of the Au, a thin Ti "sticking" layer is also needed to cap the Au film[8]. The deposition parameters are in Table 7.6. The initial chamber pressure for the deposition is about 1.5×10^{-7} torr.

	Ti	Thin Au	Thick Au	Ti cap
θ	0°	0°	45°	0°
Rate (nm/s)	0.2	0.5	0.5	0.2
d (nm)	2	20	60	4

Table 7.6: Au e-beam evaporation parameters.

[8]This is introduced to the process by C. Wilson and L. Frunzio

Au Lift Off. After the sample is taken out from the PLASSYS, it is soaked in 65 °C Acetone for 120 minutes[9], and followed by 60 seconds of ultrasonic agitation.

7.3.5 Second material layer – SiO_x

Resist Process. The resist process for this layer is the same as the Au layer, except that the PMMA A8 is soft baked for 5 minutes, since there is no small feature in this layer.

E-beam lithography. The pattern is aligned to the Au layer by using the Au alignment marks co-deposited with the Au patterns. The large and intermediate sets of the alignment marks are used. Exposure parameters for both the alignment and the pattern are given below

	AL mark 1	AL mark 2	SiO_x
Spot size	1	1	4
Magnification	500	1200	1200
Point-to-point space (nm)	30	10	10
Line space (nm)	30	10	10
Area dose ($\mu C/cm^2$)	30	10	10

Table 7.7: E-beam writing parameters for SiO_x.

SiO_x Deposition. The SiO_x is deposited by sublimation. The process is similar to evaporation, except that when the source material is heated, it does not go through liquid phase, but enters the gas phase directly. The SiO_x source is heated by the applied high current in a vacuum chamber (Lasker). The deposition procedure for SiO_x is given in table 7.8 for reference. The starting chamber pressure P_{ch} is $\sim 1 \times 10^{-7}\,torr$. The source is pre-heated to get rid of contaminations before the actual

[9] 65°C is the reading of the hot plate temperature display. The actual liquid temperature is lower, $\sim$ 50°C.

deposition.

(a) Pre-heating SiO_x

Current (A)	Duration (s)	P_{ch} ($\times 10^{-7}$ torr)	Rate (Å/s)
100	120	1	-
200	120	2	-
300	120	2.1	0.2
350	120	2.5	1.0

(b) SiO_x Deposition

Current (A)	P_{ch} ($\times 10^{-7}$ torr)	Rate (Å/s)	Thickness (Å)
440	2.8	15	1000

Table 7.8: SiO_x Sublimation.

SiO_x Lift Off. Since the SiO_x deposition is performed at fairly high temperature (>400°C), the resist is "hard" baked, therefore after the deposition. The sample needs to be soaked in 90 °C (hot plate temperature, not the liquid temperature) PG Remover for 2 hours, followed by 1 minute of ultrasonic agitation, rinsing in Methanol, and blow-drying with dry N_2 gas. The sample is then viewed under optical microscope for remaining SiO_x residue on the chip. If necessary, repeat above process starting from the ultrasonic agitation until there is no visible SiO_x residue on the chip.

7.3.6 Third material layer – $Al/Al_2O_3/Al$ junction

Resist Process The resist for this layer is a thick MMA/PMMA double layer. This is necessary for the required large shift, $\sim 2\,\mu m$, for the double layer deposition of the Al junction. We use the high solid concentration MMA(8.5) EL15 resist as the bottom "sacrificial" layer to achieve large thickness and thus large undercut, $\sim 3\,\mu m$. The parameters of the process are listed in Table 7.9. The resist is baked 30 min to

Resist	MMA(8.5) EL15	950PMMA A8
Spinning speed (rpm)	1500	2500
Spinning time (s)	60	60
Baking temperature (°C)	170	170
Baking time (min.)	1	30
Cooling time (s)	60	60
Resist thickness (nm)	1300	750

Table 7.9: $Al/Al_2O_3/Al$ layer resist process.

assure high writing resolution in PMMA, and also rigid suspended resist bridge for double angle evaporation.

E-beam Lithography The writing of the SQUID junctions is also strongly affected by the proximity effect, but in a rather different way. As shown in Fig.7.11, the wires

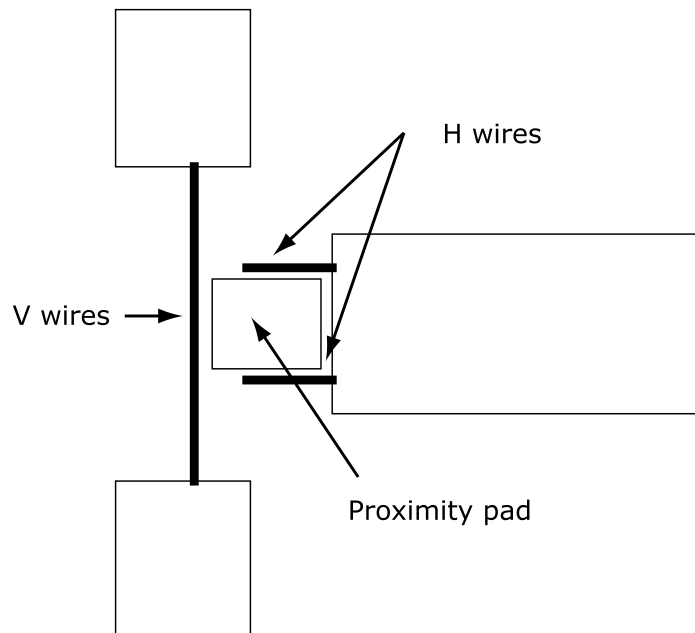

Figure 7.11: Proximity effect in Al junction writing.

that form the junctions of the SQUID are 0.2 μm in width, and are written as single pass lines. Most part of the wires is far away from any large contact pads, except

for at the ends. Therefore, if the dose is defined uniformly along the wires, the ends would have higher effective dose due to the proximity effect from the contact pads, while the parts that are far from the pads have lower dose. As a result, if the latter is fully exposed to have the 0.2 μm width, the ends would be over exposed and be wider. One solution is to assign different doses to different parts of the wire. However, it is unrealistic for such short wires ($\sim 5\ \mu m$). Another alternative is to utilize the proximity effect. A rectangle pad is intensionally added in the space among the wires (the proximity pad in Fig.7.11). The dose of the wires and the pad are both assigned slightly low, and the proximity pad very low to transfer any image to the resist, but it adds extra doses to the resist near by. So now for the parts of the wires that are far from the contact pads, the effective dose is the sum of the designed wire dose and the dose from the proximity pad. The SEM settings of the writing is the same as the Au critical structures in Table 7.5(a), and the typical doses for each parts of the SQUID junction are In addition, the Al layer needs to be aligned to the Au layer by

V wire	H wire	Contact pads	Proximity pad
420	410	410	185

Table 7.10: Area doses in μC/cm^2 for SQUID writing.

using the Au alignment marks. The alignment basically follows the steps of the SiO_x layer.

Al/Al$_2$O$_3$/Al junction deposition The Al/Al$_2$O$_3$/Al junction is deposited in the PLASSYS e-beam evaporator using the double angle technique. The basic steps for making an Al/Al$_2$O$_3$/Al tunnel junction are as follows

Al Lift Off Follow the same procedure as the Au liftoff.

Steps
Purge the chamber with 15 Torr Ar gas
Deposit Al at 0°, 1 nm/s, for 40 nm
Wait 2 minutes for the sample to cool down
Oxidized Al in 3 Torr O_2 gas at room temperature
Deposit Al at 37°, 1 nm/s, for 110 nm
Wait 2 minutes for the sample to cool down

Table 7.11: Double angle evaporation for $Al/Al_2O_3/Al$ junctions.

7.3.7 Fourth material layer – Nb

Resist Process Since Nb is deposited by isotropic sputtering, and the Nb films in the device are all relatively large (the smallest feature is a 2 μm gap), a low temperature soft baked single PMMA layer is used as the resist, as listed in table 7.12.

Resist	PMMA A8
Spinning speed (rpm)	2500
Spinning time (s)	60
Baking temperature (°C)	90†
Baking time (min.)	5
Cooling time (s)	60
Resist thickness (nm)	750

† The baking temperature is chosen at 90 °C to avoid damaging the $Al/Al_2O_3/Al$ junction fabricated in the previous step. In general, the $Al/Al_2O_3/Al$ junction could sustain heat up to 110-120 °C.

Table 7.12: Nb resist process.

E-beam Lithography The patterns are aligned to the Au layer. Since there is no small structures in this layer, the writing follows the similar procedure as the SiO_x layer.

Nb Deposition The Nb film is DC sputtered onto the sample in the Lesker sputterer. The sample is vacuum greased onto the copper sample holder to provide better

thermal contact. Before the deposition, ion beam is used to clean off the remaining resist on the chip, so that the Nb films can have better contacts to the sample. For such purpose, ion beam is applied for 30″.

It is well-known that the sputtered Nb thin films are stressed. The sign of the stress strongly depends on the Ar pressure, at low pressure, the stress is compressive, while at high pressure, the stress is tensile. It also depends on the voltage applied at the cathode – Nb target; the stress is compressive at high voltage and tensile at low voltage[10]. It is very important to have low stress film deposited on top of SiO_x, since the strong stress in the Nb film could peel off the SiO_x from the Au layer[11], shown in optical microscope image in Fig.7.12. After the Nb sputtering, the SiO_x

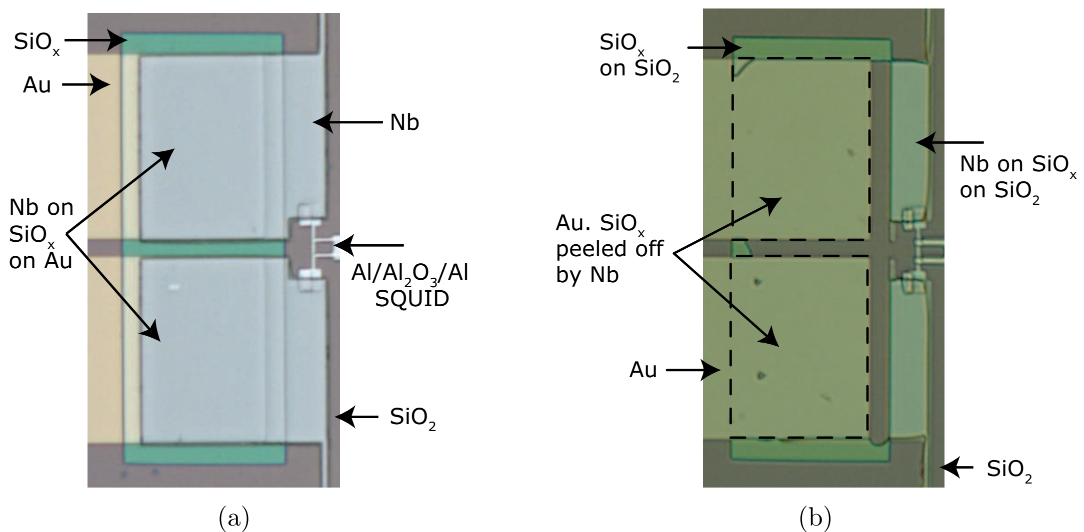

Figure 7.12: Nb film sputtered on SiO_x deposited on Au.
(a) A successful sample. (b) The Nb peels off the SiO_x from the Au layer.

films is mostly peeled off from the Au pad, as indicated in the dashed line rectangle in Fig.7.12(b), except for the little triangular piece at the upper-left corner. Special

[10]For more details, and also the relation of the Nb film T_c and the stress, please refer to (Iosad et al. 2001) and references within.

[11]Au usually does not stick well to SiO_x. Even with the Ti sticking layer, the stress in the Nb is large enough to tear the bond between the Au and the SiO_x.

care is needed to choose the deposition parameters. The parameters used in the process are given in Table 7.13.

Power (W)	Pressure (mTorr)	Rate (nm/s)	Thickness (nm)
330	4	0.9	200

Table 7.13: Nb sputtering parameters.

Nb Lift Off Similar to that of the SiO_x, the resist is hard bake during the high temperature deposition process. Therefore, we use the SiO_x liftoff process for this layer.

7.3.8 Image of the fabricated device

The optical microscope image of the full device (excluding the conducting leads) is shown in Fig.7.13(a). Fig.7.13(b) is an SEM image of the Au micro-bridge photon source, the dimensions of the source are $0.5 \times 0.1 \mu m^2$. Fig.7.13(c) is an SEM image of the SQUID structure for the photon detector, the area of each junction is $0.2 \times 0.2 \mu m^2$.

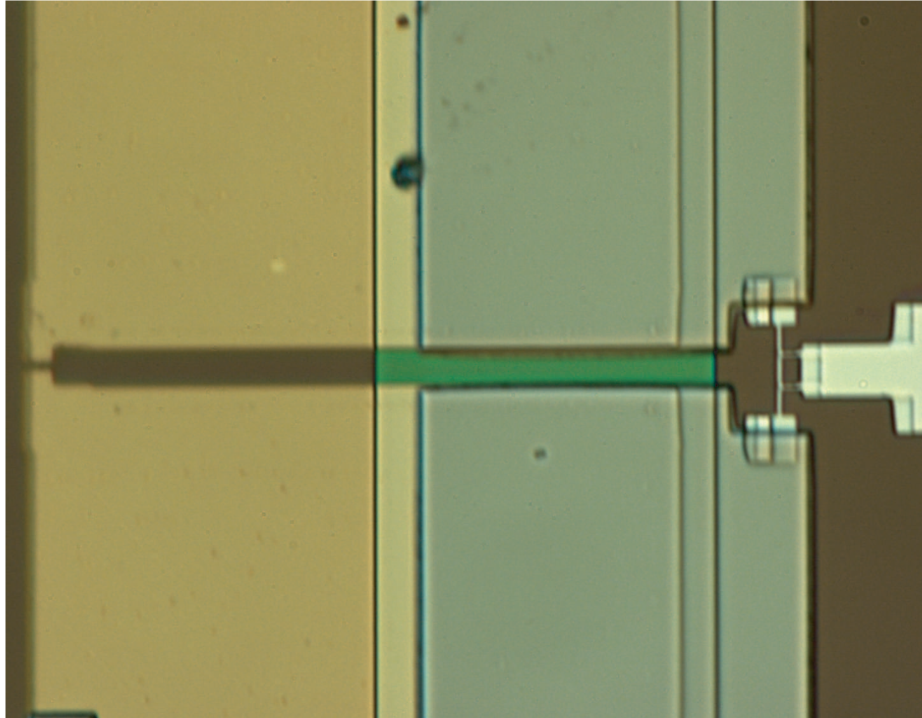

(a) OM image of the on-chip calibration device

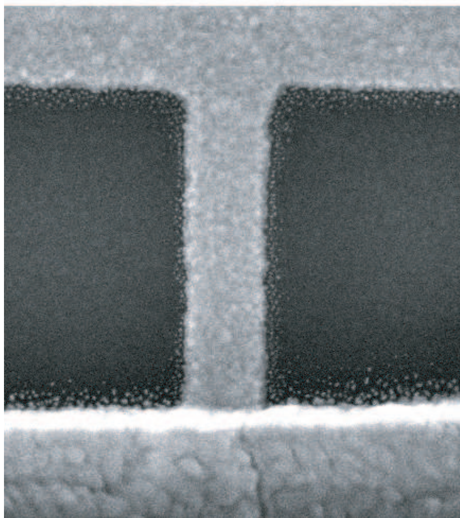

(b) SEM image of the Au source

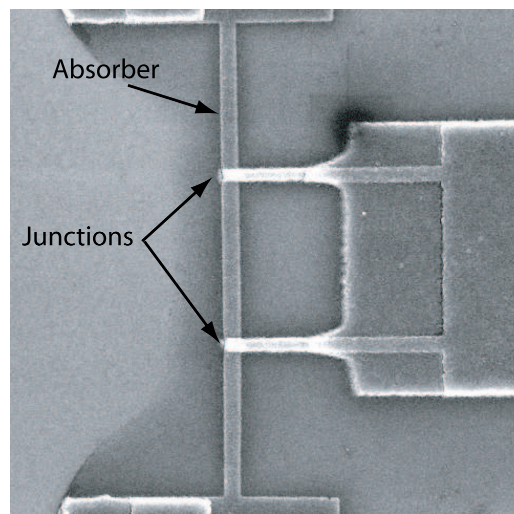

(c) SEM image of the SQUID photon detector

Figure 7.13: Optical microscope and SEM images of the on-chip calibration device.

Chapter 8

Conclusions

8.1 Summary of results presented in this thesis

In summary, we developed a new technique for characterizing the electron-phonon interaction in nano-scale metal thin films at very low temperatures (sub-Kelvin temperatures). The technique involves hot electron generation in the metal films, and the direct electron temperature measuring in the time domain using the fast, sensitive dynamic microwave Johnson noise thermometry. With this technique, we demonstrate the first direct measurement of G_{e-ph}, τ_{e-ph}, and C_e in the same setup, for a single material — Au. Both long diffusive wires and nano-scale wires in SNS structure are measured.

We have measured the electron-phonon heat conductance down to $\sim 10^{-12} W/K$ (device SNS–2 with $\sim 0.1 \mu m^3$ volume) in the steady state. The G_{e-ph}'s for different devices show good volume scaling, and the temperature dependence can be decried by the theory (Sergeev & Mitin 2000) qualitatively. However, the values are about 10–50 times larger than expected.

The electron-phonon interaction time τ_{e-ph} and is directly measured in the time domain. The measured values are in good agreement with the theory (Sergeev & Mitin 2000) in two disordered regimes — the “dirty” metal and the moderate disordered

regime. Howver, by using two different approaches, deriving from the measured G_{e-ph} and τ_{e-ph}, and from the calorimetry measurements, we find that the electronic heat capacities in our devices are very large, deviating from the book values (Ashcroft & Mermin 1976, Kittel 1995) by 10-50 times. This suggests, at sub-Kelvin temperatures, an anomaly in the electronic heat capacity, in micro/nano-scale metal thin films that are deposited on insulating substrate. We propose a few models in attempt to explain the data, but none of them give satisfactory explanations to the results of all three quantities. It is interesting to study such phenomena in the future.

We develop a new on-chip calibration scheme for ultra-sensitive photon detector with the nano-scale metal thin films as the photon source. The electron thermal fluctuation induced Johnson noise transmits photons to the detector through an electrically connected superconducting bandpass filter between the source and the detector. The source can deliver very low power at sub-Kelvin temperatures, and is very accurate and fast due to the extremely weak electron-phonon interaction in the metal film. In this thesis work, we[1] fabricate a simplified version of the no-chip calibration scheme where the filter is replaced by superconducting transmission line. J. Teufel (Teufel 2006) has successful observed photons with the STJ detector in response of the Au thin film source.

The extremely weak electron-phonon interaction in the metal films at low temperatures is also proposed to be used as ultra-sensitive phonon cooled HEBs. The promising sensitivity of the HEB lies in the extremely small electron-phonon heat conductance G_{e-ph}. An optimistic better than 1×10^{-19} W/$\sqrt{Hz}$ NEP is estimated for a Au absorber, at 100 mK, and with book value electronic specific heat. We point out, from our measurements, that the estimation might be over simplified; the actual

[1] Based on the original work of C. Wilson and L. Frunzio

measure electronic heat capacity is 10–50 larger than the book value, which degrades the estimated sensitivity. In order to truly understand the performance of the HEB, one needs to fully characterize the electron-phonon interaction in the absorber material. The technique we developed in this thesis work proves an excellent tool for such tasks.

8.2 Suggestions for future work

Given the unusual results on the electronic heat capacity and the electron-phonon heat conductance, it is important to have further experiments on Au films. An interesting device to look at is a nano-scale Au films in a SNS structure with Al or Ta superconducting leads, which are expected to have better interfaces with Au than the Nb in present structure. Therefore there could be better blockage for the electron out diffusion cooling.

It is also interesting to utilize our new technique to investigate the e-ph interaction in other materials. Especially the materials that are proposed to use in HEBs, since all the previous measurements have not measured the G_{e-ph}, τ_{e-ph}, and C_e independently; G_{e-ph} (τ_{e-ph}) is induced from τ_{e-ph} (G_{e-ph}) with the book value C_e. It is inappropriate to derive the NEP of the HEB from these value, since we have shown that the metal thin films might have different electronic heat capacity from the bulk.

For the ultimate calibration of detector, the superconducting high frequency bandpass filter should be developed.

Bibliography

Altshuler, B. & Aronov, A. (1985), *Electron-Electron Interaction In Disordered Conductors*, 1 edn, Elsevier Science Publishers B.V.

Altshuler, B., Aronov, A. & Khmelnitsky, D. (1982), 'Effects of electron-electron collisions with small energy transfers on quantum localisation', *J. Phys. C* **15**, 7367.

Andreev, A. (1964), 'The thermal conductivity of the intermediate state in superconductors', *Sov. Phys. JETP* **19**, 1228.

Ashcroft, N. & Mermin, N. (1976), *Solid State Physics*, 1 edn, Brooks Cole.

Bennett, W. R. (1960), *Electrical Noise*, McGraw-Hill.

Burke, P. (1997), *Ph.D. Thesis. High Frequency Electron Dynamics in Thin Film Superconductors and Applications to Fast Sensitive THz Detectors*, Yale University.

Callen, H. & Welton, T. (1951), 'Irreversibility and generalized noise', *Phys. Rev.* **83**, 34.

Chatenier, F. J. D. & Miedema, A. R. (1966), 'Observation of the linear term and the h.f.s. contribution to the heat capacity below 1°k of some dilute alloys', *Physica* **32**, 403.

Dalrymple, B., Wolf, S., Ehrlich, A. & Gillespie, D. (1986), 'Inelastic electron lifetime in niobium films', *Phys. Rev. B* **33**, 7514.

Dicke, R., Beringer, R., Kyhl, R. & Vane, A. (1946), 'Atmospheric absorption measurements with a microwave radiometer', *Phys. Rev.* **70**, 340.

Dicke, R. H. (1946), 'The measurement of thermal radiation at microwave frequencies', *Rev. Sci. Inst.* **17**, 275.

Dorozhkin, S. I. & Schoepe, W. (1986), *Solid State Commun.* **60**, 245.

Dumpich, G. & Carl, A. (1991), 'Anomalous temperature dependence of the phase-coherence length for inhomogeneous gold films', *Phys. Rev. B* **43**, 12074.

Echternach, P. M., Gershenson, M. E. & Bozler, H. M. (1993), *Phys. Rev. B* **47**, 13659.

Echternach, P., Thoman, M., Gould, C. & Bozler, H. (2002), 'Evidence of interference between electron-phonon and electron-impurity scattering on the conductivity of thin metal films', *Phys. Rev. B* **46**, 10339.

Friedrichowski, S. & Dumpich, G. (1998), 'One- and two-dimensional quantum transport in thin gold wires', *Phys. Rev. B* **58**, 9689.

Gantmakher, V. (1974), 'The experimental study of electron-phonon scattering in metals', *Rep. Prog. Phys.* **37**.

Gershenson, M., Gong, D., Sato, T., Karasik, B. & Sergeev, A. (2001), 'Millisecond electronphonon relaxation in ultrathin disordered metal films at millikelvin temperatures', *App. Phys. Lett.* **79**, 2049.

Gershenzon, E., Gershenzon, M., Gol'tsman, G., Lyul'kin, A., Semenov, A. & Sergeev, A. (1990), 'Electron-phonon interaction in ultrathin nb films', *JETP* **70**, 505.

Hsu, S., Sheng, P. & Lin, J. (1999), 'Quadratic temperature dependence of the electron-phonon scattering rate in disordered metals', *Phys. Rev. B* **60**, 3940.

Huang, K. (1987), *Statistical Mechanics*, 2 edn, Wiley.

Il'in, K., Ptitsina, N., Sergeev, A., Goltsman, G., Gershenzon, E., Karasik, B., Pechen, E. & Krasnosvobodtsev, S. (1998), 'Interrelation of resistivity and inelastic electron-phonon scattering rate in impure nbc films', *Phys. Rev. B* **57**, 15623.

Iosad, N., Jackson, B., Polyakov, S., Dmitriev, P. & Klapwijk, T. (2001), *Journal of Vacumm Science and Technology A* **19**, 1840.

Jaeger, R. (1993), *Introduction to Microelectronic Fabrication: Volume 5 of Modular Series on Solid State Devices*, 1 edn, Addison-Wesley Publishing Company.

Kapitza, P. (1941), *J. Phys. (Moscow)* **4**, 181.

Karvonen, J., Taskinen, L. & Maasilta, I. (2004), 'Electron-phonon interaction in thin copper and gold films', *cond-mat/0410281 v1* .

Kittel, C. (1995), *Introduction to Solid State Physics*, 7 edn, Wiley.

Komnik, Y. F., Kashirin, V. Y., Belevtsev, B. I. & Beliaev, E. Y. (1994), 'Temperature variation of the time of inelastic electron relaxation in disordered bismuth films', *Phys. Rev. B* **50**, 15298.

Kozhevnikov, A. (2001), *Electron Dynamics and Coherence Effects in Mesoscopic Hybrid Normal Metal - Superconductor Devices*, Yale University.

Li, L., Frunzio, L., Wilson, C. M. & Prober, D. E. (2003), 'Quasiparticle nonequilibrium dynamics in a superconducting ta film', *J. Appl. Phys.* **93**, 1137.

Lin, J. & Bird, J. (2002), 'Recent experimental studies of electron dephasing in metal and semiconductor mesoscopic structures', *J. Phys. C* **14**, R501.

Little, W. (1959), *Can. J. Phys.* **37**, 334.

Madou, M. (2002), *Fundamentals of Microfabrication: The Science of Miniaturization*, 2 edn, CRC Press.

Mather, J., Moseley, S., Leisawitz, D., Dwek, E., Hacking, P., Harwit, M., Mundy, L., Mushotzky, R., Neufeld, D., Spergel, D. & Wright, E. (2002), *astro-ph/9812454v1* .

Nabity, J. (n.d.), *NPGS users manual.*

Nahum, M. & Richards, J. (1991), 'Design analysis of a novel low temperature bolometer', *IEEE Trans. Magn.* **27**, 2448.

Nahum, M. & Richards, J. (1993), 'Design analysis of a novel hot-electron microbolometer', *IEEE Trans. Applied Superconductivity,* **3**, 2124.

Nyquist, H. (1928), 'Thermal agitation of electric charge in conductors', *Phys. Rev.* **32**, 110.

Pathria, R. K. (1996), *Statistical Mechanics*, 2 edn, Butterworth-Heinemann.

Pierre, F., Anthore, A., Pothier, H., Urbina, C. & Esteve, D. (2001), *Phys. Rev. lett.* **86**, 1078.

Pippard, A. (1955), *Philosophical Magzine* **46**, 1104.

Pititsina, N., Chulkova, G., Il'in, K., Sergeev, A., Pochinkov, F., Gershenzon, E. & Gershenzon, M. (1997), *Phys. Rev. B* **56**, 10089.

Pozar, D. M. (1998), *Microwave Engineering*, 2 edn, John Wiley & Sons, INC.

Press, W. H., Teukolsky, S. A., Vetterling, W. T. & Flannery, B. P. (2002), *Numerical Recipes in C++: The Art of Scientific Computing*, 2 edn, Cambridge University Press.

Prober, D., Moseley, S., Schoelkopf, R., Stevenson, T. & Wollack, E. (2004), *NASA proposal* .

Rai-Choudhury, P. (1997), SPIE Press.

Reif, F. (1965), *Fundamentals of Statistical and Thermal Physics*, 1 edn, McGraw-Hill Science/Engineering/Math.

Reizer, M. (1989), *Phys. Rev. B* **40**, 5411.

Rooks, M. (1987), *Electron-Beam Lithography Of Quantum Interference Devices For Electron-Transport Studies*, Yale University.

Roukes, M. (1985), *Ph.D Thesis: Hot Electrons and Energy Transport in Metals at mK Temperatures*, Cornell University.

Roukes, M., Freeman, M., Germain, R., Richardson, R. & Ketchen, M. (1985), *Phys. Rev. Lett.* **55**, 422.

Santhanam, P. & Prober, D. (1984), *Phys. Rev. B* **29**, 3733.

Santhanam, P., Wind, S. & Prober, D. (1987), *Phys. Rev. B* **35**, 3188.

Schmid, A. (1973), *Z Phys. B* **259**, 421.

Schmidt, D. R., Schoelkopf, R. J. & Cleland, A. N. (2004*a*), 'Photon-mediated thermal relaxation of electrons in nanostructures', *Phys. Rev. Lett.* **93**, 045901.

Schmidt, D. R., Yung, C. S. & Cleland, A. N. (2004), *Phys. Rev. B* **69**, 140301(R).

Schmidt, D., Schoelkopf, R. & Cleland, A. (2004*b*), 'Photon-mediated thermal relaxation of electrons in nanostructures', *Phys. Rev. Lett.* **93**, 045901.

Sergeev, A., Karasik, B., Gershenson, M. & Mitin, V. (2002), 'Electronphonon scattering in disordered metallic films', *Physica B* **316**, 328.

Sergeev, A., Karasik, B., Ptitsina, N., Chulkova, G., Il'in, K. & Gershenson, E. (1999), 'Electronphonon interaction in disordered conductors', *Physica B* **263**, 190.

Sergeev, A. & Mitin, V. (2000), *Phys. Rev. B* **61**, 6041.

Shannon, C. E. (1948), 'A mathematical theory of communication', *Bell System Technical Journal* **27**, 379–423 and 623–656.

Siddiqi, I. (2002), *Ph.D Thesis: Critical Temperature Dependence of High Frequency Electron Dynamics in Superconducting Hot-Electron Bolomter Mixers*, Cornell University.

Simons, R. N. (2001), *Coplanar Waveguide Circuits Components & Systems*, 1 edn, Wiley-IEEE Press.

Stoner, R. & Maris, H. (1993), *Phys. Rev. B* **48**, 16373.

Swartz, E. & Pohl, R. (1989), *Rev. Mod. Phys.* **61**, 605.

Taskinen, L., Kivioja, J., Karvonen, J. & Maasilta, I. (2004), *cond-mat/0410283* .

Teufel, J. (2006), *Ph.D. Thesis*, Yale University.

Wellstood, F., Urbina, C. & Clarke, J. (1994), *Phys. Rev. B* **49**, 5942.

White, D., Galleano, R., Actis, A., Brixy, H., Groot, M. D., Dubbeldam, J., Reesink, A., Edler, F., Sakurai, H., Shepard, R. & Gallop, J. C. (1996), 'The status of johnson noise thermometry', *Metrologia* **33**, 325.

Wind, S., Rooks, M., Chandrasekhar, V. & Prober, D. (1986), *Phys. Rev. Lett.* **57**, 633.

Wu, C. Y. & Jian, W. B. (1998), *Phys. Rev. B* **57**, 11232.